Characterizing the Structure and Mechanics of 2D Clathrin Lattices with Atomic Force Microscopy

Dissertation

for the award of the degree

"Doctor rerum naturalium"

of the Georg-August-Universität Göttingen

within the doctoral program

Physics of Biological and Complex Systems

of the Georg-August University School of Science (GAUSS)

submitted by

Mitja Platen

from Bielefeld

Göttingen, August 27th, 2015

Members of the Thesis Committee:

Dr. Iwan A.T. Schaap (Supervisor, 1st Reviewer)

III. Institute of Physics

Faculty of Physics

Prof. Dr. Kai Tittmann (2nd Reviewer)

Albrecht von Haller Institute

Faculty of Biology and Physiology

Prof. Dr. Claudia Steinem

Institute of Organic and Biomolecular Chemistry

Faculty of Chemistry

Additional Members of the Examination Committee:

Prof. Dr. Michael Meinecke

European Neuroscience Institute

Dr. Florian Rehfeldt

III. Institute of Physics

Faculty of Physics

Dr. Thomas Burg

Max Planck Institute for Biophysical Chemistry

Date of the oral examination: October 22nd, 2015

I herby declare that this doctoral thesis entitled "Characterizing the Structure and Mechanics of 2D Clathrin Lattices with Atomic Force Microscopy" has been written independently with no other sources and aids than those quoted.

Mitja Platen
August 27$^{\text{th}}$, 2015
Göttingen, Germany

ACKNOWLEDGMENTS

ABSTRACT

Clathrin is a self-assembling protein involved in intracellular trafficking. Since its discovery in the early 1960s, much has been learned about its structure, assembly, and regulation mechanisms. The three legged monomers, called triskelia, are known to form cages in order to invaginate the cell's plasma membrane and, thus, create coated vesicles which contain incorporated extracellular molecules. So far, clathrin research has mostly been focused on these clathrin cages and clathrin-coated vesicles. However, already in the 1980s researchers observed another form of clathrin assembly, namely flat hexagonal lattices attached to the plasma membrane. Little is known about these structures, and whether these flat lattices are involved in clathrin cage formation has been highly debated.

The atomic force microscope (AFM) allows the study of biological samples in liquid and, therefore, near their native state. In this work, we took advantage of this unique capability of the AFM to study the 3D structure of flat clathrin lattices at nanometer resolution. The susceptibility of the lattice to mechanical forces, a common issue when investigating soft biomaterials with AFM, was tested using different scan techniques exerting scanning forces from tens of pN to several nN.

After discussing the assembly of the flat clathrin lattice itself, the first part of this thesis shows how the AFM can be used to study biological questions in the clathrin field. First, a highly featured image of a hexagonal lattice pore was reconstructed from multiple low force AFM scans. The obtained image was used to investigate the triskelion orientation inside the lattice, and to determine a change in the pucker angle when compared to triskelia in a cage. Secondly, force maps were acquired to investigate the mechanical influence of the clathrin light chains (CLC) on the stability of the lattice. The findings suggest that the CLC has a role in rigidifying the structure of the triskelia.

Beyond the investigation of biological properties and mechanisms of clathrin, this thesis additionally explores the application of the flat lattices in bionanotechnological designs. Besides the very regular spacing of the 30 nm-sized pores, clathrin assemblies provide the possibility of specific functionalization, which turns them into useful matrices for sensors and biosynthetic reactors. Towards this goal, we

were able to show that the lattice can be assembled on various surface materials and can be stabilized into durable matrices. AFM experiments showed that the stabilized lattice structure remains intact even after a dehydration and rehydration cycle. Finally, a first demonstration to functionalize the lattice with inorganic particles and biologically active molecules is presented.

CONTENTS

iv

ABBREVIATIONS

AFM	Atomic force microscope
AP	(3-Aminopropyl)-triethoxysilane
ATP	Adenosine Triphosphate
BSA	Bovine serum albumine
CHC	Clathrin Heavy Chain
CLC	Clathrin Light Chain
DNA	Deoxyribonucleic Acid
EDTA	Ethylenediaminetetraacetic Acid
EGTA	Ethylene Glycol Tetraacetic Acid
EM	Electon Microscopy
ENTH	Epsin Amino-Terminal Homology
EPS15	Epidermal Growth Factor Substrate 15
FFT	Fast Fourier Transform
FZ	Force Distance
GST	Glutathione S-Transferase
HEPES	4-(2-Hydroxyethyl)-1-Piperazineethanesulfonic Acid
HOPG	Highly Ordered Pyrolytic Graphite
Hsc70	Heat Shock Cognate 70
k_{eff}	Effective Spring Constant
m_{eff}	Effective Mass
MES	2-(N-Morpholino) - Ethanesulfonic Acid
MW	Molecular Weight
NaSCN	Sodium Thiocyanate

PBS	Phosphate-Buffered Saline
PSD	Power Spectral Density
Ψ	Pucker Angle
PtdIns(4,5)P2	Phosphatidylinositol 4,5-bisphosphate
PVF	Polyvinyl Formal
SEM	Standard Error of the Mean
siRNA	Small interfering RNA
SMR	Suspended Microchannel Resonator
STM	Scanning Tunneling Microscope
UA	Uranyl Acetate

Part I

INTRODUCTION

MOTIVATION

Since many years the atomic force microscope (AFM) has been used to study biological samples, ranging from DNA [1] and proteins, such as collagen [2] and microtubules [3], to whole cells [4]. Hereby, the AFM offers certain advantages over other imaging techniques, such as light- and electron microscopy. One of the main advantages of the AFM for the investigation of biological samples is certainly the possibility to image unlabeled samples in a liquid environment [5], allowing observations at almost native conditions. Furthermore, the AFM allows to acquire 3D images with resolution far beyond the Abbe diffraction limit. However, the atomic resolution that can be achieved for hard and flat materials [6, 7], is unfortunately not accessible for biological samples. Here, the resolution is mainly limited by the size of the AFM-probe (tip) on one hand, and by the properties of the sample itself on the other [8, 9]. A stiffer biological sample, such as collagen or DNA, can be imaged with high resolution (nm regime). In contrast, it is more difficult to acquire detailed images of soft samples, such as whole cells. The main obstacle for the examination of soft samples via AFM are the scanning forces exerted and, therefore, the deformations of soft samples [9] represent one of the major drawbacks for this imaging technique.

The aim of this project was to examine the possibilities of using the AFM to study soft protein complexes, which led to the investigation of several protein assemblies (see also appendix 1). This thesis will be focused on discussing the studies of the hexagonal protein lattice assembled by clathrin. As discussed later on, different attempts were used to obtain high resolution images of the clathrin network as well as to study its mechanical behavior.

All work concerning the AFM experiments as well as the quantitative data analysis of electron micrographs was performed by me. The sample purification, protein functionalization and electron microscopy was performed by our collaborators from the group of Prof. Dr. Ernst Ungewickell (Hannover Medical School). Major parts of the results presented in this work were published in Traffic [10] and Nature Nanotechnology [11].

ATOMIC FORCE MICROSCOPY

2.1 GENERAL DESCRIPTION OF THE ATOMIC FORCE MICROSCOPE

As a successor of the scanning tunneling microscope (STM), Binnig and Quate introduced the atomic force microscope in 1986. Unlike the STM, which was limiting surface investigations to conductive samples, the AFM was now able to expand the variety of samples by also allowing the analysis of insulators [12]. Nowadays, the AFM is used to study diverse surfaces with near atomic resolution [13] and finds application in major scientific fields such as electronics, material science (including soft polymers), and biology [14].

The AFM setup is straightforward and consists of a cantilever with a sharp tip, con-
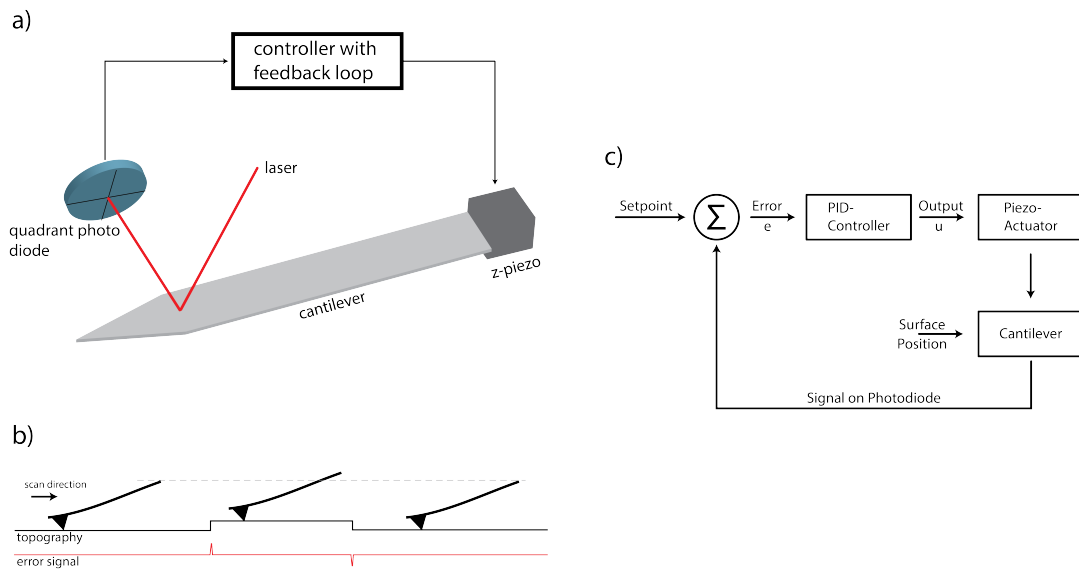
Figure 1: a) Illustration of the AFM setup. b) Schematic of how the AFM responds to an error signal, occurring due to sample features. c) Control loop of a scanning AFM.

trolled by a piezoelectric actuator. The deflection of the cantilever is measured via a laser beam focused onto the cantilever's end, which is reflected onto a position

sensitive photodiode [14] (Fig. 1 a). The critical component of this system is the cantilever, which needs to be soft enough to bend while scanning soft materials but in the same time it needs a high resonance frequency, to allow for high scan rates [12].

$$f_0 = \frac{1}{2}\pi \left(\frac{k}{m_0}\right)^{1/2}$$

(1)

With f_0 being the resonance frequency, k the spring constant and m_0 the effective mass of the cantilever, equation 1 shows that a sufficient frequency can be obtained by keeping the ratio k/m_0 large [12]. Another way to describe the resonance frequency of rectangular cantilever is to consider the dimension of the cantilever as in equation 2 [15, 16].

$$f_0 = \frac{1.02t}{2\pi l^2} \left(\frac{E}{\rho_{cantilever}}\right)^{1/2}$$

(2)

Here, t represents the thickness of the cantilever, l its length, E the cantilever's Young's modulus and $\rho_{cantilever}$ its density. While analogous to equation 1, the ratio between cantilever stiffness and density is crucial, it additionally shows that cantilevers with high resonance frequency can be produced by increasing their thickness or by shortening them.

2.2 IMAGING WITH THE AFM

In order to acquire images with an AFM, the cantilever tip is moved across the surface. During the scanning process, the error signal, which is the difference between the recorded signal (e.g. deflection or amplitude; see Tab. 1) and the corresponding set-point, is monitored. This error is then used in a feedback loop that restores the distance between tip and sample (Fig. 1 b,c), and allows the AFM tip to follow the surface topography. The resulting Z-piezo movement, which is necessary to keep a constant distance between tip and surface, is used to create the topographical height image of the sample [14].

Due to the scanning, exerting a certain imaging force on the sample is inevitable and, therefore, the need for gentle scanning techniques is high. This applies especially to fragile samples, such as biological ones. One major factor, on which the scanning force depends, is the stiffness of the cantilever. Still, even a very soft cantilever,

Table 1: Error signals and force regimes of different imaging modes

	Error Signal	Force Regime
Contact Mode	deflection	repulsive
Amplitude Modulation	amplitude	repulsive/attractive
Jumping Mode	deflection	repulsive/attractive

barely in contact with the sample, exerts a force onto it. This is demonstrated in figure 2, displaying the forces resulting from thermal fluctuations of the cantilever, for different cantilevers with varying resonance frequencies and spring constants. In order to establish stable scanning conditions, the set-point during imaging has to exceed this thermal noise level and, therefore, figure 2 depicts the uttermost minimum scanning forces for those specific cantilevers. Besides the choice of the cantilever, the amount and type of force, which is exerted onto the sample during scanning, can be majorly controlled choosing different imaging or operating modes. As mentioned before, these imaging modes work via different error signals, and, furthermore, in different force regimes (attractive/ repulsive) (Tab. 1) [13, 14].

The first two imaging modes implemented for AFM were the contact- and non-
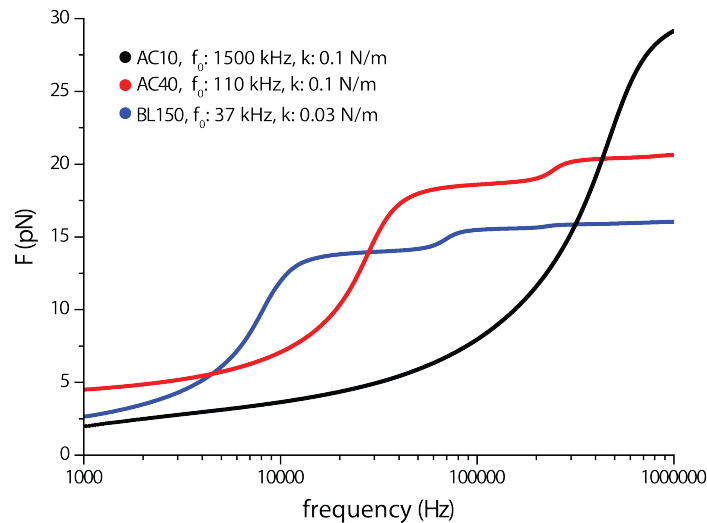
Figure 2: a) Forces which already occur due to thermal fluctuations of different cantilevers. AC10, AC40 and BL150 are different cantilever types available by Olympus.

contact mode [17]. Albeit certain efforts to make the non-contact mode a feasible option for experiments in liquid [18], its difficult feedback conditions [17, 19] render

this imaging mode to be inconvenient for biological studies. Hence, this mode is not further discussed in this work.

2.2.1 *Contact Mode*

The second historically implemented imaging mode is the contact mode [17]. This mode works mainly in the repulsive regime (Fig. 2 b) and the cantilever tip stays in permanent contact with the sample [14, 19]. The monitored error signal is based on the deflection of the cantilever itself and it can be used in two different ways (constant height or constant force). In the constant height version, the cantilever remains at the same height during the whole scanning process and only the deflection is recorded. More commonly the constant force version is used, in which the bending of the cantilever and, therefore, the imaging force is kept constant by using a feedback loop. This feedback ensures a constant distance between the tip and the sample surface by restoring the cantilever deflection to match the set-point via the extension or retraction of the Z-piezo [14]. The major drawback of the contact mode is the destruction and deformation of soft samples, which occur due to the constant contact during the scan motion, generating high lateral forces (Fig. 3) [5, 13]. Therefore, the contact mode is generally not well suited for the investigation of biological and polymer samples [20], with the exception of complete cell imaging with soft cantilevers [21, 22] and the imaging of protein crystals [23].
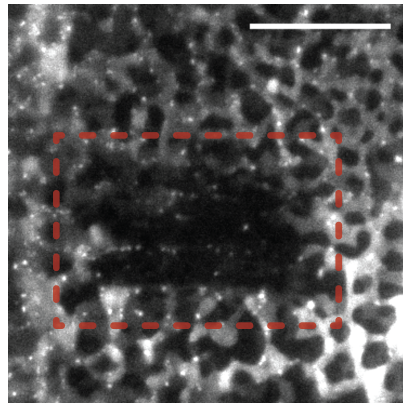
Figure 3: Inside the boxed area a destroyed lipid bilayer is visible, caused by the lateral forces during contact mode scanning, scale bar 2 μm.

2.2.2 *Amplitude Modulation*

The intermittent contact mode, also called the tapping mode or amplitude modulation, overcomes the problems occurring in contact mode, and is the most commonly used imaging mode to obtain scans of fragile samples [13, 20]. Here, the cantilever is excited near its resonance frequency and its oscillation amplitude (typically 20-100 nm) is monitored [5, 19]. While oscillating, the cantilever tip impacts the surface only for a very limited duration, which largely eliminates lateral forces during the scanning process [13, 20]. The monitored error signal in this mode is based on the oscillation amplitude, which is reduced when the cantilever is brought close to the surface (Fig. 4 a). The observed amplitude reduction is due to energy losses, caused by the interaction with the surface [5, 13]. Using a feedback loop, a constant amplitude can be maintained by ensuring a constant distance between the cantilever tip and the surface [19].

Despite, the elimination of the lateral force, there is a minimum normal force which
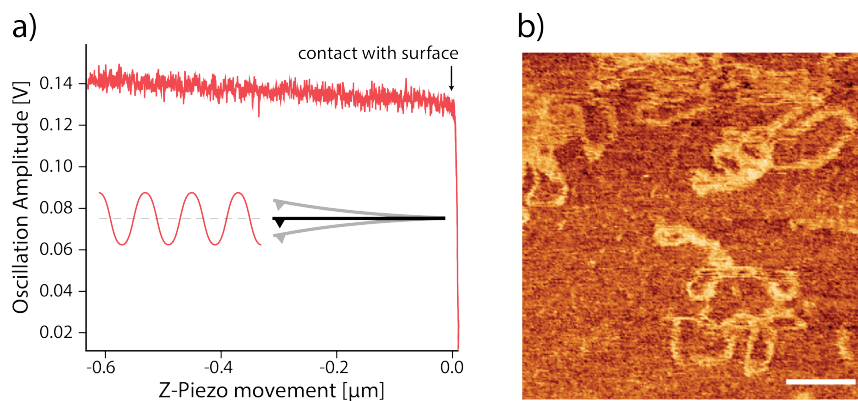
Figure 4: a) Reduction of the oscillation amplitude when an AFM cantilever approaches the surface. b) DNA scanned in tapping mode; scale bar 100nm

needs to be applied to the sample. Besides overcoming the above discussed thermal noise force, the restoring cantilever force after impact needs to exceed the adhesion force between sample and tip, in order to ensure proper sampling [5, 13]. Hence, a minimum free amplitude is necessary to obtain an adequate image of the surface topography. Controlling the amount of force, which is applied to the sample during amplitude modulation, is challenging due to a large number of variables (e.g. sample elasticity, viscosity, adhesion and surface charge) [20], and represents one

of the major drawbacks of this mode. Furthermore, the actual force applied to the sample is difficult to estimate. In 1994, C. Putman described one strategy to estimate an average scanning force (F_{av}). The average force can be obtained by describing the cantilever movement via a harmonic oscillator and reducing it to equation 3, by considering the system at the time of impact [5].

$$F_{av} = k\,A_0\,\frac{4\,\pi^2}{3}\left(\frac{\tau}{T}\right)^2 \tag{3}$$

In this formula k is the spring constant, A_0 the amplitude, T the oscillation period and τ represents the period where the tip is in contact with the sample [5]. Still, the applied force during imaging with tapping mode remains only an estimation. Nonetheless, amplitude modulation is commonly used to image soft materials and allows the imaging of a wide variety of biological samples, e.g. DNA (Fig. 4 b).

2.2.3 Jumping Mode

Jumping mode represents a compromise between contact mode and the dynamic modes (frequency- and amplitude modulation). The idea is to use fast force-distance (FZ) curves (Fig. 5 a and section 2.4) throughout the scan area [24]. This allows great
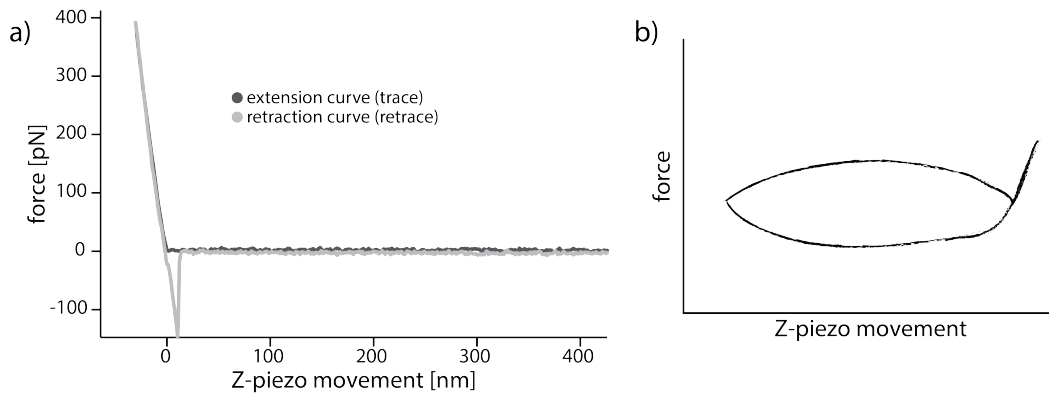
Figure 5: a) Example force distance curve, trace: the cantilever moves toward the sample, retrace: the cantilever is retracted from the surface. b) Sinusoidal force curve acceleration for jumping mode.

control over the imaging force because, similar to the contact-mode, the error signal is based on the cantilever bending and, therefore, the exact imaging force can be determined. In fact, even the normal force drift, which can appear in contact mode

due to slow changes in the deflection signal, is overcome, since the zero force voltage for the unbend cantilever can be reset for each point of the scan [24]. In order to establish fast scanning and to reduce piezoelectric resonances, a sinusoidal wave is used to drive the piezo elements during the FZ curves (Fig. 5 b) [24]. Analogous to amplitude modulation, the jumping mode eliminates lateral forces because the cantilever is moved in X and Y direction when it is at its furthest Z distance and, therefore, out of contact with the sample [24].

2.3 AFM MEASUREMENTS IN LIQUID

One major benefit of using atomic force microscopy for biological studies is the possibility to scan unlabeled samples in liquid and, therefore, close to physiological conditions [25, 26]. Moreover, the operation in liquid eliminates capillary forces and reduces van der Waals forces [25, 27]. However, compared to the cantilever behavior in air or vacuum, the oscillatory characteristics change dramatically in liquid [28]. When driven by a piezo actuator, one can observe not only a single peak at the cantilever's resonance frequency, but a forest of peaks (Fig. 6) [28]. The additional peaks are thought to appear due to the so called fluid drive spectrum, which represents the hydrodynamic modes of the liquid when the cantilever is oscillated [28, 29]. Major changes in the cantilever's oscillatory behavior can be observed while looking
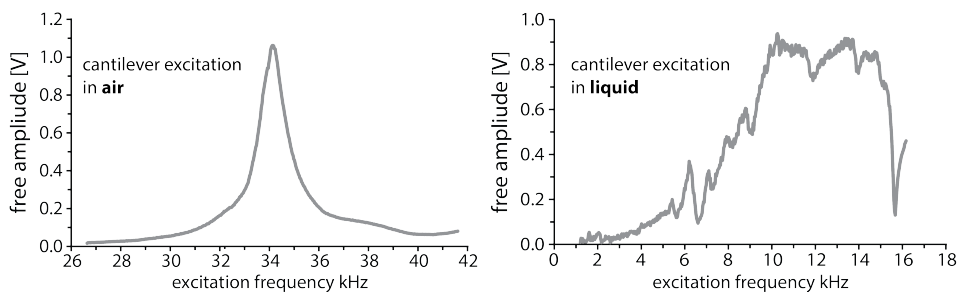
Figure 6: A cantilever excitation spectrum of the same cantilever in air and in liquid shows a change from a single resonance frequency peak to a forest of peaks. In addition, the resonance frequency shifts by roughly one-third in the liquid environment.

at its resonance frequency and quality factor (Q). In contrast to operation in air or vacuum, the resonance frequency is highly influenced by the size of the cantilever [30]. Due to liquid drag during cantilever oscillation, the effective mass is increased

by a factor of 10-40, which in turn reduces the resonance frequency [26, 28, 30] (compare to Equation 1 and Fig. 6). An estimation of the resonance frequency reduction in liquid can be described as follows [30]:

$$\frac{f_{water}}{f_{air}} \cong \sqrt{\frac{m_{lever}}{m_{lever} + m_{water}}} \tag{4}$$

Furthermore, the strong hydrodynamic interactions between the cantilever and the liquid are reducing the Q factor by around two orders of magnitude [26]. The dependency of the Q factor can be described by equation 5 [30]:

$$Q = \frac{m\,\omega}{\gamma} = \frac{(m_{lever} + m_{added})\,\omega}{\gamma}\;, \tag{5}$$

where ω describes the cantilever pulsation and γ represents the damping coefficient, which scales with liquid density [30]. The low Q factor reveals also one major drawback of the imaging in liquid using dynamic modes (i.e. non-contact and tapping mode), since it indicates high forces between the tip and the sample due to reduced sensitivity [26].

2.4 PROBING ELASTICITY WITH THE AFM

Additionally to the utilization of AFM for imaging surfaces with high resolution, another wide spread use is probing of sample mechanics via the recording of force-distance (FZ) curves. An example FZ curve is shown in figure 5 a), representing the cantilever movement towards the sample and its deflection during sample indentation [31]. Hereby, the abscissa shows the movement of the Z-piezo and the ordinate displays the signal detected by the photodiode, which is proportional to the applied force [32, 33]. Additionally to the indentation (extension) curve, the retraction from the sample is also recorded (retraction curve). The retraction curve holds important information, such as information about the adhesion force, and it can be used to investigate whether a sample is elastically or plastically deformed, when comparing it with the extension curve. The different shapes of those curves and the information one can receive from them was described in details by Burnham, Colton and Pollock in 1993 [34].
The slope of the extension curve is often used for material characterization, more

precisely, it is used to obtain the sample elasticity [35], which is represented via the Young's modulus (E), defined by equation 6 [36].

$$E = \frac{F/A}{\Delta l/l_0} \tag{6}$$

Hereby, F/A represents the stress (force over area) and $\Delta l/l_0$ is the change in length with respect to the original length, called strain [36]. A main challenge in these investigations is the non-linearity of the recorded FZ curves from soft samples. This is due to the fact that the AFM tip is conical for a few 100nm and, therefore, the contact area increases while indenting the sample [31] (Fig. 7). This problem was discussed by Hertz already in 1882 [37], and his model is now the most commonly used one to deduce the Young's modulus from the recorded FZ curves by fitting of equation 7 for conical indentations [31].

$$F = \delta^2 \frac{\pi}{2} \frac{E}{(1-\nu^2)} \, tan(\alpha) \tag{7}$$

In this equation δ represents the indentation depth, ν the Poisson ratio and α the opening angle of the tip [31].
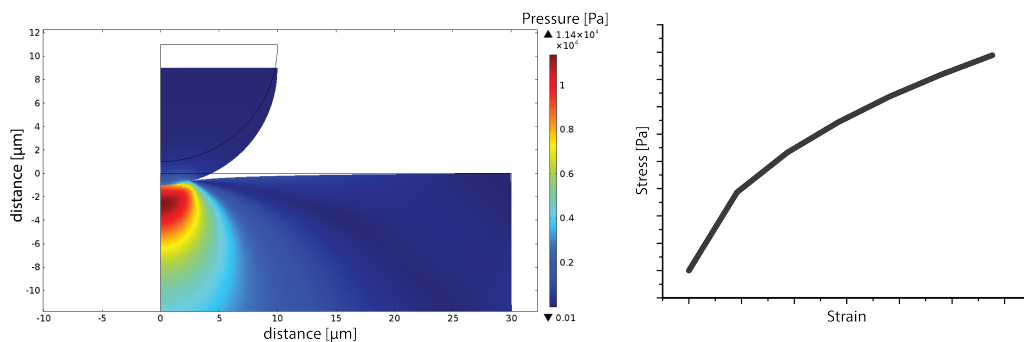
Figure 7: Simulation of a soft sample indentation with a spherical object. Note that the stress vs strain relation is not linear due to the increasing load applying surface area with extending indentation.

CLATHRIN

The compartmentalization of eukaryotic cells generates a need for transport vesicles, which allows controlled endo- and exocytosis to internalize and secrete specific molecules, respectively (Fig. 8) [38]. In the case of endocytosis the cell membrane
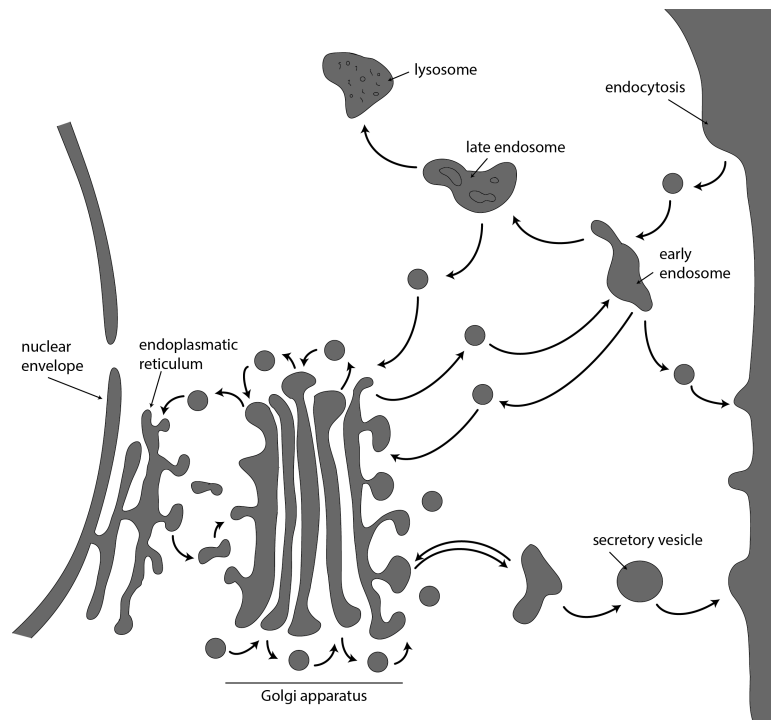
Figure 8: Schematic of intracellular trafficking. Here, the formation of lipid vesicles plays an important role; based on [38].

needs to be invaginated to form transport vesicles. Apart from certain exceptions [39, 40], this is established by coated pits and vesicles [41]. These coated pits occupy around 2 % of the plasma membrane area [42], and the main coat forming protein is clathrin [41, 43]. Barbara M. F. Pearse was the first one to successfully isolate the coated vesicles and also suggested the name "Clathrin" (lat. *clathratus*, lattice like) [44, 45]. However, the discovery of the coated vesicles goes back to the early 1960s. By looking at small vesicles or pits at the cell surface in 1962, Roth and

Porter discovered ordered "spines" around these structures. Interestingly, already then they speculated that these "spines" might play a role in membrane infolding and in pinching off the vesicles [46]. Shortly after this discovery Roth and Porter reported that these coated vesicles indeed are involved in protein uptake [47, 48], which was confirmed by Bowers in 1964 [49], who furthermore suggested that this uptake might be selective. Additionally, he observed that the coat was polygonal and suggested a honeycomb-like or alveolate structure. Such basket-like structure was confirmed by Kanaseki and Kadota in 1969 [50], who revealed a network of pentagons and hexagons (Fig. 9). This icosahedral network was further analyzed by Pearse in 1976, discussing different types of cages which were based on structures consisting of hexagons and 12 pentagons [45, 51].
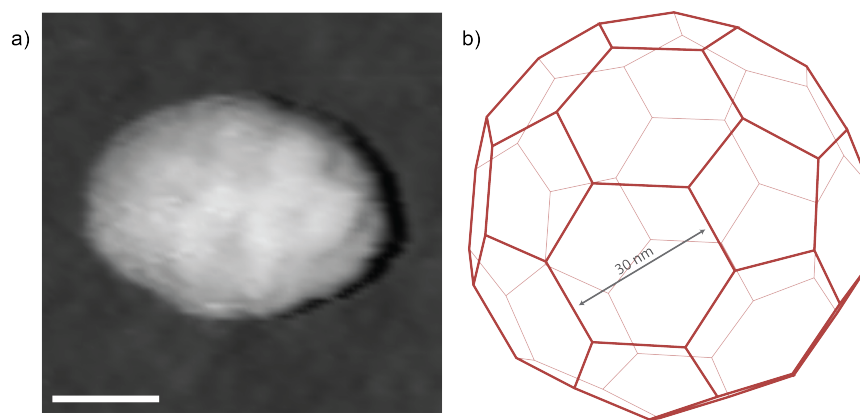
Figure 9: a) AFM image of the clathrin cage in liquid, scale bar 50 nm. b) Sketch of the icosahedral clathrin cage.

3.1 STRUCTURE

The clathrin network is composed of a three legged structure, called triskelion, identified and named by E. Ungewickell in 1981 [52] (Fig. 10, inset). This structure is a trimerization of three clathrin heavy chains (CHC), radiating from a hub [52, 53, 54]. Continuing from the hub, which is formed by the C-termini of the CHC [55], each triskelion leg consists of several segments: the proximal segment, knee, distal segment, ankle and terminal domain (Fig. 10) [54]. Each CHC forms a relatively uniform leg [55] with a molecular weight (MW) of 190 kDa [55], a preferred direction of curvature [52], and a length of around 44 nm [52, 56] to around 47 nm [57].

Associated to the CHC are three clathrin light chains (CLC) [52]. These CLC rep-
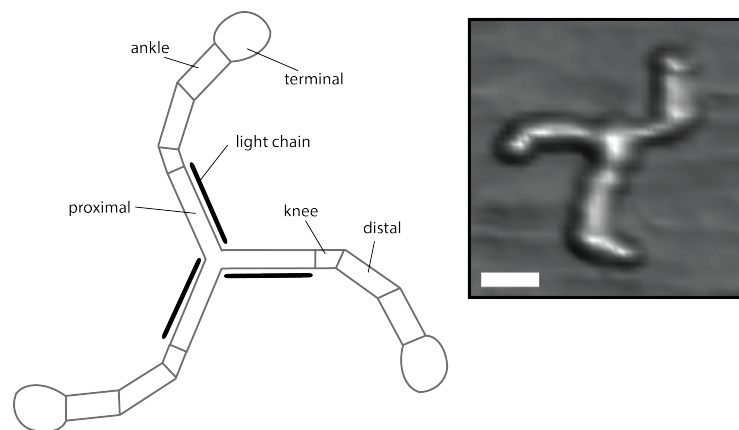
Figure 10: Schematic of a triskelion with its different segments of the CHC and the attached CLC. Inset: AFM image of a triskelion in liquid, scale bar 20 nm.

resent α-helices with a MW of 25 kDa [54], which become ordered after specifically binding to the proximal leg (Fig. 10) [58]. Exceptions are the N- and C-termini of the CLC, which remain unstructured [55]. There are two different types of CLC (a and b), their distinct role, however, is so far unknown [53].

At concentrations above 0.05 mg/ml, these triskelia start to self-assemble into the above mentioned polyhedral basket structures, which are involved in cell membrane invagination [53, 56]. Each vertex in this structure consists of a triskelion hub [54]. Radiating from these vertices are the proximal segments, which extend towards the neighboring triskelia. Following the proximal segments are the knees, from which the legs gradually protrude inwards the forming cage by extending the distal segments towards the neighboring triskelia (see Fig. 11). At the end of each leg, the terminal domain which is found at the cage interior, forms a hook-like structure that connects the cage with the appropriate adaptor proteins (described in section 3.2) [54, 55]. Since the proximal segments are well aligned in the clathrin network and the legs begin to disperse after the knee [54], the knee is considered the most variable part of the triskelion [55].

The cages have a diameter between 50 nm and approximately 100 nm [50] and consist of hexagons and pentagons. In addition to clathrin cages, flat clathrin lattices can also be found at the inner membrane of the cell, which predominantly consist of hexagons (Fig. 13 a) [59]. In order to form a cage, the clathrin network must contain 12 pentagons, to create the curvature, and a variable number of hexagons,
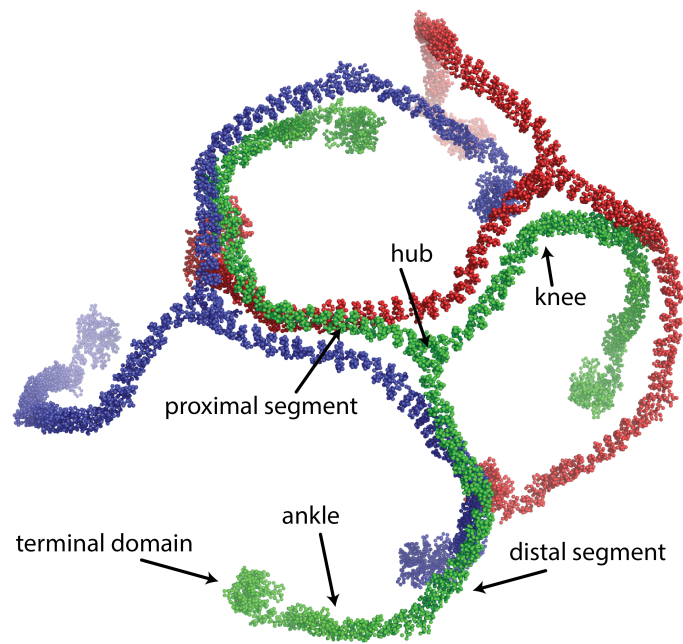
Figure 11: Structure of three triskelia forming a partial pore inside a clathrin cage. The structure reveals clearly the adjacent proximal segments of neighboring triskelia and the inward protrusion of triskelia legs from the knees on (green triskelion labeled). Adaptation from PDB structure 3IYV, CLC were removed for clarification.

which scale the vesicle size [56]. The average diameter of a polygonal pore inside the network is 30 nm [59], with a distance between two vertices of around 18 nm [56]. Inside the cell a clathrin network can span more than 300 nm [59].

3.2   CLATHRIN COAT FORMATION AND DISASSEMBLY

The cycle of endocytosis via clathrin coated vesicles is depicted in figure 12 and can be divided into three different phases: initiation, propagation, and detachment and uncoating phase.

Already the initiation phase raises unsolved questions in clathrin-mediated vesicle
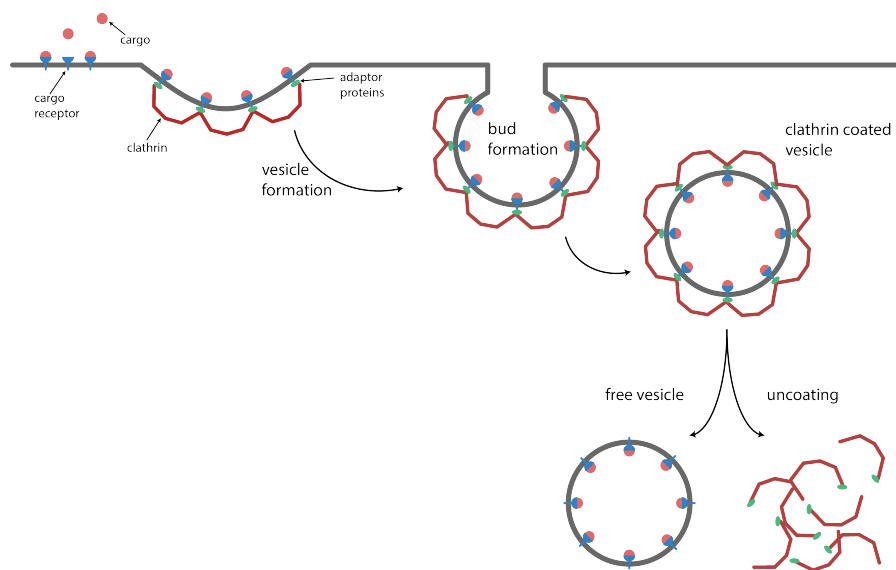
Figure 12: Schematic of lipid vesicle formation in endocytosis by the clathrin pathway.

formation. Besides clathrin coated pits, in 1980 Heuser discovered also flat hexagonal clathrin lattices at the plasma membrane [59]. This spurred a debate on whether the budding vesicles are formed via the rearrangement of flat lattices, or via free triskelia from the cytosol (Fig. 13). A good argument against the hypothesis of vesicle formation via the lattice, is in fact that the rearrangement needed to introduce pentagons into the hexagonal lattice, in order to introduce curvature, is energetically unfavorable [60]. In addition, membrane patches without any signs of hexagonal lattices are also able to form clathrin coated pits [59]. On the other hand, simulations by Nossal suggested that the remodeling of the lattice might occur due to thermal
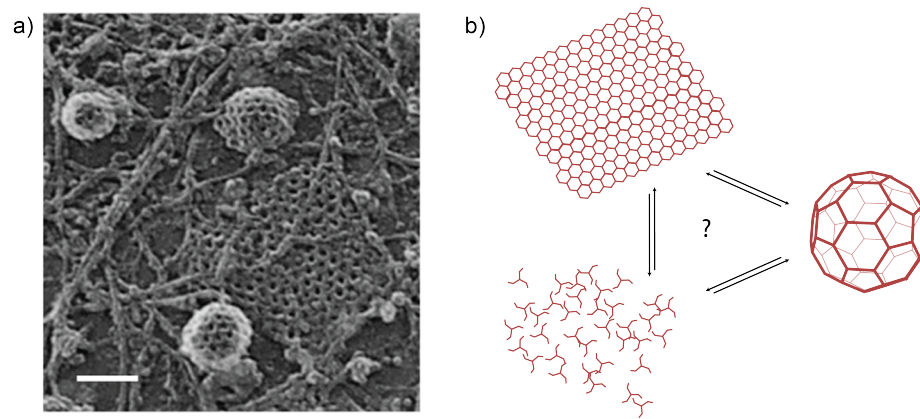
Figure 13: a) Electron micrograph of the inner leaflet of the plasma membrane from HeLa cells shows hexagonal arrays and icosahedral clathrin coated buds, scale bar 100 nm; kindly provided by P. Dannhauser. b) The observation of hexagonal lattices generates two hypothesis for the clathrin cage initiation process: I) formation of cages from the flat lattice, II) formation of cages from free triskelia.

fluctuations [61]. An interesting mechanism was proposed by Kirchhausen, who states that the flat clathrin lattices might serve as a triskelion reservoirs, and via the lattice disassembly at its sides, a high local concentration of triskelia can be achieved [62].

In order for clathrin to interact with the lipid bilayer, adaptor proteins are necessary. One of the most dominant proteins from this group is the heterotetrameric adaptor protein (AP) complex [62, 63]. Depending on which membrane and, therefore, in which pathway the coated vesicle is formed, a different AP complex links the specific membrane to clathrin (AP1 binds clathrin to the membrane of the trans golgi network, and AP2 to the plasma membrane) [64, 65]. So far it is not clear whether APs are needed for initiation of the pit or for driving the polymerization [62]. In 1999 Huang et al. showed that even without functional AP complexes, coated vesicle formation can still occur [66]. In contrast, in 2001 Ford et al showed that the minimal components needed for successful membrane invagination are AP2, phosphatidylinositol 4,5-bisphosphate (PtdIns(4,5)P$_2$) and AP180 [67]. The factor AP180 is known to drive the polymerization [68] and is also thought to regulate the size of the coated vesicles [69].

Another adaptor protein family, which can bind clathrin to epidermal growth factor substrate 15 (EPS15, which binds to AP2) and which can furthermore bind clathrin

directly to AP2, is epsin [70, 71, 72, 73]. A highly conserved part of epsin proteins is the epsin amino-terminal homology (ENTH) domain, which can bind to PtdIns(4,5)P$_2$ [67, 74] on one hand, and can interact with the membrane due to its amphipathic helix on the other. Therefore, it was thought to largely contribute to membrane invagination [75]. However, by removing the ENTH domain from epsin, Dannhauser & Ungewickell showed that clathrin polymerization alone is able to provide the driving force for creating coated vesicles [76].

At the very end of the vesicle formation process, a GTPase containing protein called dynamin, is necessary to separate the vesicle from its membrane of origin [77, 78]. Finally, after scission of the coated vesicle, the clathrin network needs to be disassembled in order to be recycled, as well as to provide a free lipid vesicle, which can then fuse with the endosomal system [79]. Under physiological conditions this uncoating step is facilitated by a member of the heat shock cognate 70 (Hsc70) protein family, via consumption of ATP (therefore also called "uncoating ATPase") [80]. These Hsc70 proteins are known to shift the unfolding equilibrium of other proteins by stabilizing their unfolded state [62]. To obtain sufficient vesicle uncoating an additional protein, named auxilin, is needed, in order to recruit and activate Hsc70 [79, 81]. More precisely, the J-domain of auxilin, which spans residues 547-910, is needed to promote Hsc70 activity [82, 83]. Auxilin is known to bind to the C-terminus of clathrin and is thought to recruit Hsc70 to sites of critical clathrin interactions [84, 85]. Moreover, Fotin showed that local changes to the clathrin contacts occur upon auxilin binding, which promote coat disassembly [84]. After successful uncoating, the triskelia can be recycled for the next membrane invagination.

3.2.1 *Clathrin and Membrane Bending*

In order to produce transport vesicles for intracellular trafficking, lipid bilayers need to be bent for a limited time period. The essential bending can be performed, as discussed above, by scaffold proteins, which do not attach directly to the membrane [86, 87]. In addition to clathrin [61], COPI and COPII are also cage forming proteins [88]. Phosphoinositides play an important role in the connection of coat proteins to the membrane since their headgroups can be easily modified [86]. For clathrin, as mentioned before, PtdIns(4,5)P$_2$ represents one of the key linkage points, and enables the connection of clathrin to the membrane via adaptor proteins [67, 89, 90].

In order to form vesicles, there are two energy barriers which need to be overcome;

the energy for membrane bending and for membrane stretching [91, 92]. The energy needed for bending a certain membrane area is 10–100 times higher than for stretching, and bending rigidities were determined to be around $10\,k_B T$ for soft fluid membranes, and $50\,k_B T$ for membranes with 50 % cholesterol [87, 93]. In general it is thought that the bending energy needed to form a naturally occurring 100 nm lipid vesicles is between $0.008\,k_B T/nm^2$ and $0.04\,k_B T/nm^2$ [87].

Simulations by Otter & Briels in 2011 predicted a binding energy of $25\,k_B T$ per triskelion [94], which was experimentally confirmed by Saleem et al. in 2015, who measured a binding energy per triskelion of around $23\,k_B T$ [95]. Considering that one triskelion occupies a surface area of around $300\,nm^2$ [54], this would indicate that a single triskelion contributes approximately $0.08\,k_B T/nm^2$ to membrane bending [87].

Regarding the biological function of clathrin, this work will use an artificial clathrin lattice as a minimal system to study the triskelion orientation inside a single pore, as well as to shed light into the role of the CLC in clathrin stability.

BIO-NANOTECHNOLOGY

The field of nanotechnology exists since several decades and describes systems with dimensions on the order of 10^{-9} m [96]. Here, the demand is high for new materials [97, 98], in order to create designs for applications such as data storage, efficient synthesis, drug transport and nano-electronics. To tackle these tasks, merging the fields of physics, chemistry and biology came a long way and showed tremendous advances. Although a lot of promising non-biological systems, such as carbon nanotubes [99], were developed, this work focuses on biological approaches in the field of bionanotechnology.

4.1 DNA BASED NANOTECHNOLOGY

Unsurprisingly, throughout the recent years a great part of the bionanotechnology research has been based on the employment of DNA. By taking the advantage of single stranded-overhangs at the sides of double-stranded DNA, so called sticky ends, many beneficial properties, such as predictability and diversity are achieved [100]. Furthermore, synthesizing the proper sequence enables to design branched DNA molecules [101], which can be used to generate 3D topographies [102, 103]. Additionally to 3D structures, DNA can be used to from 2D lattices [104] and aperiodic patterns [105].

In a more advanced approach, in 2006 Rothemund demonstrated a way to use a long single-stranded DNA and short "staple strands" to produce 2D nano shapes and patterns, which can later on be used to form larger assemblies [106]. This method, widely known as "DNA origami", was later on extended to form 3D objects [107, 108] and dynamic designs [109].

These DNA structures have found various uses, such as transport vesicles for drugs, and it was shown in numerous attempts that these designs can be used to immobilize and organize nanoparticles [110, 111, 112, 113] as well as proteins [114, 115, 116]. However, the efficient integration of proteins remains a particular challenge because

of lag in chemical diversity for functionalization [117].

4.2 PROTEIN BASED NANOTECHNOLOGY

Although DNA has traditionally found more attention as biological building blocks in bionanotechnology [118], peptides and proteins also provide promising properties for nanotechnological designs. In comparison to DNA the vast variety of proteins represents an obvious advantage. Moreover, they offer additional benefits, such as their high specificity towards target binding and their self-assemble capability into large scale shapes (e.g. S-layers, discussed below) [118]. Despite the more focused research on using DNA for bionanotechnological approaches, several attempts have been made to apply proteins for such use.

One of these approaches uses viral envelopes (capsids) as a nanotechnological tool. It has been shown that capsids of different viruses can be facilitated as scaffolds to create nanomaterials [119], as nanoreactors [120] or as packaging and transport vesicles [121, 122].

Aside from capsids, β-structured fibers of viruses have also been used, which in nature enable the attachment of the virus to its host cell [123]. A major benefit of these molecules is their evolutionary adaptation to harsh extracellular environments, rendering these proteins more stable than the majority of other proteins [124]. However, their structural complexity, as well as their potential to aggregate, makes them difficult to handle [125].

Other fibrous protein assemblies, which are thoroughly discussed in literature, are amyloid fibrils (Fig. 14 a). These fibrils are protein products that occur due to misfolding and aggregation, and can be associated to several diseases such as Alzheimer's and Parkinson's [126, 127, 128]. Comparable to the virus filaments, amyloid fibrils tend to be extremely stable in solution. Furthermore, they form organized structures of β-strands with a diameter of around 8 nm and a length of up to several μm [129, 130, 131]. Their ability to bind to both, hydrophilic and hydrophobic surfaces [132, 133], makes them naturally adhesive [131, 134], which renders them to interesting building blocks for material functionalization. Recently Li et al., for example, showed that by using amyloid fibrils together with graphene a biodegradable composite can be produced [133]. Nonetheless, the same authors reveal in a later review that to form these functional composites is far from trivial because changes in the

carbon architecture can either promote or inhibit fibrilation [135].

Besides the above mentioned proteins, one of the most promising protein structures
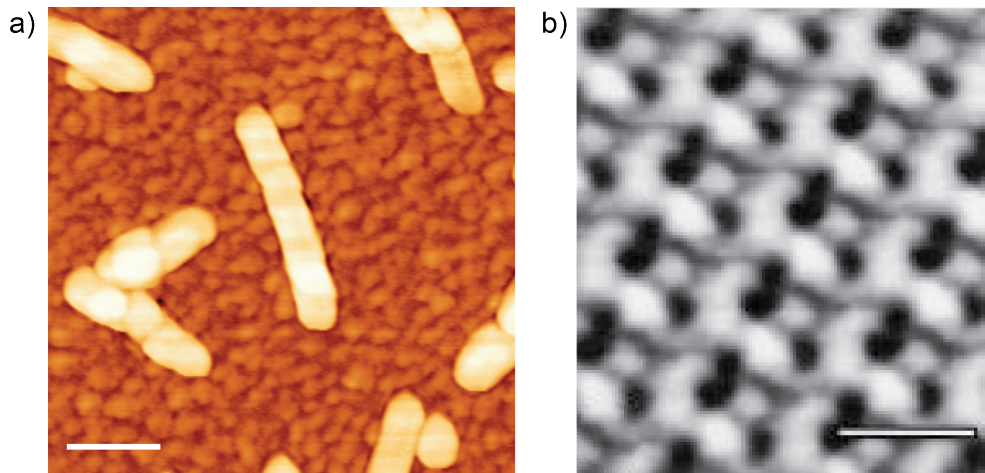
Figure 14: a) AFM scan of insulin amyloid fibrils [136], scale bar 100 nm. b) AFM image of the S-layer surface, scale bar 10 nm; adapted from [137].

for usage in material functionalization are the so called S-layer proteins [138]. This very regular and highly porous (glyco)protein layer is expressed by a variety of prokaryotic organisms, and it covers their surfaces (Fig. 14 b) [139]. These arrays can self-assemble with different lattice symmetries, showing unit cell dimensions of 3 - 30 nm and a thickness between 5 nm and 20 nm [137, 140]. Weigert & Sára showed already in 1995 that these arrays can be used as filters with extremely small pores (2 nm – 8 nm [137]) and , utilizing their periodically spaced carboxyl-groups [141], these filters can be additionally functionalized [142]. Furthermore, these layers have been shown to be a versatile tool for many nanotechnological approaches, e.g. for material functionalization, as matrices for biosensors, and as matrices for biomineralization [143].

An entirely different strategy for the utilization of proteins for nanotechnological applications was reported by Sinclair et al. in 2011. They presented a completely engineered approach in which they designed proteins with specific linker sequences, enabling them to assemble into big protein arrays (1D – 3D) and named them "Crysalins" [144].

4.2.1   *Clathrin in Nanotechnology*

So far only little has been done to take advantage of the highly structured and self-assemblying protein clathrin for nanotechnological uses. Schoen et al. demonstrated in 2011 a so called "Template Engineering Through Epitope Recognition" strategy, which relies on the binding of engineered peptides to epitopes of the clathrin cage. These peptides enable in turn the coverage of the cages with specific inorganic materials, which turns the clathrin cages into nanoparticles (Fig. 15) [145].
Another approach was to use CHC with hexahistidines attached to their N-terminus,
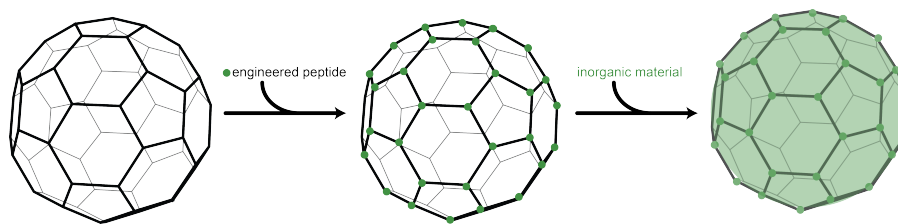
Figure 15: Clathrin cages, together with engineered peptides, can act as scaffolds. The peptides serve as seeding points to form inorganic nanoparticles; Illustration based on [145]

in order to control the formation of uniform gold nanocrystals along the cage structure [146].

The bionanotechnology related part in this work diverges from using the whole cage as a template for nanomaterials and focuses instead on the use of a 2D lattice for the modification and functionalization of surfaces. The kinetics, stabilization and controlled disassembly of the clathrin array, as well as the coverage of the lattice with inorganic particles and active biomolecules are described.

Part II

MATERIALS & METHODS

IMAGING & MECHANICAL MEASUREMENTS

1.1 ELECTRON MICROSCOPY

All electron microscopy images in this thesis were recorded and kindly provided by P. Dannhauser.

The freshly assembled clathrin lattices were fixed with 3 % glutaraldehyde for 10 min and negatively stained with 5 % uranyl acetate, analogous to lattice stabilization (section 4.2.1). Exceptions were the samples on glass and aluminum, which were critical point dried and processed by PT/C- shadowing, as described by Hinrichsen et al. [147].
After sample preparation, the images were obtained using a Tecnai^{TM} G2 (FEI) electron microscope with an acceleration voltage of 200 kV or a Morgagni^{TM} (FEI) electron microscope at 80 kV.

1.2 AFM IMAGING

To investigate the clathrin lattices using AFM, the samples were generally assembled onto HOPG as described in section 4.2, and fixed with 0.1 % glutaraldehyde for 20 min. The fixed samples were imaged using a "Cervantes Full Mode AFM System" (Nanotec, Spain). The standard cantilever for imaging in liquid was AC40TS (f_0 = 100 kHz, k = 0.1 N/m; Olympus, Japan). To record the images used for superposition and averaging of the pore the MSNL, cantilever E (f_0 = 38 kHz, k = 0.1 N/m, tip < 2 nm; Bruker, USA) was used. To image the dehydrated lattice in air, the OMCL-AC240TS cantilever was used (f_0 = 70 kHz, k = 1.7 N/m; Olympus, Japan). A controllable imaging force was achieved by using the "Jumping Mode Plus" [148] (jump off: 100 nm, sample points: 50, control cycles: 4). This allowed to image with forces between 0.2 nN and several nN. A usual scan area had a size of 1 μm x 1 μm and was recorded with 256 x 256 points and lines.

1.3 CALIBRATION OF THE AFM CANTILEVER

In order to calibrate the AFM system and to calculate the cantilever's spring constant, a force distance curve on a hard, non-deformable substrate (e.g. glass) was recorded. A linear fit to its extension curve represents the sensitivity of the system (nm/V). To further determine the spring constant of the cantilever the thermal noise spectrum was used, as described in more detail by Burnham et al. [149]. Here, the recorded thermal noise of the cantilever away from the surface, was transformed into its power spectral density (PSD). To the first peak of the PSD, representing the first eigenmode of the cantilever, we fitted the following modified Lorentzian function (Fig. 16):

$$S_{(f)} = \frac{A}{f} + B + \frac{S_0 f_0^4}{Q^2(f_0^2 - f^2)^2 + (f_0 f)^2},$$ (8)

where A and B are pink and white noise, respectively, S_0 is the amplitude, f_0 the resonance frequency and Q represents the quality factor of the resonance peak. The obtained fit parameters can be used to calculate the cantilever's spring constant via:

$$k = \frac{2k_B T Q}{\pi S_0 f_0},$$ (9)

where k is the spring constant, k_B the Boltzmann constant and the temperature is represented by T.

1.4 FORCE MAPS

Force maps were recorded from clathrin lattices on graphite coated electron microscopy grids. For this investigation the "Cervantes Full Mode AFM System" (Nanotec, Spain) and MSNL, cantilever E (f_0 = 38 kHz, k = 0.1 N/m, tip < 2 nm; Bruker, USA) were used. Force maps with 128 x 128 force curves were obtained by using sinusoidal accelerations of the Z-piezo, which allowed relatively fast scanning. A complete scan of a 500 nm x 500 nm area was acquired in approximately 3 min to 4 min using a ramp of -80 nm, 40 points and a set point of 1.2 nN.

The recorded force maps were used to calculate topographical height images at specific forces by extracting the contact part from each curve (point at which cantilever
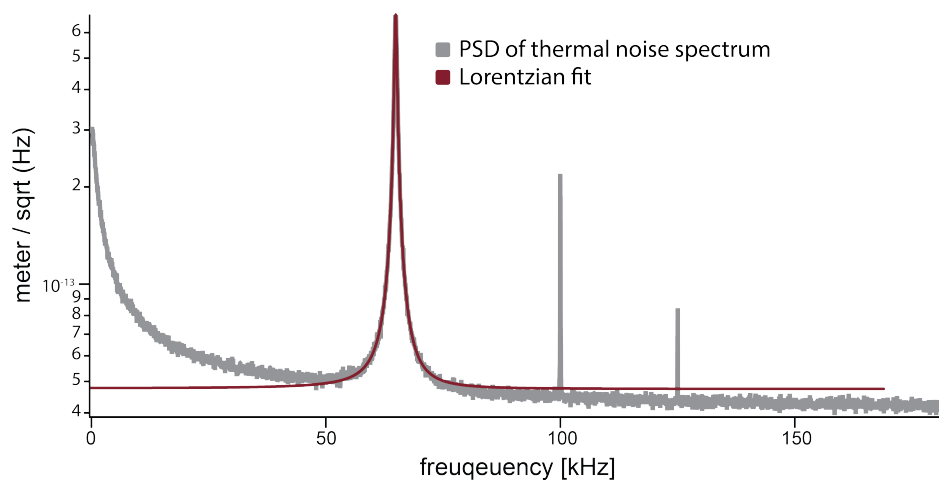
Figure 16: PSD of thermal cantilever noise with Lorentzian fit at its first eigenmode peak.

starts to bend). Subsequently, the Z-piezo movement was interpolated to find the best point in the deflection representing the desired force.

1.5 CAGE MECHANICS

The mechanics of, onto HOPG adsorbed, native and CHC clathrin cages were probed using an Asylum Research MFP 3D AFM and OMCL-TR400PSA cantilever (f_0 = 34 kHz, k = 0.08 N/m; Olympus, Japan). The cages were identified by scanning 1 μm x 1 μm areas, and in a second step a single cage was centered in a 300 nm x 300 nm scan (using amplitude modulation). The centered cage was indented with a trigger force of 3 nN, and with two different indentation speeds (0.9 μm/s and 2 μm/s), in order to rule out viscous effects.

1.5.1 *Analysis of Cage Mechanics*

The recorded force distance curves were converted to force-indentation curves by subtracting the slope of an extension curve on an indeformable substrate. This conversion enables to correlate the applied forces with the cage indentations/ deformations. Subsequently, a linear function was fitted to the extension curves of the cages from contact to 1 nN. The resulting slope represents the effective spring constant of the clathrin cages.

To analyze the area between the extension curve and the retraction curve, a MATLAB routine was written (appendix 2.3). Here the binary *.ibw files were read in using a function written by Jason Bemis. The data was plotted and the lower and upper limits for the area calculation were selected. Trapezoidal numerical integration was used to calculate the area under the extension and retraction curves. To calculate the final area in between the two curves, the area under the retraction curve was subtracted from the area under the extension curve.

IMAGE ANALYSIS

2.1 LATTICE HEIGHT

The height analysis of the clathrin lattices was performed via a home written MAT-LAB script (appendix 2.1). Namely, the height values, extracted from each image, were sorted and 2.5 % of the data was cut off from each side (lowest and highest points), in order to dismiss outliers. The remaining data was plotted into a histogram of 100 bins and the height of the lattice was defined as the difference between the maximum and the minimum height values of the histogram.

2.2 SURFACE CURVATURE

To quantify the surface curvature, on which native clathrin is able and CHC clathrin is unable to form lattices, we used AFM images from clathrin networks on carbon coated electron microscopy grids. These grids show partially uneven areas from which surface scans with concave curvature were selected. MATLAB was used to smoothen the height-profiles across the concave areas and a parabola was fitted into the obtained curve (appendix 2.2). Equation 10 was used to calculate the radius of curvature (R).

$$R = \frac{\left[1 + \left(\frac{dy}{dx}\right)^2\right]^{3/2}}{\left|\frac{d^2y}{dx^2}\right|} \tag{10}$$

For a parabolic function,

$$y = ax^2 + bx + c \tag{11}$$

the radius of curvature was calculated around the minimum of the parabola via:

$$R = \frac{\left[1 + (2ax + b)^2\right]^{3/2}}{|2a|} \tag{12}$$

2.3 SUPERPOSITION AND AVERAGING

The images of clathrin lattices for the averaging were obtained by using an Asylum Research MFP3D AFM and MSNL, cantilever E (f_0 = 38 kHz, k = 0.1 N/m, tip < 2 nm; Bruker, USA) in amplitude modulation with an amplitude of around 5 nm and low forces (around 30 pN), as described by Schaap et al. [150]. Sections displaying a single hexagon in the middle, surround by six further hexagons, were isolated. Six of these selections were used, and from each of these sections six copies were created via rotation by 60° (using the pores sixfold symmetry).
The images were superimposed in an iterative process in which each image was shifted and rotated to find the least square error with respect to the first (template) image (see equation 13).

$$f := min \left\{ \frac{1}{N} (b[i,j] - c[i,j])^2 \right\} \tag{13}$$

Hereby, $b[i,j]$ represents the pixel information of the template image and $c[i,j]$ are the image values of the current image, which is superimposed to the template. After 15 iterations all superimposed images were averaged to generate a final, high resolution image.

2.4 RELATIVE QUALITY OF CLATHRIN LATTICES

To quantify the quality of a lattice, in order to be able to determine best assembly conditions, assembly kinetics, and to quantify degradation processes, multiple electron micrographs of each condition were selected. The selection was based on the overall contrast of each image which had to be comparable to all other images in the set. The software WSxM [151] was used for image flattening and fast fourier transformation (FFT). Depending on the quality of the lattice, the FFT shows a ring at around 0.035 nm^{-1} (Fig. 17), which corresponds to the periodicity of the hexagonal lattice

(30 nm pore diameter). Further, the radial average of this FFTs was calculated, show-
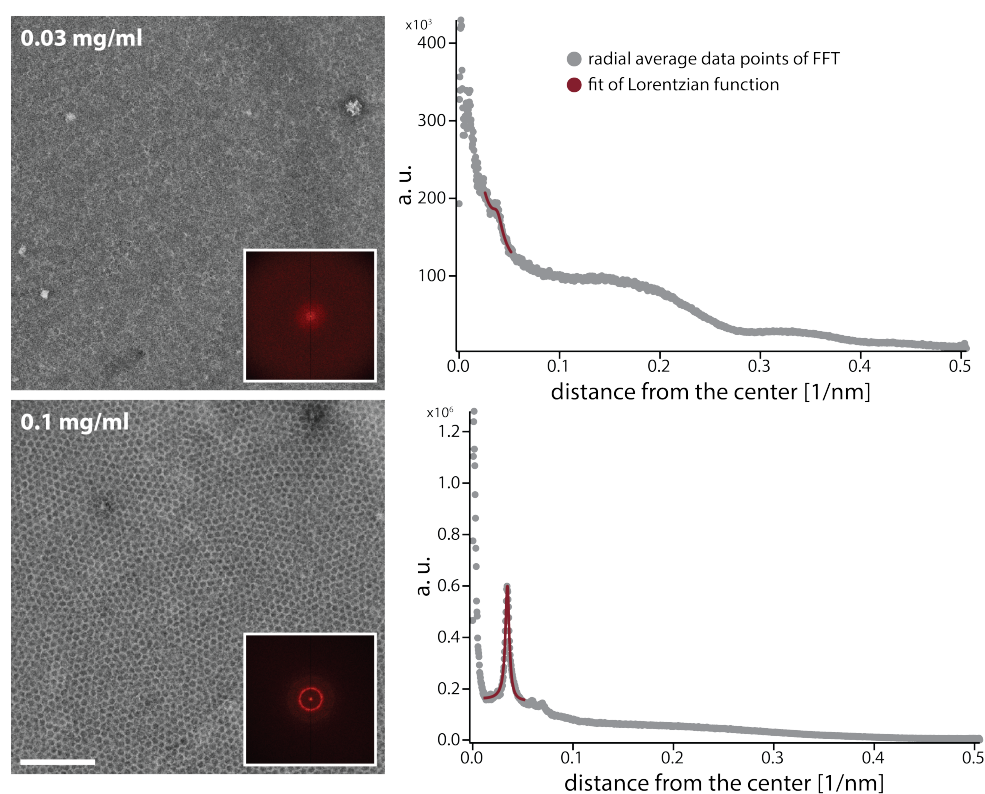
Figure 17: Two electron microscopy images of clathrin lattice assemblies from different triskelia concentrations; scale bar 300 nm. Inlays are the respective FFT. The graphs show the radial average of the FFT with a Lorentzian fit to determine the peak height with respect to the background.

ing a distinct peak at $0.035 \, \text{nm}^{-1}$ for lattices of high quality. To this peak a modified Lorentzian function (equation 8) was fitted to obtain the peak height with respect to the background noise (S_0), using Igor Pro (WaveMetrics). The height values were averaged for each condition, and the resulting highest value was considered to be an optimal lattice and lower values were normalized with respect to it.

2.5 GOLD PARTICLE QUANTIFICATION

To quantify the density of gold nanoparticles on the clathrin lattice, 14 to 19 200 nm x 200 nm areas of electron micrographs with different CLC to particle ratios were selected. The number of gold particles in these areas was determined and an average

density of the particle coverage for an area of 1 µm was estimated. These numbers were compared to the estimated number of triskelions inside a lattice as described in section 4.6.

SUSPENDED MICROCHANNEL RESONATOR (SMR)

All suspended microchannel resonator experiments were conducted in the group of Dr. Thomas Burg, together with Dr. Yu Wang.

3.1 SHORT INTRODUCTION TO SMR

The SMR setup shows similarities to the AFM setup and consists of a cantilever which deflection is measured by a laser system. Unlike in AFM, these cantilevers are hollow and can be used to weigh single nanoparticles, bacteria and sub-monolayers with very high resolution (fg regime) [152]. While particles pass through or attach to the cantilever's surface, they introduce a change in mass inside the micro-channel [152, 153, 154], which results in a change of the cantilever's resonance frequency according to equation 14 (Fig. 18):

$$f = \frac{1}{2\pi} \sqrt{\frac{k}{m^* + \alpha \Delta m}} \, , \tag{14}$$

with k representing the spring constant of the cantilever, m^* being the effective mass, Δm the added mass and α is a numerical constant (depending on the localization of Δm).

With respect to biological assembly processes, it was shown by Modena et al. and Wang et al. that SMR can be used to study the formation of amyloid fibirls [136, 155].

3.2 EXPERIMENTAL PROCEDURE

To analyze the kinetics of the clathrin lattice assembly, as well as to study the amount of bound molecules after the self-assembly, a SMR setup with a channel size of 3 μm x 8 μm x 144 μm (height, width, length) was used. For calibration, NaCl solutions with different densities were used and fitted with a linear regression, yielding the response in $fg/(\mu m^2\,Hz)$. The channels were cleaned and charged by flushing them with piranha solution (2:1 H_2SO_4 / H_2O_2) until a steady signal
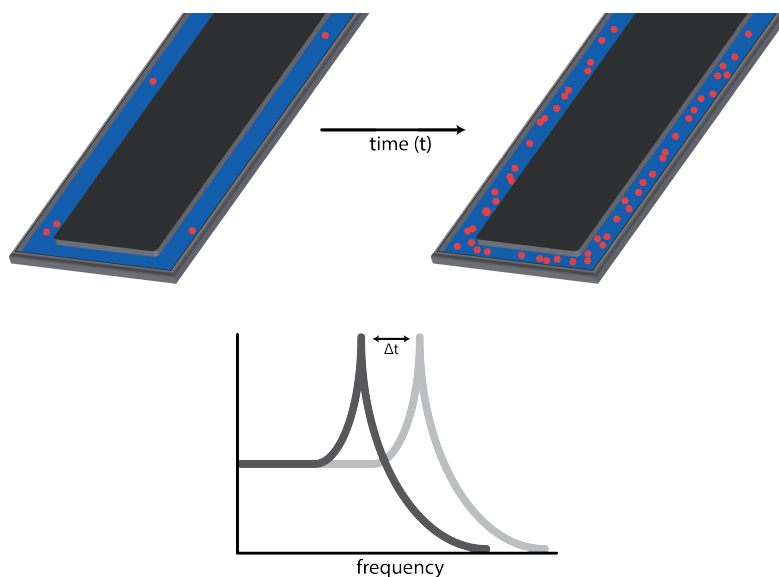
Figure 18: Illustration of the overall function of a SMR. Depicted is the hollow cantilever and the shift in resonance frequency upon addition of mass inside the cantilever; illustration based on [152].

was obtained. After equilibration with dH_2O, we subsequently injected buffer G, $H_6 - epsin^{144-575}$(0.83 μM), native (0.08 μM) or CHC triskelia (0.016 μM), followed by CLC triskelia (3.8 mM), and finally NaSCN (1 M), with a flow rate of around 1 nL/s. For each step the decrease in frequency was monitored until a steady state was reached.

3.3 DATA ANALYSIS

3.3.1 *Calculation of Masses and Number of Molecules*

To handle the huge amount of acquired data points, the data was down-sampled 100 times to 20 points per second. The mass changes were analyzed in MATLAB by calculating the frequency shifts between the corresponding baselines (e.g. difference between $H_6 - epsin^{144-575}$ baseline and triskelia baseline). These frequency shifts were multiplied with the calibration value (here 0.016 fg/Hz) to calculate the change in mass per μm^2. The change in mass per area could now be used to calculate the number of molecules per area.

For the calculation of the number of molecules per area, the buoyancy masses (m_b)

of the different molecules involved had to be calculated. For this purpose the widely accepted average density for proteins (ρ_p) of 1.35 g/cm^3 [156, 157, 158] was used. With ρ_p, the volumes of the molecules were calculated as follows:

$$V = \frac{m_m}{\rho_p},$$

(15)

where m_m represents the mass of a single molecule with respect to table 2. The

Table 2: Single molecule masses of peptides involved in the clathrin experiments

molecule	weight (g)
CHC triskelion	$7.1x10^{-19}$
CLC	$4.2x10^{-20}$
native triskelion	$8.0x10^{-19}$
$H_6 - epsin^{144-575}$	$7.2x10^{-20}$

buoyancy mass was then calculated by multiplying the molecule's volume with the density of the buffer (ρ_{liquid}), see equation 16.

$$m_b = V * \rho_{liquid}$$

(16)

Finally, the number of molecules per area was calculated by dividing the measured mass per area by the calculated buoyancy mass per molecule.

3.3.2 Determination of Time Constants

To access the time scales of clathrin assembly, the corresponding part of the curve was fitted with an double exponential function (equation 17) using Igor Pro.

$$f(x) = y_0 + A_1 \, exp \left[\frac{-(x - x_0)}{\tau_1} \right] + A_2 \, exp \left[\frac{-(x - x_0)}{\tau_2} \right]$$

(17)

The time constant τ_2 was considered to represent the assembly times.

PROTEIN & SAMPLE PREPARATION

4.1 PROTEIN PURIFICATION

All protein expression and purification was performed by P. Dannhauser, H. Böning and E. Ungewickell as described in [10, 11].

Rat brain $H_6 - epsin^{144-575}$ without ENTH domain was expressed and purified as described by Kalthoff et al. [159]. Clathrin light chain b with His-tag was created using a cDNA clone, provided by Frances Brodsky (UCL). Pig brain clathrin was purified by gel filtration [160]. The purified and reassembled clathrin cages were stored in 100 mM 2-(N-morpholino) - ethanesulfonic acid (MES), 1 mM EDTA, 0.5 mM $MgCl_2$, 2 mM $CaCl_2$ and 0.02 % NaN_3 at pH 6.4. After disassembly of the purified cages, triskelia were stored in 10 mM Tris-HCl and 0.02 % NaN_3 at pH 7.5. CHC triskelia and CLC from pig brain were purified as described by E. & H. Ungewickel [161] and by Winkler & Stanley [162]. The GST-CLC and GST-axuilin$^{813-910}$ were expressed and purified as described before [163, 164, 165]. Hsc70 from pig brains was purified as described by Schlossman et al. [80].

4.2 CLATHRIN LATTICE ASSEMBLY ON 2D SURFACES

Several substrates were investigated for clathrin lattice assembly: carbon coated formvar on copper grids (Science Services) [10], highly ordered pyrolytic graphite (HOPG, µmash), aluminum foil (Rubin, Rossmann), polyvinyl formal (formvar, PVF, Agar Scientific), glass (Thermo Scientific), and mica (Science Services).
These surfaces were charged by exposing them to air plasma (HARRICK PLASMA, USA) at highest RF level for approximately 5 min, with exception of the electron microscopy samples on modified copper grids. These samples were only shortly charged at an air pressure of 13 Pa and a current of 13 mA (Leybold - Hereaus Combitron CM30 and a Balzers BSV 080 Evaporation control unit). The charged surfaces were incubated for 30 min on top of a drop containing 0.83 µM $H_6 - epsin^{144-575}$ in

25 mM HEPES, 125 mM potassium acetate, and 5 mM magnesium acetate at pH 7.2 (buffer G). After a washing step, transferring the sample to two drops of buffer G, the $H_6 - epsin^{144-575}$ covered surfaces were transferred to a drop of buffer G containing 0.08 μM native triskelia or 0.016 μM CHC-only triskelia. Finally, the sample was washed as described before and further processed according to the experiment.

4.2.1 *Lattice Stabilization, Dehydration & Rehydration*

After a first fixation of the clathrin lattice with 0.1 % glutaraldehyde in buffer G, the samples were excessively rinsed with 100 mM MES, 1 mM EGTA, and 0.5 mM $MgCl_2$ at pH 6.4 (buffer A), in order to remove all acetate. Excess buffer A was aspirated and the sample was incubated with 5 % uranyl acetate (Polysciences) in H_2O for 1 min. Finally, excess uranyl acetate was aspirated using a moist filter paper and the sample was dried in air for several minutes, or under nitrogen flow.

In order to rehydrate the lattice, the sample was transferred to two drops of buffer A and incubated in an additional drop of buffer A for 2 min. Subsequently, the lattice was fixed once more with 0.1 % glutaraldehyde.

To modify the lattice with gold particles (described below, section 4.4.1), an extended incubation with buffer A was necessary to ensure complete uranyl acetate removal, and the fixation with 0.1 % glutaraldehyde was neglected.

4.3 CLATHRIN LATTICE DISASSEMBLY

Disassembly experiments were performed by P. Dannhauser.

In order to remove the clathrin lattice completely from the surface, the sample was incubated with 1 M NaSCN for 5 min. The surface was washed by transferring the sample subsequently to three droplets of buffer G. On the second drop, the sample was incubated for approximately 1 min.

To reassemble the lattice onto the uncoated surface, it was essential to excessively rinse it by transferring the sample to three droplets of buffer G. Finally, the cleaned surface could be incubated with 0.08 μM clathrin and 1 mg/ml BSA to reassemble the lattice.

4.4 LATTICE FUNCTIONALIZATION

The functionalization of clathrin lattices and imaging by electron microscopy was performed by P. Dannhauser und H. Böhning [11].

4.4.1 *Functionalization with Gold Nanoparticles*

Histidine tagged CLC b, in different concentrations (0.24 µM, 0.59 µM, 1.78 µM and 3.28 µM), were incubated with 0.078 µM of 5 nm gold nanoparticles (BBI-solutions, Cardiff, UK) in PBS for 5 min on ice. In order to remove excess CLC, the resulting constructs were diluted in 945 µl PBS with 2 mg/ml BSA and centrifuged at 90720 g (Optima TL100 ultracentrifuge, Beckman Coulter, Germany) for 15 min at 4 °C. After a second centrifugation step, the pellet was resuspended in 60 µl PBS containing 1 mg/ml BSA.

CHC lattices were fixed with 0.1 % glutaraldehyde in buffer G (10 min) and, subsequently quenched using 10 mM NH_4SO_4 and 0.1 % BSA in buffer G. The fixed lattices were incubated with the CLC coupled gold particles in buffer G, containing 10 mM NH_4SO_4 and 0.1 % BSA for 30 min, and subsequently processed for electron microscopy.

4.4.2 *Functionalization with J-Domain*

Using 1.25 M guanidinium hydrochloride (GndHCl), 42 mM sodium phosphate, 2 mM DTT and 2 mM EDTA at pH 7.0, GST-CLC and GST-auxilin[813−910] homodimers were dissociated. GST-auxilin[813−910] and GST-CLC monomers were mixed in a 2:1 ratio and the GndHCl was exchanged with PBS and 1 mM DTT using a PD10 desalting column. A Superdex 200 (GE Life Science) gel filtration column was used to enrich the GST-CLC/GST-auxilin[813−910] heterodimers.

The auxilin[813−910] modified CHC lattices were incubated with 1 µM Hsc70, 2 mM ATP, 5 mM creatine phosphate, 5 u/ml creatine phosphokinase and 1 mg/ml BSA in buffer G, for 10 min at 25°C. The reaction was stopped by transferring the sample onto a droplet containing 3 % glutaraldehyde in buffer G. Subsequently, the sample was further processed for electron microscopy.

4.5 CLATHRIN CAGE ADSORPTION

Clathrin cages were adsorbed on HOPG (pre-treated with air plasma for approximately 5 min). 0.05 mg/ml cages in buffer A were incubated on the surface for 1 min, washed by transferring the sample to two drops of buffer A and fixed with 0.2 % glutaraldehyde in buffer A for 10 min. Finally, the sample was washed once more by subsequently transferring it to two drops of buffer A.

4.6 ESTIMATION OF TRISKELIA PER μM^2

In order to estimate the coverage efficiency for the clathrin lattice functionalization with gold particles as well as to estimate the assembly efficiency in the SMR experiments, the number of lattice ribs and triskelia per μm^2 was calculated. Since the flat-to-flat distance in our hexagons is known (30 nm), equation 18 was used for this purpose:

$$A = \frac{\sqrt{3}}{2}d^2, \tag{18}$$

with A as surface area and d being the flat-to-flat distance. Considering that a hexagon has 6 sites (here 6 ribs) and each rib is composed of 2 hexagons, each hexagon provides 3 ribs to the overall structure of the lattice, and hence:

$$\frac{3}{A} = \frac{6}{\sqrt{3}}d^2, \tag{19}$$

which results in 3849 ribs / μm^2.

To calculate the number of triskelia per μm^2 we consider that 1 triskelion contributed to 3 ribs and 1 rib consists of 2 triskelia. Hence, $\frac{1}{3} * 2 = \frac{2}{3}$ triskelia are necessary to build up one rib. Therefore:

$$\frac{2}{3} * \frac{3}{A} = \frac{2}{A} = \frac{4}{\sqrt{3}}d^2, \tag{20}$$

resulting in 2566 triskelia / μm^2.

Part III

RESULTS

LATTICE ASSEMBLY

In order to study biological properties and mechanisms of clathrin protein networks in a minimal system, Philip Dannhauser and Ernst Ungewickell designed a protocol to produce a flat lattice on 2D substrates [10, 76]. Apart from their use for fundamental studies, these lattices inspired new directions for nanotechnological utilization [11].

1.1 ASSEMBLY OF CLATHRIN LATTICES

The formation of clathrin lattices requires a charged surface, which can generally be achieved by treating the desired surface with air plasma. The clathrin binding motifs of epsin ($H_6 - epsin^{144-575}$) are adsorbed onto this surface, which enables self-assembly of a clathrin network upon addition of purified triskelia (Fig. 19).

1.2 CLATHRIN ASSEMBLY CONCENTRATIONS

As shown by Pearse in 1981, a minimum concentration of $0.05\,mg/ml$ is needed for the self-assembly of clathrin baskets to take place [56]. In addition, a regulating effect of the CLC on clathrin cage assembly has been demonstrated [161, 166].

In order to study the effect of different triskelia concentrations (native and CHC-only), electron micrographs of lattices assembled with varying concentrations were recorded by P. Dannhauser (Fig. 20). Images with comparable contrast were analyzed by extracting the radial averages of their Fast Fourier Transform (FFT) (see Fig. 21). A Lorentzian function was fitted to the peak at $0.035\,nm^{-1}$ to determine the height of the peak with respect to the background noise. The peak represents the periodicity of the clathrin lattice and, therefore, it is more pronounced for high quality lattices. The normalized height was considered as relative quality of the lattice (Fig.
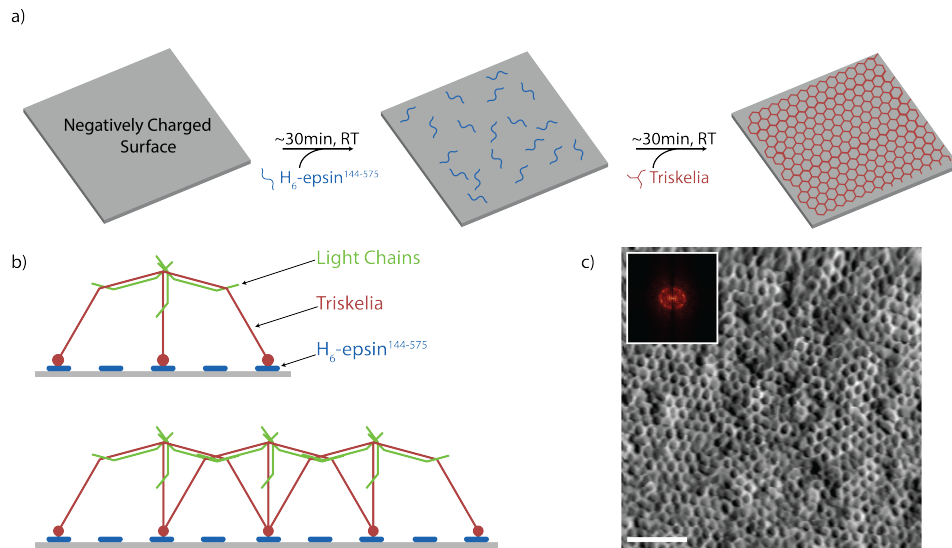
Figure 19: Assembly scheme of the clathrin lattice. a) Scheme of the assembly protocol. b) Sketch of the lattice cross-section [11]. c) AFM image of the clathrin lattice in air, inlay: FFT of the image representing the 30 nm pores, scale bar 200 nm.
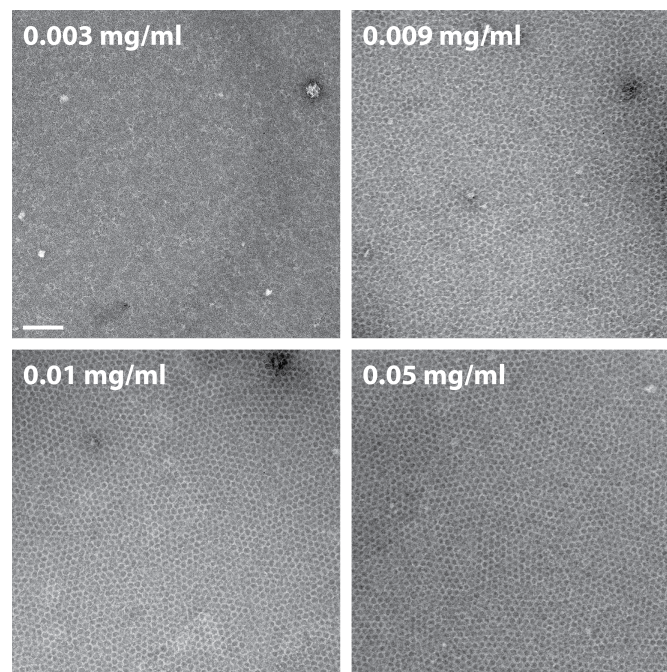
Figure 20: Electron microscopy images of native lattices assembled from different triskelia concentrations, scale bar 200 nm.
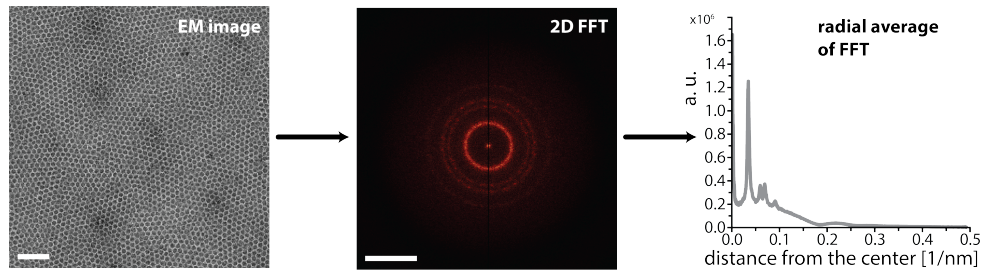
Figure 21: Electron micrographs with similar contrast were converted by FFT. From the resulting FFT images the radial average was calculated, which reveals a peak near $0.035\,\text{nm}^{-1}$, representing the lattice periodicity. Scale bar electron micrograph $200\,\text{nm}$, FFT image $0.08\,\text{nm}^{-1}$.

22).

This analysis revealed that a minimum concentration slightly above $0.01\,\text{mg/ml}$ is
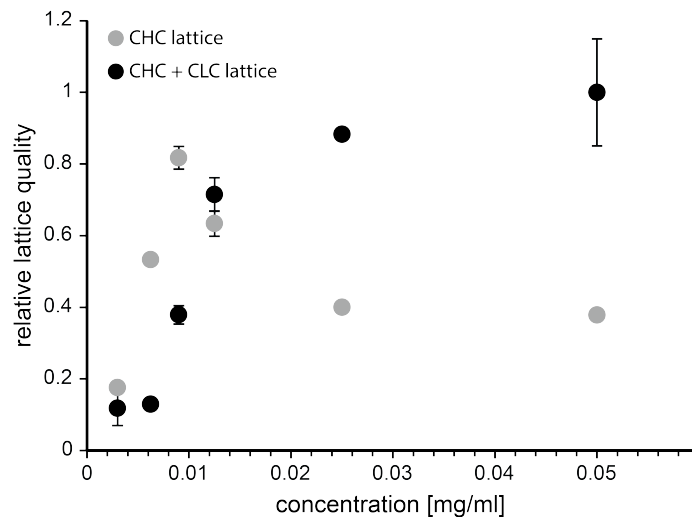
Figure 22: The lattice quality depends on the triskelia concentration. Analysis of the relative lattice quality by radial averaging of the FFT shows a maximum concentration for CHC lattices [10].

essential in order to form a full clathrin lattice with native triskelia (CHC + CLC). When using higher concentrations, only a slight increase in lattice quality was observed. Interestingly, when triskelia lacking CLC were used, a maximum lattice quality was reached at a concentration of $0.01\,\text{mg/ml}$. In this case an increase in the triskelia concentration resulted in a drop in lattice quality, supporting the previously shown regulating role of CLC in clathrin cage assembly [161, 166].

1.3 CLATHRIN ASSEMBLY KINETICS

The next step was to study the kinetics of the lattice assembly. For this purpose electron micrographs of the lattice state (native and CHC-only) for different time points were recorded (Fig. 23). The data analysis was analogous to that of the concentration
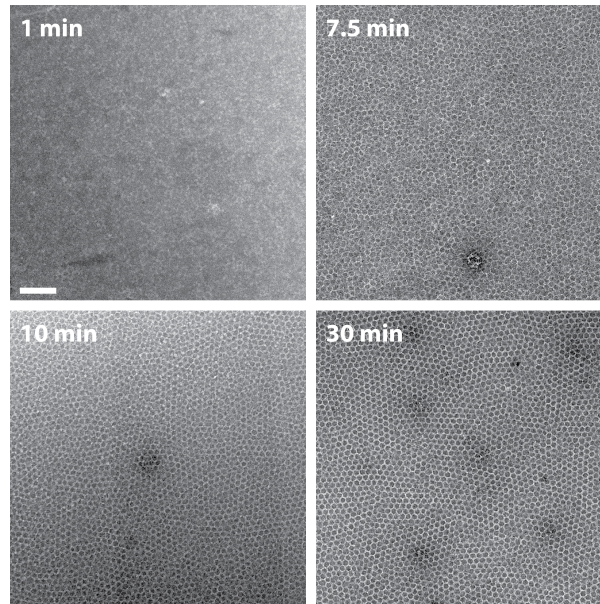
Figure 23: EM images of the clathrin lattices during self-assembly at different time points, scale bar 200 nm.

dependency. In order to be able to gain the best possible CHC lattice, the previously determined optimum concentration of 0.01 mg/ml CHC triskelia was used for the assembly kinetics investigations.

Figure 24 shows that a native lattice requires approximately 10 min to be fully assembled. After that time, only minor increases in lattice quality can be observed. The self-assembly of the CHC lattice appears to be slightly slower. Furthermore, the lattice quality remains slightly inferior to the one observed for native lattices.

In order to not only investigate static points in time but to follow the clathrin lattice assembly dynamically, a suspended microchannel resonator was used to temporally follow the assembly kinetics. Hereby, the change in effective mass (m_{eff}) of the resonator can be tracked by monitoring its resonance frequency (additional mass causes a reduction of the frequency, see methods 3.1) [152, 153, 154]. Figure 25 shows a usual recording from these experiments. In the beginning the baseline at 0 Hz represents the resonance frequency (or effective mass) of the hollow can-
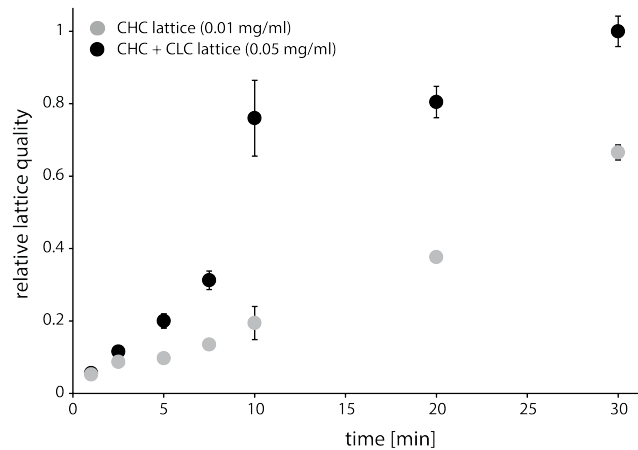
Figure 24: Analysis of the relative lattice quality by radial averaging of the FFT from the time series electron microscopy images reveals the assembly kinetics. The lattice needs around 10 min to fully assemble, only minor changes were noticeable with additional time [10].

tilever when filled with buffer G. Upon addition of $H_6 - \mathrm{epsin}^{144-575}$, the frequency slowly drops by 30 Hz and, hence, represents an increase in m_{eff} of 0.5 fg/µm^2(with 0.016 fg/Hz). Under consideration of $H_6 - \mathrm{epsin}^{144-575}$'s buoyancy mass (methods 3.3.1), this corresponds to a coverage of the cantilever surface with approximately 8800 $H_6 - \mathrm{epsin}^{144-575}$ molecules/µm^2. Addition of native triskelia reduces the frequency for another 50 Hz (additional m_{eff} increase of 0.8 fg/µm^2).

Averaging four of these experiments revealed a coverage of 760 native triskelion molecules/µm^2 (m_{eff} = 0.61 fg/µm^2), suggesting that approximately 30% of the resonator surface is covered with a clathrin lattice, compared to the theoretical value of 2566 molecules/µm^2 for a complete lattice (see methods 4.6).

In order to obtain the time needed for the triskelia to self-assemble into clathrin lattices, a double exponential function was fitted to the curve of frequency reduction upon triskelia addition (Fig. 26 a). The measured time constants for lattice self-assembly correlate very well with the kinetics observed in the electron microscopy analysis (Fig. 24). For the native lattice, a time constant of 20 min $\pm$ 13 min (SEM) was determined, and investigating the assembly of CHC-only lattices revealed a time constant of 31 min $\pm$ 6 min (SEM).

Interestingly, a single exponential fit was insufficient to successfully fit the curve of the frequency decay during triskelion adhesion and clathrin assembly (Fig. 26), and
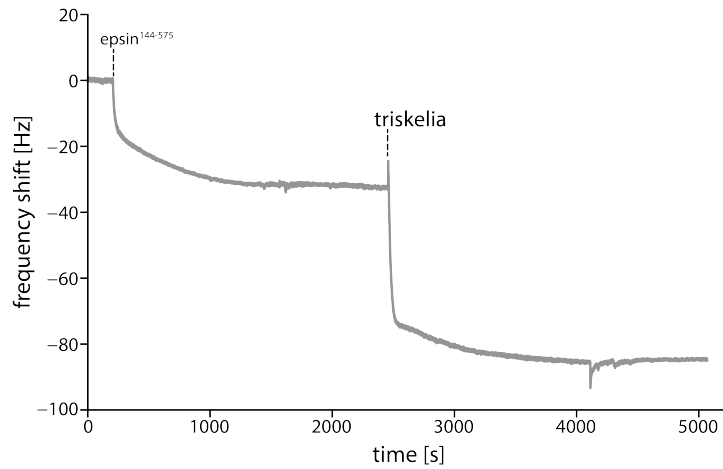
Figure 25: SMR experiments enable to follow the assembly kinetics by monitoring the decrease in resonance frequency due to changes in the effective mass (m_{eff}) of the resonator. The experiments were conducted in the group of Dr. Thomas Burg, together with Dr. Yu Wang.
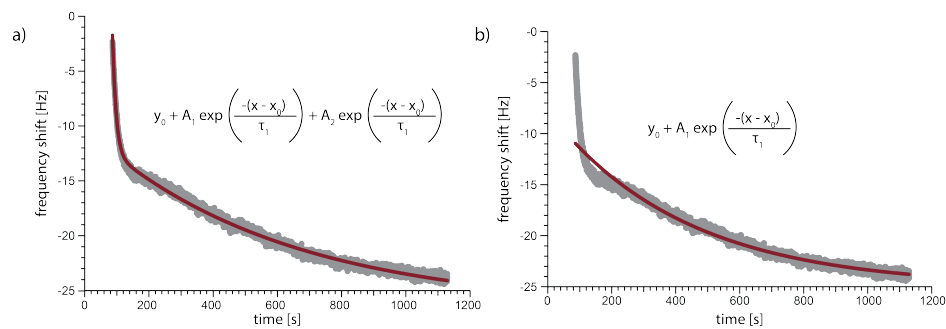
Figure 26: Fitting of the clathrin assembly curves. a) Double exponential fit follows the recorded data very well. b) Whereas, a single exponential fit is unable to trace the data.

raised suspicion for a two step process. Unfortunately, a single exponential fit is also insufficient to fit the curve obtained during the adhesion of $H_6 - epsin^{144-575}$ to the resonator's surface. Nonetheless, analyzing the trend of both curves, ignoring the first steep part, reveals a clear discrepancy between them (Fig. 27). While the shape
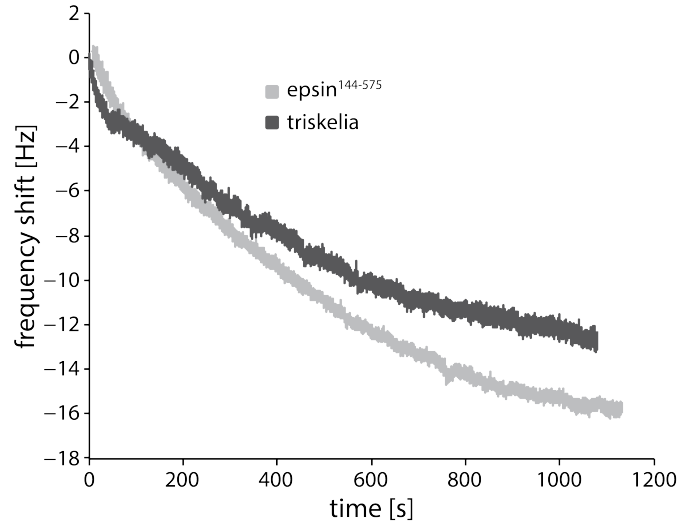
Figure 27: Comparison of a clathrin assembly curve to an epsin curve in the SMR experiments. The clathrin curve diverges drastically from a normal exponential curve and might therefore reveal a two step assembly mechanism.

of the frequency shift curve during $H_6 - epsin^{144-575}$ adhesion resembles closer to an exponential function, the clathrin assembly shows a different behavior between 100 s and around 400 s. This irregularity might be due to a mixture of adhesion, detachment and reorganization processes and, therefore, might indicate a two-step assembly process (first adhesion to the surface and, subsequently, a phase to organize the lattice).

CLATHRIN LATTICES FOR BIOLOGICAL STUDIES

Clathrin lattices are very convenient as minimal system to study some of the remaining fundamental biological questions in its field. To complement the already existing electron micrographs, the first objective was to establish high resolution AFM images. Finally the mechanical properties of the clathrin lattice were studied.

2.1 VARIATIONS IN THE PUCKER ANGLE

The AFM image quality was highly dependent on the imaging force (Fig. 28). The image obtained, while scanning the lattice at high force (in the nN range), displayed a well visible, albeit highly deformed hexagonal lattice. In contrast, scanning at low force (<100 pN) resulted in an image depicting a more natural lattice structure; however, its features appeared not well defined, due to the soft and flexible structure itself.

These results were insufficient for a close study of the hexagonal pore structure and the triskelion orientation within it. Therefore, the following processing had to be employed. To avoid deformations of the clathrin's native state the low scanning force images were used as a starting point. In order to increase the level of details and visible features of the hexagonal pore, the obtained 500 nm x 500 nm images of the lattice were cropped in a way that each fragment contains a single hexagon in the middle, surrounded by six adjacent hexagons. These image fragments were superimposed in iterative steps by shifting and rotating the individual fragments, in order to obtain the least square error between each image and the template (Fig. 29 a). The resulting averaged image displays a hexagonal pore with a height of approximately 12 nm. One of the most notable features were the clearly distinguishable vertices, which represent the hubs of the integrated triskelia. Between two vertices a dent of approximately 1 nm in depth could be measured, which allowed for calculations of the angle between the vertices and their legs, the so called pucker angle (Ψ) (Fig. 30). This angle, due to its fixed structure in the clathrin cage, as well as in single
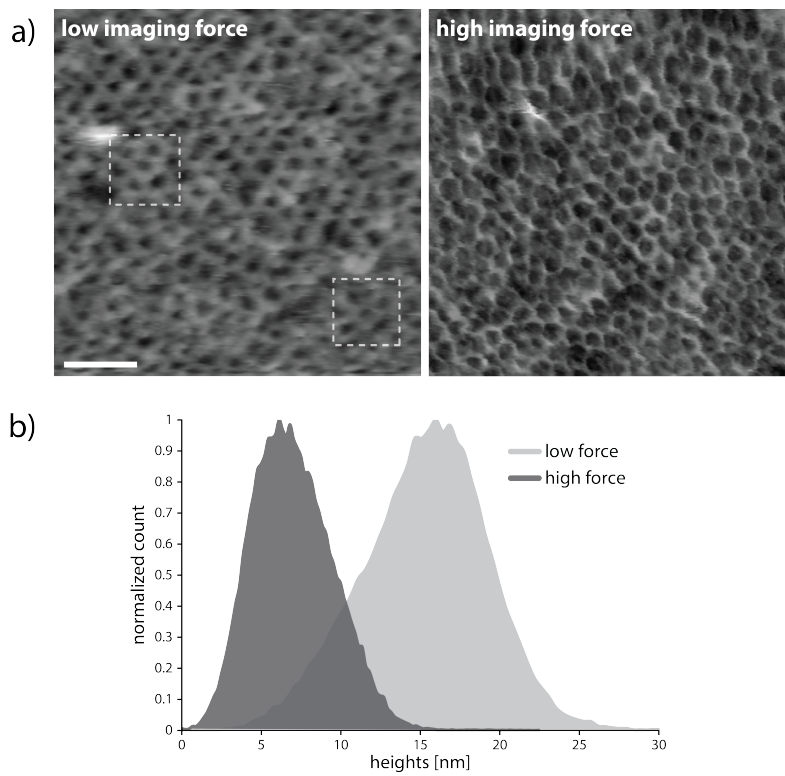
Figure 28: a) Imaging the clathrin lattice at high scanning forces (nN regime) results in a more pronounced, however, highly deformed structure. The deformation at lower forces (<100 pN) is reduced but the hexagonal structures are not as clear, scale bar 100 nm. b) Height histograms of the lattices at different scanning force.
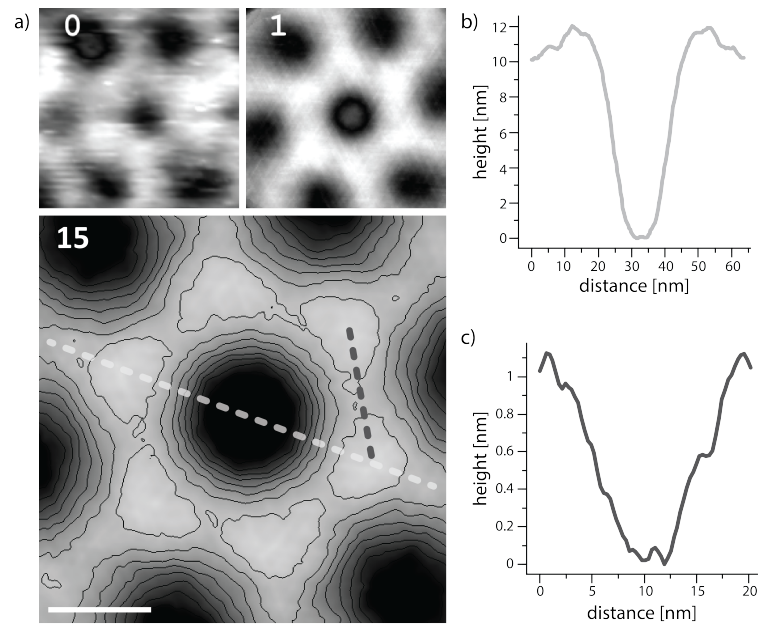
Figure 29: a) Superposition of AFM image fragments depicting a hexagonal pore: (0) raw image (0 iterations), (1) averaged image after 1 iteration, (15) final image after 15 iterations, scale bar 15 nm. b) & c) Depicting the height profiles as indicated in the final image. b) shows the profile across the pore, indicating a lattice height of 12 nm. The height profile in c) illustrates the dent between two vertices with a depth of 1 nm [10].

triskelia in solution, is generally thought to be invariant [54]. However, there are also suggestions that the pucker angle might change in a flat lattice [55]. Using a reconstruction of the clathrin cage from cryo-electron microscopy (PDB: 3IYV [54]) and triskelia reconstructions from X-ray diffraction data (PDB: 3LVG [167]), a pucker angle of around 70° was determined in these structures. A pucker angle of 70° however, would result in a dent between the vertices of approximately 3 nm, which is inconsistent with the findings from the averaged lattice pore. To accommodate a height difference of 1 nm between two vertices, the pucker angle needs to be around 83° (Fig. 30). This clearly indicates a certain flexibility of the pucker angle, which
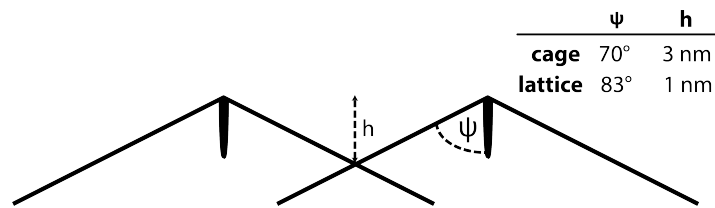
Figure 30: Sketch of two triskelia in the lattice (based on [54]) with indication of the dent between the vertices and the pucker angle between vertex and leg.

most probably plays a role in the ability of clathrin to assemble into both, 2D flat lattices, and 3D vesicle coats on the membrane.

2.2 INFLUENCE OF THE CLATHRIN LIGHT CHAINS ON LATTICE MECHANICS

The roles of the CLC in clathrin networks are still highly debated. As mentioned above, the CLC is associated with proper clathrin lattice assembly (i.e. decrease in CHC-only lattice quality at high triskelia concentrations, Fig. 22) [161, 166]. Nonetheless, it has been shown that endocytosis and vesicle coat formation can still occur after CLC depletion [168, 169]. It is even considered that the role of CLC is rather related to the communication with cytoplasmic structures than with a direct effect on the clathrin array [54]. However, considering that CLC depletion does have an effect on the pinwheel-like structure of the triskelia [170], in this work a role of the CLC in the lattice mechanics was assumed.

In order to investigate this, native lattices (CHC + CLC) as well as lattices consisting of solely clathrin heavy chains were created. Already during the process of imaging the CHC-only lattice using AFM, a difference in comparison to the native

lattice was observed. While it was possible to obtain relatively clear images of the native clathrin network at low imaging force, the CHC-only lattice exhibited a movement in scanning direction (Fig. 31 a). This deformation was a first indication for
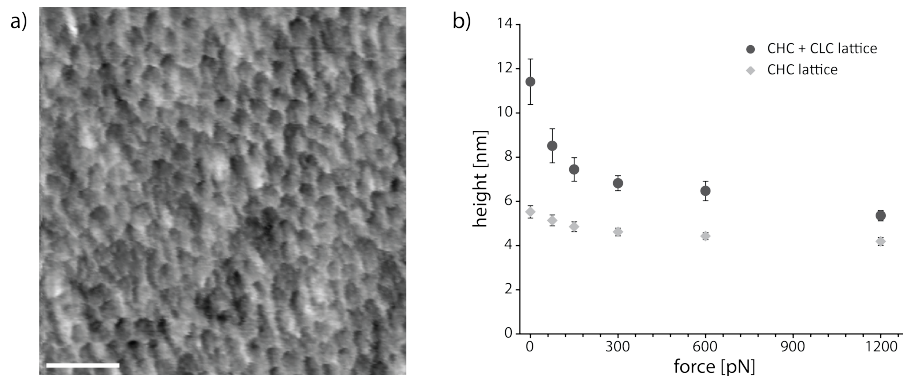
Figure 31: Influence of the CLC on the lattice mechanics. a) AFM image of a "smeared out" CHC-only lattice in liquid, indicating a more flexible lattice, scale bar 100nm. b) Height recalculation of force maps. The CHC-only lattice can not be pushed down, indicating a stabilizing role for the CLC, which allows the lattice to stand on its terminal domains [10].

a higher lattice flexibility. To investigate this hypothesis in more detail, force maps of 128x128 force curves with a trigger point of >1 nN were recorded. Topographical height images for imaging forces between 0 pN and 1200 pN were reconstructed from the force maps. These images reveal a native lattice height of around 12 nm, which was in good agreement with the lattice height obtained from the averaged pore. With increasing force, the height of the lattice drops drastically to around 6 nm (Fig. 31 b). In contrast, the CHC-only lattice shows already at 0 pN imaging force a height of around 5 nm, and is indeformable with increasing force, i.e. it is impossible to push the lattice closer to the substrate. This suggests that the CHC-only lattice is unstable and collapses, indicating a clear stabilizing influence of the CLC on the lattice, allowing it to stand on its terminal domains.

2.2.1 *Mechanics of Clathrin Cages*

In subsequent experiments, P. Dannhauser & E. Ungewickell could show that CLC-lacking clathrin is unable to bud vesicles at low temperatures [10]. Therefore, another aim of this work was to investigate CLC-lacking clathrin cages. To examine

the mechanical properties of native and CHC-only cages, several force curves for each subset of cages (heights between 60 nm and 70 nm) were recorded (Tab. 3). While there was no significant difference in the effective spring constant (k_{eff}) be-

Table 3: Effective spring constants of native and CHC-only cages at different indentation speeds

	CHC + CLC		**CHC**	
	2 μm / s	0.9 μm / s	2 μm / s	0.9 μm / s
mean k_{eff}	0.38	0.28	0.36	0.33
SEM	0.06	0.03	0.03	0.03
N	16	16	13	13

tween native and CHC-only cages, the difference between trace and retrace in native clathrin cages was more pronounced than in CHC-only cages (Fig. 32 a & b). The
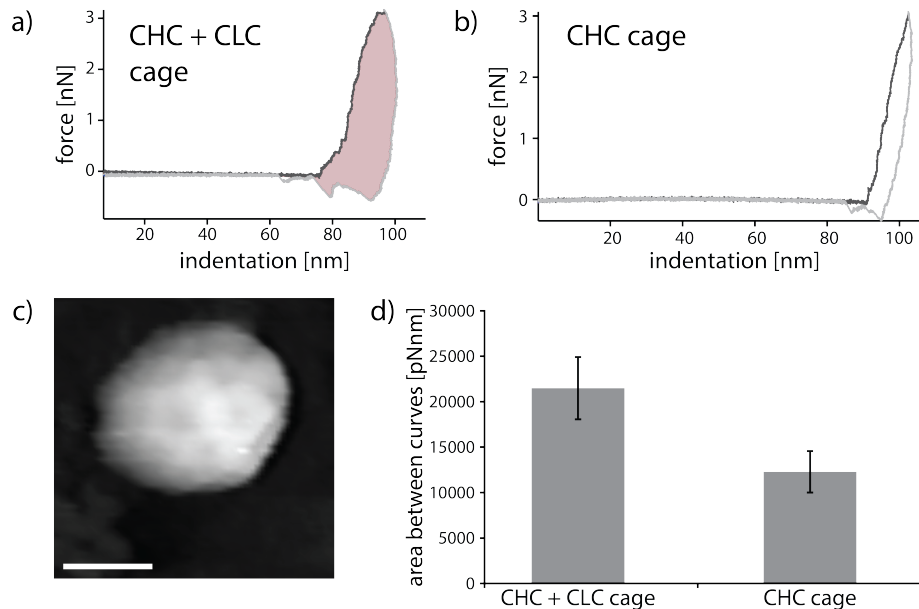
Figure 32: a) & b) Force curves on clathrin cages indicate different stability of native and CHC-only cages, illustrated by differences in their trace and retrace. c) AFM image of clathrin cage in liquid, scale bar 50nm. d) Calculation of the area between trace and retrace (indicated in a)) might suggest higher degree of defects in native cages upon indentation.

insignificant differences in k_{eff} when indenting the cages with high- (2 μm / s) and low- speed (0.9 μm / s) (Tab. 3) ensure that the divergence between trace and retrace

are not due to viscous effects. To further quantify these deviations, the area between the trace and retrace curves was calculated, as indicated in figure 32 a), which indeed shows a higher divergence for native cages (Fig. 32 d). This might indicate an increased breakage in crosslinking points, when indenting CLC-associated native cages.

CLATHRIN LATTICES FOR BIO-NANOTECHNOLOGY

Considering clathrin's highly ordered structure as well as its feature to span vast surface areas, the clathrin network represents a promising tool for bionanotechnological designs. In this work the first steps to introduce clathrin to this developing field were made.

3.1 FORMATION OF CLATHRIN LATTICES ON VARIOUS MATERIALS

In order for the clathrin lattice to be suitable for a variety of applications, it has to have the ability to assemble on different materials. In figure 33 a selection of surface
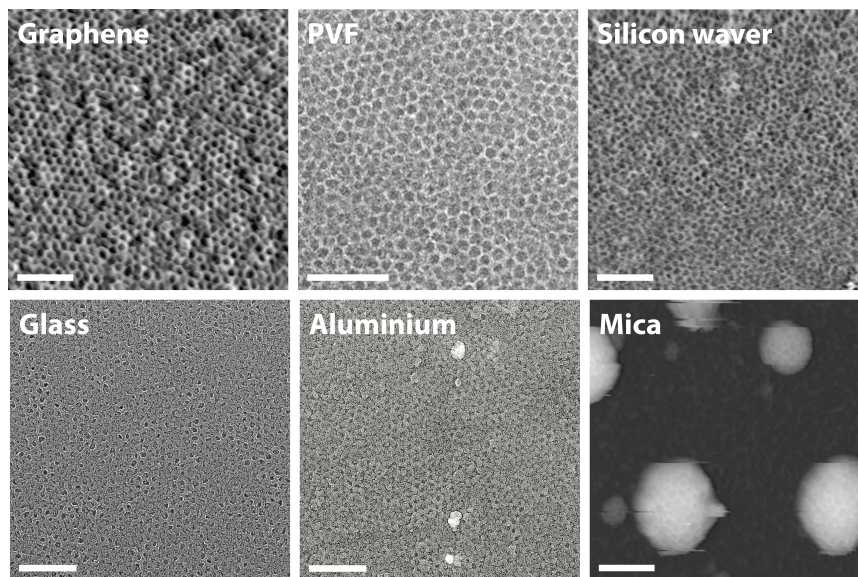
Figure 33: Clathrin lattices on different surface substrates, scale bar 200 nm [11].

materials that were investigated for clathrin assembly (including graphene, silicon, polymers, glass and metals) are shown. The clathrin lattice is able to successfully self-assemble on all tested surfaces, with the exception of mica, which seemed to

rather favor cage formation on slightly curved parts of the surface, than formation of flat lattices.

3.2 LATTICE FORMATION ON CURVED SURFACES

Imaging of the clathrin lattice on graphene-coated electron microscopy grids, revealed that native clathrin networks not only assemble on convex curved surfaces, but also on slightly concave parts (Fig. 34 a). In contrast, the assembly on areas with
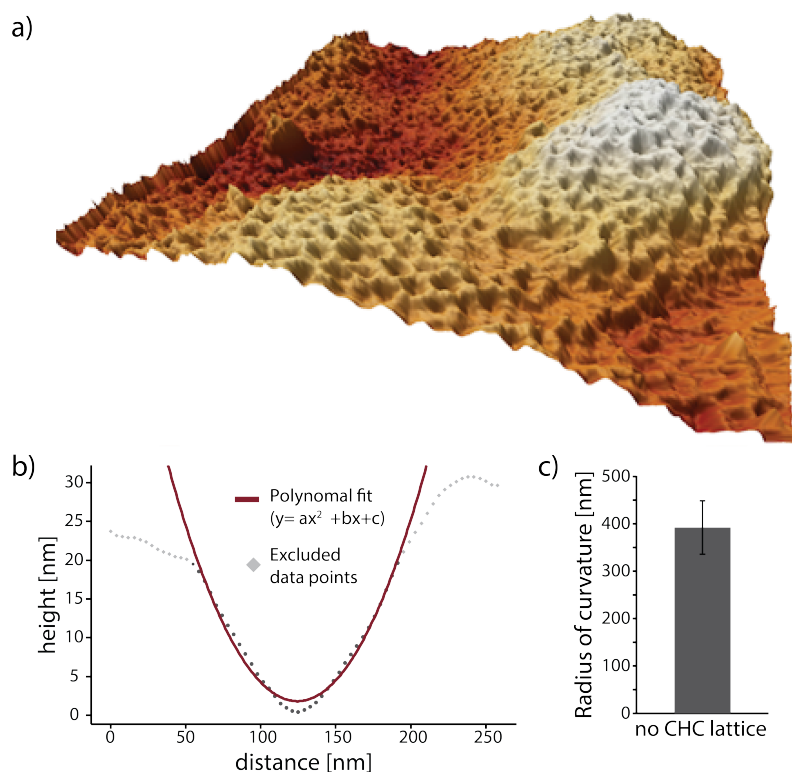
Figure 34: a) AFM image of a curved lattice in liquid. b) Height profile of an imaged native lattice assembled onto a concave area via AFM with polynomial fit. c) Radius of curvature of concave curved surfaces on which the CHC-only lattices was unable to form.

concave curvature appeared to be challenging for CHC-only triskelia. To investigate this in more detail, concave areas from AFM scans on which the CHC-only lattice was unable to assemble were examined. Each profile across these located areas was smoothed and fitted with a parabola (Fig. 34 b). The calculated radius of curvature around the parabolas' minimum shows clearly that at a radius of curvature of ap-

proximately 400 nm the CLC-lacking clathrin networks was unable to form (Fig. 34 c). Whereas, the native clathrin was found to be able to assemble arrays at concave surface areas with a similar radius of curvature.

3.3 DISASSEMBLY OF CLATHRIN LATTICES

To show that the lattice can be dynamically changed, and to make it suitable for cyclic applications, such as batch reactors, easy ways to uncoat the clathrin covered surfaces were investigated. A very straightforward method to disassemble the lattice is incubation with sodium thiocyanate (NaSCN). This chaotrophic salt is able to remove the assembled lattice; however, the surface bound $H_6 - epsin^{144-575}$ remains intact. Therefore, it is possible to immediately assemble a new lattice upon addition of fresh triskelia (Fig. 35 a). The disassembly of the clathrin network using NaSCN could also be observed via the SMR measurements (Fig. 35 b). Here, injection of 1 M NaSCN leads to a reduced effective mass due to clathrin unbinding and, hence, the frequency returns to the value measured after $H_6 - epsin^{144-575}$ binding. However, measuring subsequent binding of fresh triskelia was unsuccessful so far.

3.4 STABILIZATION & REHYDRATION OF CLATHRIN LATTICES

Freshly prepared clathrin lattices are only stable for tens of minutes at room temperature, if not further modified. Fixation with glutaraldehyde (0.1 %) can extend the stability up to weeks in solution. Here, we show that these glutaraldehyde fixed lattices can be further stabilized using 5 % uranyl acetate (UA). This enables the dehydration of the clathrin arrays and, therefore, makes them suitable for storage over several months. The dried clathrin lattices can be rehydrated using acetate free buffer (Fig. 36 a). As shown in figure 36 b, the lattice returns to its native state, illustrated by its height recovery after rehydration. Upon rehydration the lattice can be again stabilized using UA and it is possible to dehydrate it for a second time. However, the lattice appears to lose some stability, indicated by its reduced height, compared to the first dehydration step.
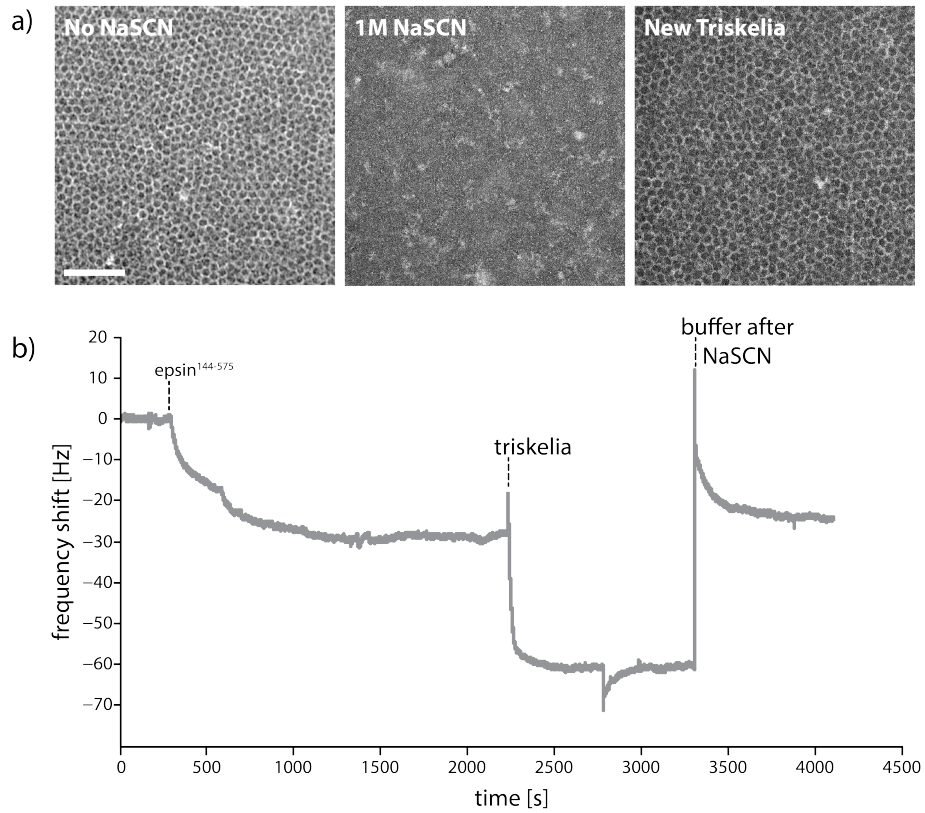
Figure 35: a) Electron micrographs of a clathrin lattice treated with NaSCN and reassembled with new triskelia, scale bar 200 nm [11]. b) SMR measurement of clathrin assembly and a subsequent disassembly with NaSCN. Obtained in the group of Dr. Thomas Burg, together with Dr. Yu Wang.
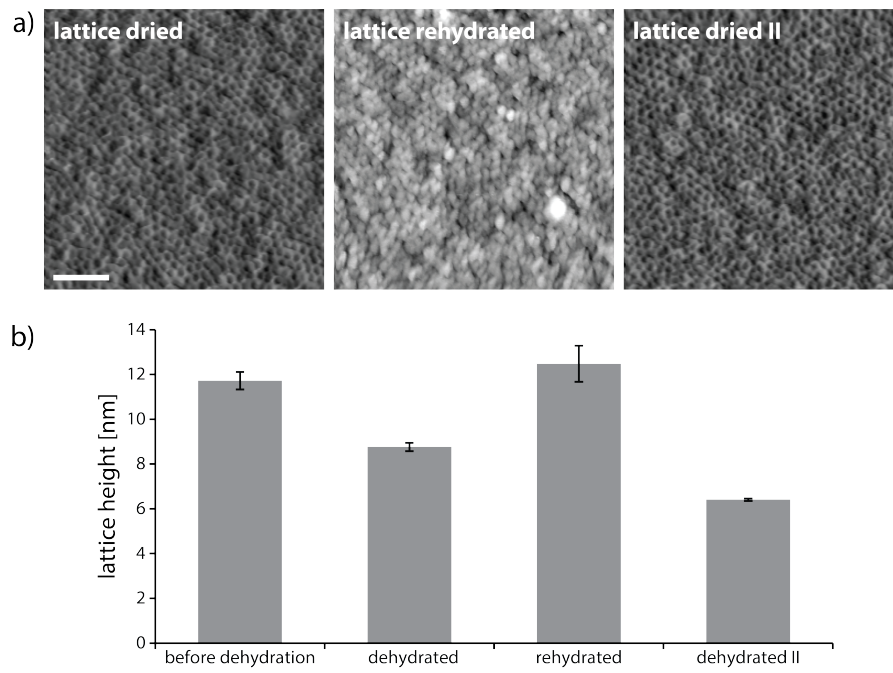
Figure 36: a) AFM images of uranyl acetate stabilized and dried lattices as well as a rehydrated lattice, scale bar 200 nm. b) Lattice height variations of a freshly prepared and hydrated lattice, stabilized and dried, then rehydrated again, and finally dried and stabilized for a second time [11].

3.4.1 *Native Stability of the Lattice*

Even without UA stabilization, the clathrin lattice has a tremendous stability itself. Forces above 10 nN are necessary to plastically deform the network (Fig. 37 a). Ap-
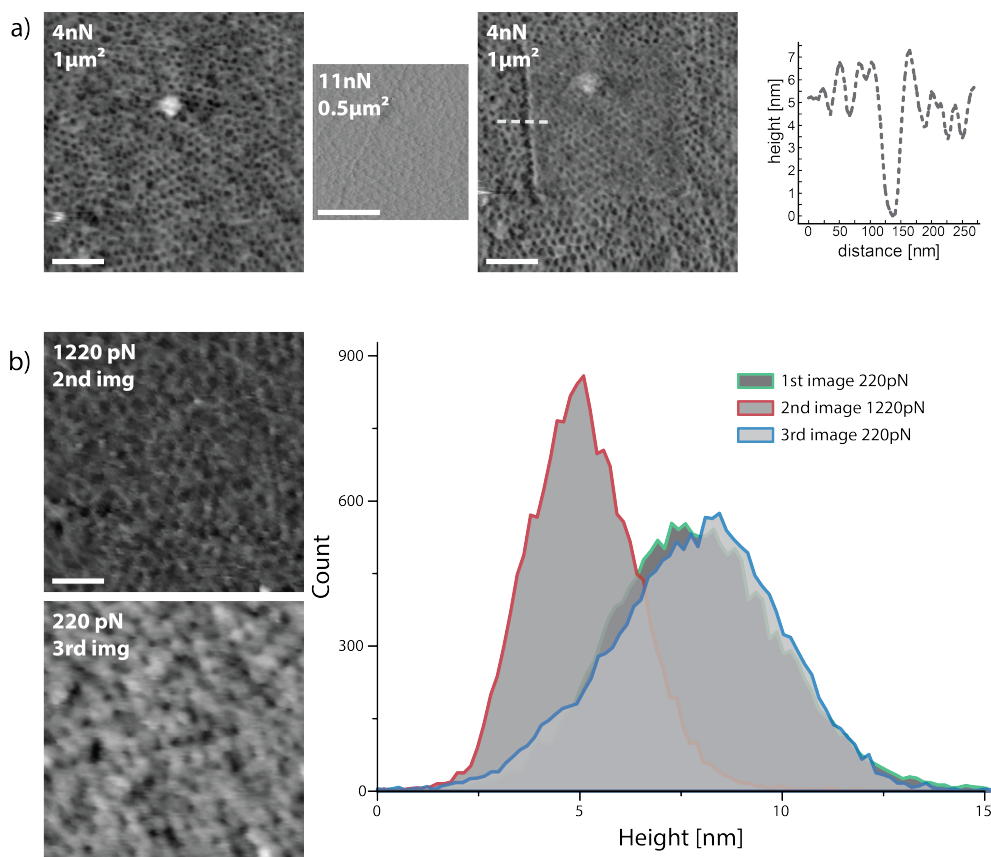
Figure 37: a) AFM images of a lattice which was partially scanned with high
destructive force (11 nN), scale bar 200 nm. b) Elastic recovery of
the lattice height after imaging with a moderate force of 1.2 nN,
scale bar 100 nm [10].

plying lower forces than that causes an elastic deformation and the clathrin lattice returns to its original height after removing the load (Fig. 37 b).

3.5 FUNCTIONALIZATION OF CLATHRIN LATTICES

In order to make efficient use of the clathrin lattice for practical applications, one goal was to investigate the functionalization of these networks with inorganic parti-

cles and active biomolecules.

3.5.1 *Inorganic Gold Nano-Particles*

Since the coverage of clathrin cages with gold nano-particles has already been shown [145, 146], the first logical approach was, to arrange colloidal gold particles on the clathrin lattice. For this purpose, gold particles were bound to the CLC via histidine residues. The binding of CLC to the gold particles is unspecific and, therefore, different CLC per particle ratios were tested to determine the most efficient ratio to cover CHC lattices (Fig. 38 & Fig. 39). An obvious drop in binding efficiency can be
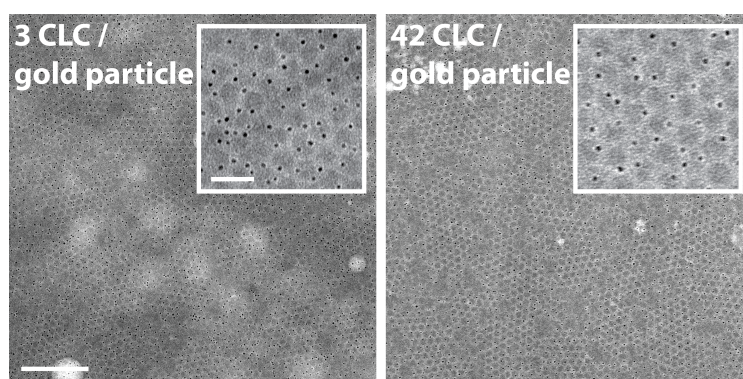
Figure 38: Electron micrographs of clathrin lattices functionalized with gold nano-particles, scale bar 300 nm (inlay 60 nm).

observed at higher ratios and the optimal ratio to cover the lattice with gold particles was found to be 3 CLC per particle (Fig. 39). At this ratio, 1525 gold particles bind per μm^2, which corresponds to a coverage of 0.4 particles per lattice rib. Assuming a coverage of two CLC per rib in the lattice [54, 167], this results in a decoration efficiency of around 20 %.

Furthermore, it is possible to cover the clathrin lattice with gold particles even after a dehydration and rehydration cycle. In this case, as expected, it is essential to stabilize the lattice with 5 % UA before dehydration.
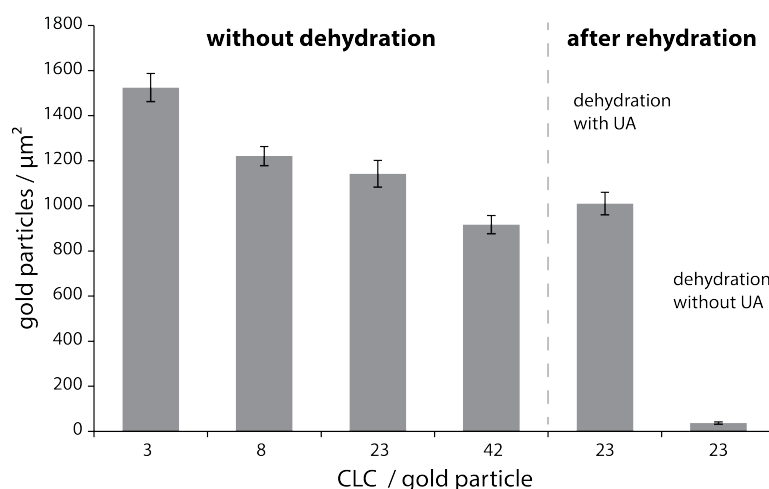
Figure 39: The number of gold particles per μm^2 lattice depends on the CLC to gold particle ratio. The CHC lattice can still be functionalized after stabilization and rehydration [11].

3.5.2 *Active Biomolecules (Auxilin's J-Domain)*

The final aim was to functionalize the clathrin lattice with active biomolecules. A self-destructive system was designed by P. Dannhauser in which auxilin's J-domain was crosslinked to the CLC via GST-GST (glutathione-S-transferase) heterodimerization (Fig. 40). Biologically, the J-domain's function is the recruitment and activation
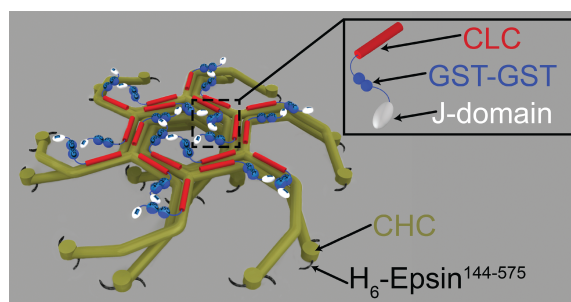
Figure 40: Model of a clathrin pore functionalized with auxilin's J-domains via GST-GST dimerization with CLC [11].

of Hsc70 protein, which disassembles the vesicle coats [82, 83]. Hence, after functionalization of the CHC-only lattice, with J-domain tagged CLC, the assembled network was able to self-destruct upon addition of Hsc70 and ATP (Fig. 41 a). The relative efficiency of the lattice disassembly was quantified by the peak height of
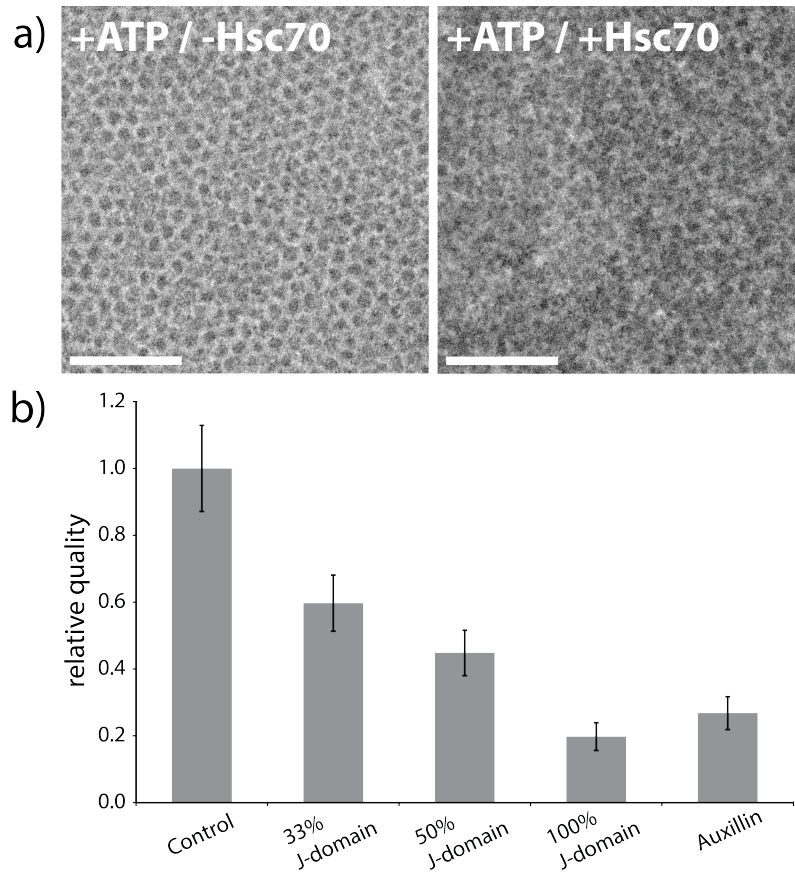
Figure 41: a) Electron micrographs of clathrin lattice disassembly via J-domian recruited and activated Hsc70, scale bar 200 nm. b) Quantification of Hsc70 activity based on the amount of J-domains immobilized on the clathrin lattice [11]. The control represents a 100 % modified lattice in absence of Hsc70.

the FFT's radial average (Fig. 41 b), as discussed before (quantification of assembly concentrations and kinetics, section 1.2). Here we could show that the efficiency indeed correlates with the amount of functionalized CLC used (percentage modified triskelia mixed with native triskelia). The effectiveness of the Hsc70 recruitment and activation is comparable, if not slightly higher, compared to the effectiveness of full auxilin in solution.

The remaining question of how many biomolecules bind to the CHC-only lattice via the modified CLC was addressed by SMR. In a first attempt, a CHC lattice was assembled inside the resonator and native CLC was added subsequently (Fig. 42). Preliminary results show that approximately 2900 CLC/μm^2 bind to 900 CHC triske-
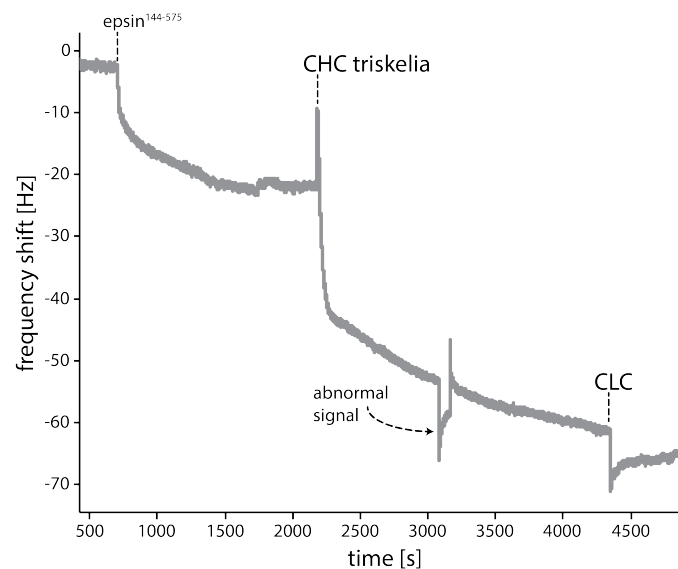
Figure 42: SMR experiment monitoring a CHC lattice assembly with subsequent addition of CLC. A small drop occurs when CLC are added which can be used to quantify how many CLC bind to the lattice (1.1 CLC / triskelion). Performed in the group of Dr. Thomas Burg, together with Dr. Yu Wang.

lia /μm^2 (3 CLC / triskelion).

Part IV

DISCUSSION

LATTICE ASSEMBLY

Since the early 1960s scientists extensively studied clathrin's structure and mechanisms of function [44, 46, 50]. The experimental research was mainly focusing on the icosahedral clathrin cage or its monomers, the triskelia [53]. Although a flat clathrin lattice on the inner plasma membrane of cells was discovered already in 1980 [59], it has not been further investigated, with exception for few theoretical studies [61, 94]. This work represents a first detailed study of flat clathrin lattices, including the investigation of its biological properties and explores its potential for the application in nanotechnological designs.

1.1 CLATHRIN ASSEMBLY CONCENTRATIONS AND KINETICS

In 2012 P. Dannhauser and E. Ungewickell showed that ENTH domain missing epsin ($H_6 - epsin^{144-575}$) can be used to form a flat clathrin lattice on liposomes [76] and extended this protocol to form flat lattices on negatively charged carbon-coated electron microscopy grids [10]. Using this artificial system, triskelion concentration dependencies and kinetics for the self-assembly of hexagonal clathrin lattices were studied in this work.

Fully formed lattices, using native (CHC + CLC) triskelia, could already be observed at a concentration of approximately 0.01 mg/ml, which is lower than the previously reported minimum concentration of 0.05 mg/ml for clathrin cage assembly [56]. With increasing triskelia concentrations only minor improvements in the clathrin lattice quality were observable. Fully formed lattices could also be observed using CHC-only triskelia at the same concentration (0.01 mg/ml). With increasing concentrations, however, the relative CHC-only lattice quality drops drastically. These findings support the well known inhibitory effect of the CLC in clathrin cage assembly under physiological conditions, which most probably allows the adaptor proteins to regulate the self-assembly process of clathrin [161, 166]. The rapid drop

in the quality of the CHC-only lattice might be due to triskelia aggregation, which has been known to occur in CLC lacking clathrin assemblies [170]. Therefore it was shown that proper organization between the triskelia inside the clathrin lattice is highly dependent on their bound CLC.

Both, the analysis of the EM time series images and the SMR measurements, show comparable kinetics. A time of approximately 10 min to 20 min is sufficient for the native clathrin lattice to assemble, whereas the CHC-only lattice requires slightly more time to do so (20 min to 30 min). This might seem counter-intuitive at first, keeping in mind the inhibitory effect of the CLC on clathrin assembly. The low concentration used to assemble the CHC-only lattices, however, as well as their overall lower assembly quality, might account for their slower assembly.

Furthermore, the SMR experiments monitoring the self-assembly of clathrin lattices suggest a two-step process for the formation of the lattice. The first hint towards this two-step process was the need for a double exponential function to fit the recorded data sufficiently during clathrin assembly (Fig. 26). Unfortunately, the necessity for a double exponential fit does not conclusively prove that the clathrin assembly is a two-step process because the same necessity can also be observed for the adsorption of $H_6 - epsin^{144-575}$. The insufficiency of a single exponential function to fit those curves might be due to a diffusion limited step. By considering the resonance frequency decay over time in the first seconds of the adhesion process, an adsorption time for single triskelia was estimated to be in the microseconds regime. Considering a diffusion coefficient of $9*10^{-8}$ cm^2/s for triskelia [171], a much longer diffusion time in the regime of tens of milliseconds was calculated for the 3 µm high SMR channel. The indicated diffusion limited adhesion process might explain the necessity for a double exponential fit to successfully follow the $H_6 - epsin^{144-575}$ and triskelia recordings in the SMR experiments.

Nonetheless, the high irregularity in the observed trend for the clathrin lattice assembly during the SMR experiments, compared to the $H_6 - epsin^{144-575}$ binding (Fig. 27), correlates well with the previously stated two-step process hypothesis. Namely, in a first step, the triskelia bind to the surface in a random manner, during a rather fast process (seconds regime). In a second phase, the triskelia start to organize themselves into the 2D lattice (Fig. 43 a). Thereby, certain triskelia can detach to assure a proper structure as well as further triskelia can be recruited, in order to fill in gaps. In contrast, a one-step process in which the triskelia immediately assemble into the flawless lattice is highly unlikely. This notion is further supported by the time series

of electron micrographs, which clearly shows random binding of triskelia during the first minute (Fig. 43 b). A two-step process, however, raises the question of how interchangeable or strong the binding between $H_6 - epsin^{144-575}$ and the triskelia is, in order to allow their reorganization. While the epsin binding motifs were studied extensively [172, 173], the actual binding affinity is still unknown. However, in this work it was observed that for a stable lattice in solution, either a fixation with glutaraldehyde was necessary, or an excess of triskelia in solution, allowing for constant triskelia exchange. This speaks for a rather interchangeable connection between $H_6 - epsin^{144-575}$ and the triskelia in the lattice.

In addition to the kinetics studies of clathrin lattice assembly, the SMR experiments
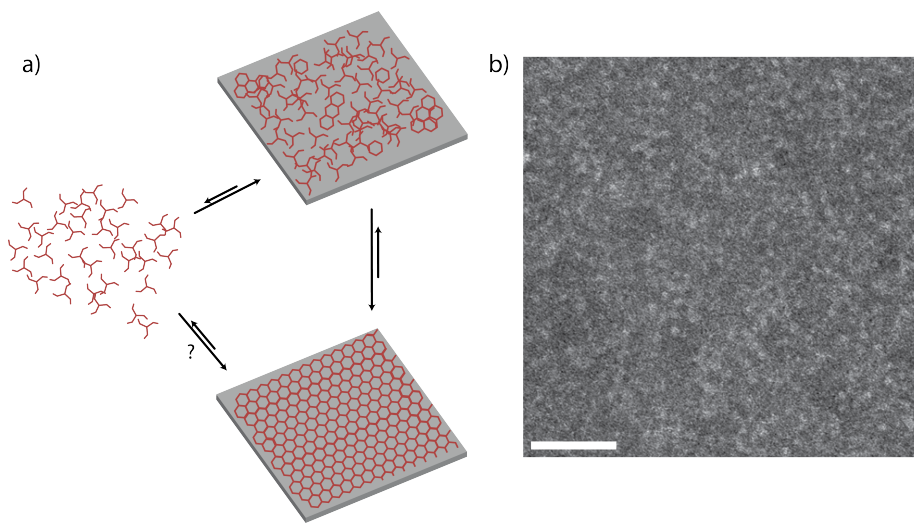
Figure 43: a) Hypothesis that triskelia are first randomly adsorbed to the surface and later reorient into a clathrin lattice. b) Electron micrograph of randomly bound triskelia after 1 min incubation, scale bar 200 nm.

allow for estimations of the number of molecules bound to the surface of the hollow cantilever. An average of 8800 adsorbed $H_6 - epsin^{144-575}$ molecules per μm^2 were calculated and only 760 native triskelia per μm^2 that bind to them. A higher number of $H_6 - epsin^{144-575}$ molecules compared to the number of triskelia is not surprising considering that the $H_6 - epsin^{144-575}$ fragment is only a peptide of 430 amino acids and, therefore, extremely small. The prediction that around 2500 native triskelia are needed to assemble a flawless lattice onto a surface of 1 μm^2, leads to the estimation that approximately 30 % of the cantilever's surface is covered with a clathrin lattice.

This ratio seems to be a fair estimation, considering fabrication defects or artifacts which might occur on the cantilever's surface, as well as remains from prior experiments, which could not be removed by cleaning with piranha-solution. Nonetheless, it might be of interest to improve the assembly-efficiency inside the resonators in near future.

CLATHRIN LATTICES FOR BIOLOGICAL STUDIES

2.1 VARIATIONS IN THE PUCKER ANGLE

To investigate the structure and properties of the clathrin lattice in more detail, multiple cropped images of AFM scans containing hexagonal pores were averaged. This averaging resulted in a highly featured image of the hexagonal pore (Fig. 29), later referred to as the "averaged pore". The topographical height image of this pore revealed a height of approximately 12 nm from the base to the vertices. Unsurprisingly, this diverges from the 24 nm height shown by Musacchio et al. [55] for triskelia in cages. The divergence is due to the fact that the legs of the triskelia need to bend inwards to form the cage and, furthermore, the degree of bending needs to change to scale the dimensions of the cage, which are dictated by the cargo size [174]. Two models exist which would allow this bending. One states that the pucker angle (Ψ), the angle between leg and vertex, is flexible. The second one relies on the variation of CHC contacts, which allow the change of the angle between the crossing legs of neighboring triskelia (Fig. 44) [54]. By analyzing structures of different-sized
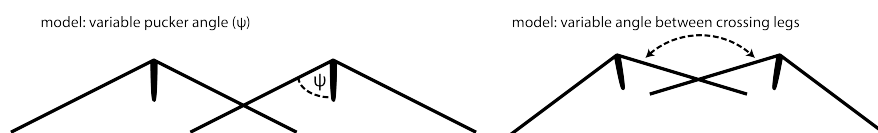
Figure 44: Two models allow the bending of triskelia to form the cage: 1) a variable angle between vertex and legs (Ψ), 2) a variable connection between the CHC, illustration based on [54].

clathrin cages, Fotin et al. showed a constant Ψ and suggested an invariable pucker angle [54]. Already five years before Fotin's work, Musacchio et al. proposed a fixed pucker angle for cage-forming triskelia and suggested the knees and distal legs to be the variable parts. Nonetheless, they assumed that in large cages and flat lattices the pucker angle might decrease [55]. The fact that the vertices are clearly visible features of the averaged pore structure enabled a detailed investigation of the pucker angle in flat clathrin lattices. By measuring Ψ in previously published structures,

obtained by cryo-electron microscopy and X-ray diffraction [54, 167], allowed to calculate the depth of the dent between two vertices (Fig. 30). For triskelia in solution and in average sized cages a Ψ of approximately 70° can be measured, which results in a dent of 3 nm. This is three times deeper than the depth measured in the averaged pore (1 nm), which correlates to a Ψ difference between cages and flat lattices of around 13°. This result shows that the pucker angle indeed provides a certain flexibility and, furthermore, suggests that the lattice might not be the most favorable state of the clathrin network, considering that Ψ is invariant in single triskelia and naturally-sized cages. This notion is supported by the findings of P. Dannhauser, who showed that clathrin self-assembles much faster and is more stable on 100 nm polystyrene beads, compared to the assembly on flat surfaces [10]. This indicates that a Ψ of 70° corresponds to the most stable structure conformation. The need for energy in order to change the angle would, therefore, explain a more unfavorable state. The fact that the clathrin lattice is more unstable as compared to the clathrin cage, additionally supports the hypothesis by Kirchhausen, that the lattice represents a triskelion reservoir. This reservoir disassembles on its edges and, therefore, induces a high local concentration of triskelia [62]. Furthermore, considering that variations in the pucker angle induce less stable assemblies, and Ψ might also change in very large clathrin cages [55], one might assume that this could be one of the reasons why clathrin cages are found only in a quite limited size range of 50 nm to 100 nm [50].

2.2 INFLUENCE OF CLATHRIN LIGHT CHAINS ON LATTICE MECHANICS

As mentioned briefly in the results section, the role and function of the CLC is still highly debated and of major interest in the clathrin field. It was shown that vesicle formation is still possible upon CLC depletion [168, 169], with the exception of the uptake of G-protein-coupled receptors, which was affected by the knockdown of CLC via siRNA [175]. Furthermore, Fotin et al. showed that the absence of CLC has no effect on the clathrin cage design and, therefore, suggested a more pronounced role of the CLC in the communication with cytoplasmic structures, based on the CLC location [54].

In this work we shed light onto the question whether CLC play a role in the mechanical properties of the flat clathrin lattices. This question was raised on one hand by the low-scanning force AFM images of CHC-only lattices, which seemed to show a

more flexible network, and on the other hand by various examples from the literature, which indicate a role of CLC in clathrin mechanics. For instance, by analyzing X-ray diffraction data from CLC mutants, Wilbur et al. have shown that CLC have an effect on the triskelion's knee. This effect in return might help in the regulation of clathrin cage assembly by facilitating conformational changes in the CHC [167]. Other studies state that CLC are involved in stabilizing the CHC trimerization [176, 177, 178] and it was shown that CLC ensure the proper structure of the triskelia themselves [170].

The studies in this work concerning native as well as CHC-only lattice mechanics on flat solid surfaces, revealed that the native lattice has a natural height of around 12 nm, which is comparable to the previously measured height from the averaged pore image. This height is rapidly reduced when load is applied onto the lattice, to a value of around 6 nm. In contrast, the height of the CHC-only lattice at low force is comparable to the native lattice height under heavy load, and is not further compressible. This finding supports the hypothesis that clathrin-bound CLC are involved in the overall mechanics of the lattice. A conceivable mechanism, which can explain the experimental outcome, would be that CLC stabilize the knees and hubs inside the clathrin array and, thereby, enable the lattice to "stay" on the terminal domains of its triskelia. Whereas, a not-stabilized CHC-only lattice collapses already in the absence of any load (Fig. 45).
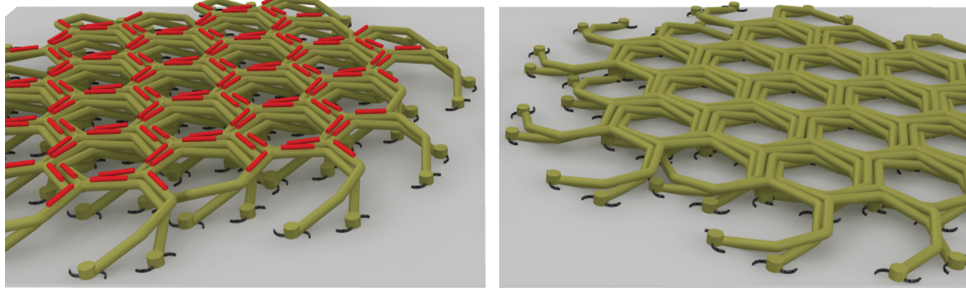
Figure 45: Left: CHC + CLC (red) lattice; right: CHC-only lattice. CLC have a stabilizing effect on clathrin lattices. A lack of CLC causes the lattice to collapse [10].

2.2.1 *Mechanics of Clathrin Cages*

Intrigued by these findings, P. Dannhauser & E. Ungewickell additionally showed that CLC-lacking clathrin is unable to form vesicles from more rigid liposome membranes at $15\,^{\circ}$C [10]. This is comparable to findings from 2012, where a similar mechanism was observed for Sec13-missing COPII vesicles [179]. To further investigate any changes in the clathrin cage mechanics by the lack of CLC, force curves of native cages as well as CHC-only cages were recorded. Unfortunately, the analysis of effective spring constants showed no indication for a different stability between the two types of cages. However, a bigger deviation between the extension and retraction curves in native clathrin cages as compared to CHC-only cages was detected (see Tab. 3 and Fig. 32). The observed deviation between extension and retraction was not related to a viscous effect, as the effective spring constants in the recordings for a single cage remained constant for different indentation speeds. Since the CLC are shown to have no obvious effect on the overall cage structure [54], the increased hysteresis between the curves observed for native clathrin cages might be due to the, above discussed, inhibitory effect of the CLC on cage assembly [161, 166]. Considering this inhibitory effect, one might expect a less strong association between native triskelia in the clathrin network. This in turn would suggest an easier reversible disruption of the connections, which in the end might account for the stronger deviations between extension and retraction curves during the investigations of the native clathrin cage mechanics.

CLATHRIN LATTICES FOR BIO-NANOTECHNOLOGY

3.1 CLATHRIN LATTICE FORMATION & POSSIBLE SUBSTRATES

In a first step, to show that the hexagonal clathrin lattice could be useful for nanotechnological applications, it was assembled on different substrates. Previously it had been shown that this lattice can be assembled on liposomes [76] and, as demonstrated in our biological studies, a lattice assembly on graphene and graphene covered electron microscopy grids was successful [10].

Additionally to the above mentioned materials, a successful clathrin lattice assembly on polyvinyl formal, aluminum, glass and silicon was observed. For this, a surface charge was the only requirement. Mica surfaces were the only exception that did not allow a proper assembly of the lattice and rather promoted the formation of vesicles. This might be due to a different binding behavior of the $H_6 - epsin^{144-575}$ to the naturally charged mica surface, similar to the different orientations of fibrinogen when bound to graphite and mica, as shown in simulations by S. Köhler [180]. Therefore, future simulations of the binding behavior of unstructured $H_6 - epsin^{144-575}$ to different surface materials might provide further insights.

3.1.1 *Assembly on Curved Surfaces*

It seems trivial that clathrin lattices prefer to form on convex surfaces, since they represent the native bending direction of the cages. In fact it was shown that the the assembly of clathrin lattices on polystyrene beads was faster than the assembly on flat surfaces and, furthermore, more stable [10]. In addition, native lattices are able to self-assemble even on concave curved substrates, such as small valleys in electron microscopy grids (Fig. 34). Interestingly, the formation on concave areas was more challenging for CHC-only lattices, resulting in a lack of CHC-only lattice on areas with a radius of curvature of approximately 400 nm. This difficulty in lattice assembly on concave surfaces is probably due to the lack of stabilization by the CLC, as discussed above. The curvature dependency should be kept in mind when the

lattice is assembled for usage on a concave structures, such as tubing, and a prior functionalization with CLC might be required in such cases.

3.2 CLATHRIN LATTICE DISASSEMBLY

For dynamic applications, disassembling the clathrin lattice without destroying the underlying layer of $H_6 - \text{epsin}^{144-575}$ is necessary, in order to allow fast functional recovery. Nandi & Edelhoch have shown in 1984 that the chaotropic salt NaSCN is efficient in low concentration to impede the cage structure [181]. Already at very low concentrations (0.05 M) and short incubation times (5 s) a certain rearrangement in the overall lattice structure could be observed (data not shown) [11]. An increase in the concentration (1 M) and longer incubation times allowed for a complete removal of the clathrin network. Conveniently, the adhered $H_6 - \text{epsin}^{144-575}$is able to withstand the NaSCN treatment and, therefore, a simple washing step and addition of fresh triskelia was enough to assemble a new lattice.

The complete removal of the clathrin lattice by NaSCN could also be shown via SMR experiments. However, in this case a reassembly of the lattice inside the SMR channel after NaSCN treatment was not achieved. A closer look at the baseline after NaSCN treatment (Fig. 35 b) shows a slightly increased frequency compared to the $H_6 - \text{epsin}^{144-575}$ baseline. This might indicate that the incubation with NaSCN could have removed a certain amount of $H_6 - \text{epsin}^{144-575}$. On one hand, this might be due to the fact that treatments in microfluidic systems are in general more efficient than in batch processes because of their reaction limited rather than diffusion limited nature [182]. If so, the problem of $H_6 - \text{epsin}^{144-575}$-removal might be solved by using a lower concentration of NaSCN. On the other hand, the incubation times of the NaSCN treatment in the SMR were too long and, therefore, shorter incubation times additionally to lower concentrations need to be tested.

3.3 CLATHRIN LATTICE STABILITY & STABILIZATION

Clathrin lattices, when not fixed, have a lifetime in the order of tens of minutes. To extend this time, the lattices can be treated with glutaraldehyde, which prevents disassociation of the triskelia and enables usage of the lattice for biological studies [10]. For rather harsh nanotechnological applications, such as filters, as well as for storage purposes, it would be beneficial to further stabilize the clathrin lattice and, addition-

ally, allow for rehydration without destroying the overall structural properties and its biological function. Both of these issues were addressed in this work. Regarding the stability issue, the lattice was found to be highly stabilized by using 5 % of the heavy metal uranyl acetate (UA), a substance well known for negative staining in electron microscopy [183]. Only a minor drop in the lattice height was observed, when dehydrated after UA fixation. After rehydration with an acetate free buffer, the lattice height was fully recovered. This suggests the stabilization of the clathrin array with UA does not affect the overall structure of the lattice. The successful binding of CLC onto the rehydrated lattice (discussed below, section 3.4.1) also supports this notion and, furthermore, demonstrates that even the biological activity is restored. However, when the lattice is treated with 5 % UA for a second time, the dehydrated lattice shows a reduction of 50 % compared to its original height. This suggests that successive fixation might affect the interaction between the triskelia, weakens the CHC peptides or disrupts proper interaction between CLC and CHC, which results in a lattice collapse [10]. Therefore, depending on the application's need for lattice rigidity, the reassembly of a new lattice, using NaSCN, might be a good strategy after the first fixation. Nonetheless, a successful first stabilization and rehydration renders the strategy of UA fixation very useful. Considering that an intact dehydrated lattice was observed even after several months, makes UA fixation invaluable for long time storage. We could also imagine that the fixation with uranyl acetate might help to stabilize a variety of proteins for other nanotechnological applications.

Regarding the natural stability of the clathrin lattice, it was shown that at moderate loads (here up to 1 nN) the lattice deforms elastically and returns to its original height after the load is removed (Fig. 37 b). To plastically deform the lattice without UA treatment, a load of around 10 nN is needed. These high forces result in only a minor drop in the lattice height compared to a collapsed lattice, but the overall structure is damaged (Fig. 37 a). This finding shows that the lattice is an extremely stable structure compared to other biological samples. For example, it has been shown that microtubules can only withstand force of up to 0.3 nN to 0.5 nN [184, 185]. The force that the flat lattice can withstand exceeds even the breaking forces of virus capsids (3 nN to 6 nN for Φ29 and adenoviruses) [186, 187]. However, it is difficult to directly compare the mechanics of flat clathrin lattices with hollow structures, such as microtubules and viruses. Unfortunately, there is not much information on the rupture force of other flat protein networks in the literature. A rupture force in

the same regime can be observed for 1,2-Dimyristoyl-sn-glycero-3-phosphocholine (DMPC) lipid bilayers, namely 4 nN to 15 nN, depending on the salt conditions [188]. Additionally, it was shown that S-layers withstand loads of at least 2 nN [189], but most likely this force is far below their breaking points.

3.4 CLATHRIN LATTICE FUNCTIONALIZATION

Finally, the possibilities and the efficiency of the clathrin lattice functionalization with inorganic particles and active biomolecules was investigated. Modifications of the lattice would not only allow to tune the array for a certain purpose but, furthermore, they might in certain cases enhance the enzymatic activity since the exact spacing of individual enzymes on the lattice, might reduce spatial hindrance. Since it is possible to purify CHC and CLC separately, and to later reattach the CLC onto the clathrin network, this seemed to be a good strategy to take advantage of for clathrin lattice functionalization.

3.4.1 *Functionalization with Gold Particles*

The immobilization of colloidal nano-gold particles on clathrin cages has already been established [145, 146] and, therefore, the first approach was to couple gold-particles to the lattice. For this purpose, histidine-tagged CLC in various concentrations were incubated together with gold particles, which resulted in different ratios of CLC per particle. These "gold CLC" were subsequently attached to CHC lattices. Here, a most efficient binding was observed when the CLC concentration was low and, statistically, only three CLC were bound to one gold particle (fig. 39). This leads to the assumption that binding of more CLC per particle might hinder the attachment of other beads, since one bead would then occupy multiple adjacent CLC binding sites at once. At maximum coverage, a decoration efficiency of around 0.4 beads per lattice rib (1525 particles per μm^2) was estimated. This decoration density is certainly not inefficient, however, assuming theoretically one or two CLC per lattice rib [54, 167], improvements might be possible. To increase the efficiency one might envision a strategy which would enable to couple only a single CLC to a single particle.

The approach of gold particle immobilization was also used to show that after re-hydration of UA-fixed lattices, not only its structure but also the biological activity is restored, as discussed above. Binding of CLC-coupled particles to the rehydrated lattice revealed a comparable efficiency to the one of the constantly hydrated lattice. In contrast, a dried and rehydrated lattice without UA fixation, showed almost no CLC binding. Combined with our structural analysis, this confirms the utility of the UA-fixation approach for storage purposes.

3.4.2 *Functionalization with Auxilin's J-Domain*

In order to examine the possibility of modifying the clathrin lattice with bioactive molecules, auxilin's J-domain was used. As discussed in the introduction, the J-domain plays an essential part in the disassembly of clathrin cages in vivo, by re-cruiting and activating the uncoating ATPase Hsc70 [82, 83]. Unlike for the gold particles, here a specific approach was used to link a single J-domain to a single CLC by GST-GST heterodimerization [164].

The quantification of the lattice disassembly efficiency for different ratios of J-domain coupled CLC and native CLC (33 %, 50 % and 100 % J-domain coupled CLC) shows a clear dependency on the amount of immobilized J-domains (Fig. 41). Interestingly, the efficiency of the disassembly with immobilized J-domains might be even slightly higher compared to the efficiency of full auxilin in solution. This phenomenon might indicate a slight hindrance for the whole auxilin molecule to bind to the lattice, when it is attached to a solid surface.

The disassembly of the clathrin lattice via the immobilized J-domain & Hsc70 system shows a simple strategy for functionalization. However, a crucial remaining ques-tion is the decoration efficiency of this approach, since the small J-domain cannot be easily visualized. From preliminary SMR data a binding efficiency of approxi-mately 3 native CLC per triskelion was calculated. Although more data needs to be acquired in order to confirm this result, the preliminary calculations suggest a full coverage of the CHC-lattice by CLC. In addition to the necessity for better statistics in this regard, it also must be shown that these numbers hold for the modified CLC, which will be examined in near future.

Part V

CONCLUSIONS & OUTLOOK

CONCLUSIONS & OUTLOOK

The goal of this project was to use AFM to expand the knowledge concerning the self-assembling protein network named clathrin. While clathrin was so far almost exclusively studied using its cage structure, this thesis investigates in details 2D clathrin lattices and describes methods how to study these lattices using atomic force microscopy.

The clathrin lattices represent a tremendous asset to biological researchers studying the clathrin structure and functionality. Here the clathrin lattice was used to study the triskelion orientation inside the hexagonal pores by averaging low force AFM images. These averaged images provided insight into the variability of the pucker angle in flat clathrin arrays, the angle between triskelion hub and leg, when compared to the pucker angle inside cages or triskelia in solution. In addition this strengthens the suggestion that the pucker angle also differs in very large clathrin cages ($\gg 100\,\text{nm}$ in diameter). In the future this might be investigated by assembling clathrin onto mica surfaces, which were shown to drive huge ($> 200\,\text{nm}$), vesicle-like assemblies (Fig. 33).

Furthermore, the clathrin lattice was used to study the role of clathrin light chains. Investigation of the lattice quality when assembled with different triskelia concentrations supported the assumption that CLC inhibit cage formation and, therefore, unspecific accumulation. Additionally, the role of CLC in clathrin lattice mechanics was studied by probing the lattice's compressibility using AFM. It could be shown that CLC play an important role in stabilizing the lattice, and preventing its collapse. This suggests that clathrin without CLC is unable to form vesicles if the membrane rigidity is increased. These approaches can be used in future experiments to further extend the knowledge about the CLC. For instance, in analogous experiments, it could be investigated whether the C- or N- terminal part of the CLC has a more important role in the stabilization process, by using mutated CLC. In other experiments one could imagine to gain further insight in the debate whether the clathrin lattices themselves are able to form cages and bud vesicles. These investigations might be possible by assembling the clathrin lattice onto soft gels.

The clathrin lattice is not only a new and exciting way to study biological mechanisms but it also shows tremendous potential for the field of bionanotechnology. In order to introduce the clathrin lattice to this field of research, the clathrin lattice properties and the possibilities for its modification were thoroughly investigated. It was found that it is possible to assemble this unique protein network on various surface materials, as well as to easily disassemble and reassemble the lattice and, furthermore, the lattice can be dried and rehydrated, without losing its structure and functionality. All these properties make the clathrin lattice a very interesting building block and matrix for research and industrial nanotechnology designs alike. The possibility for disassembly enables its usage in versatile and dynamic applications, while the possibility for dehydration & rehydration enables longtime storage and even uncomplicated shipment. Another key feature of the clathrin lattice is the shown potential to functionalize the lattice with inorganic materials and active biomolecules. This renders the lattice to a versatile matrix, which can be specifically tailored to the needs of a nanotechnological design. The functionalization can be easily performed using protocols to attach the CLC, either specifically or unspecifically, to the desired particle or molecule. However, the efficiency of the lattice decoration with biomolecules, and whether it depends on the size of the molecule, is one of the important characterizations that are still missing, and should be addressed in the near future. The ratios between triskelia and the attached modified light chains can most likely be accessed via suspended microresonator experiments. Furthermore, the question whether the binding of biomolecules to the clathrin lattice influences their lifetime remains. This question could be addressed by immobilizing enzymes that catalyze reactions which allow easy monitoring (e.g. β-galactosidase). In this way, the efficiency of catalysis and the lifetime of immobilized enzymes can be directly compared to enzymes in solution.

For future applications, the clathrin lattice could enable designs which provide a strategy to immobilize molecules in a specific sequence (e.g. for enzyme cascades). These systems would allow a more effective catalysis by efficiently passing the reaction product from one enzyme to the next one in line.
Another application could be the parallel screening of immobilized biomolecules when exposed to different conditions via a microfluidic system with various inlets (Fig. 46). This setup would allow to efficiently investigate the influence of variable buffer conditions, ATP concentrations, and different cofactors, on the properties of
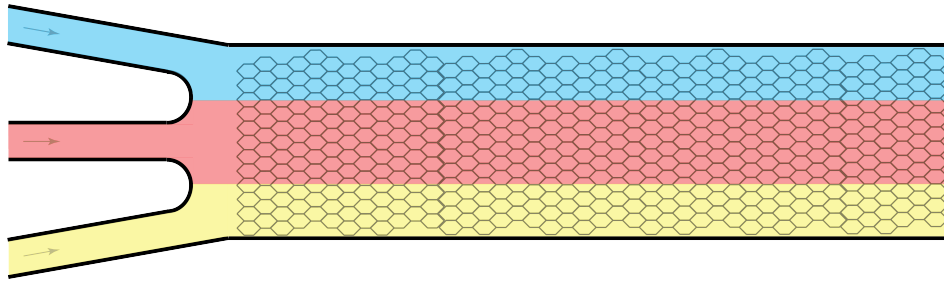
Figure 46: Schematic of a microfluidic system with an assembled clathrin lattice inside the channel. A design comparable to this might allow parallel screening of immobilized biomolecules exposed to different conditions.

biomolecules. For instance, it could be used to investigate biomolecule-dynamics. By labeling the dynamic parts of the active molecule with FRET pairs, a constant monitoring of the FRET intensity might provide insights into inhibitory or activating conditions.

REFERENCES

[1] J. Mou, D. M. Czajkowsky, Y. Zhang, and Z. Shao, "High-resolution atomic-force microscopy of dna: the pitch of the double helix," *{FEBS} Letters*, vol. 371, no. 3, pp. 279 – 282, 1995.

[2] S. Yamamoto, F. Nakamura, J. Hitomi, M. Shigeno, S. Sawaguchi, H. Abe, and T. Ushiki, "Atomic force microscopy of intact and digested collagen molecules," *Journal of Electron Microscopy*, vol. 49, no. 3, pp. 423–427, 2000.

[3] C. M. Kacher, I. M. Weiss, R. J. Stewart, C. F. Schmidt, P. K. Hansma, M. Radmacher, and M. Fritz, "Imaging microtubules and kinesin decorated microtubules using tapping mode atomic force microscopy in fluids," *European Biophysics Journal*, vol. 28, no. 8, pp. 611–620, 2000.

[4] E. Henderson, P. Haydon, and D. Sakaguchi, "Actin filament dynamics in living glial cells imaged by atomic force microscopy," *Science*, vol. 257, no. 5078, pp. 1944–1946, 1992.

[5] C. A. J. Putman, K. O. Van der Werf, B. G. De Grooth, N. F. Van Hulst, and J. Greve, "Tapping mode atomic force microscopy in liquid," *Applied Physics Letters*, vol. 64, no. 18, pp. 2454–2456, 1994.

[6] G. Binnig, C. Gerber, E. Stoll, T. R. Albrecht, and C. F. Quate, "Atomic resolution with atomic force microscope," *EPL (Europhysics Letters)*, vol. 3, no. 12, p. 1281, 1987.

[7] T. R. Albrecht and C. F. Quate, "Atomic resolution with the atomic force microscope on conductors and nonconductors," *Journal of Vacuum Science & Technology A*, vol. 6, no. 2, pp. 271–274, 1988.

[8] T. P. Weihs, Z. Nawaz, S. P. Jarvis, and J. B. Pethica, "Limits of imaging resolution for atomic force microscopy of molecules," *Applied Physics Letters*, vol. 59, no. 27, pp. 3536–3538, 1991.

[9] A. L. Weisenhorn, M. Khorsandi, S. Kasas, V. Gotzos, and H. J. Butt, "Deformation and height anomaly of soft surfaces studied with an afm," *Nanotechnology*, vol. 4, no. 2, p. 106, 1993.

[10] P. N. Dannhauser, M. Platen, H. Boning, H. Ungewickell, I. A. Schaap, and E. J. Ungewickell, "Effect of clathrin light chains on the stiffness of clathrin lattices and membrane budding," *Traffic*, vol. 16, pp. 519–533, May 2015.

[11] P. N. Dannhauser, M. Platen, H. Böhning, and I. A. T. Schaap, "Durable protein lattices of clathrin that can be functionalised with nano-particles and active biomolecules," *Nature Nanotechnology*, 2015.

[12] G. Binnig, C. F. Quate, and C. Gerber, "Atomic force microscope," *Phys. Rev. Lett.*, vol. 56, pp. 930–933, Mar 1986.

[13] N. A. Burnham, O. P. Behrend, F. Oulevey, G. Gremaud, P.-J. Gallo, D. Gourdon, E. Dupas, A. J. Kulik, H. M. Pollock, and G. A. D. Briggs, "How does a tip tap?," *Nanotechnology*, vol. 8, no. 2, p. 67, 1997.

[14] N. Jalili and K. Laxminarayana, "A review of atomic force microscopy imaging systems: application to molecular metrology and biological sciences," *Mechatronics*, vol. 14, no. 8, pp. 907 – 945, 2004.

[15] D. Walters, J. Cleveland, N. Thomson, P. Hansma, M. Wendman, G. Gurley, and V. Elings, "Short cantilevers for atomic force microscopy," *Review of Scientific Instruments*, vol. 67, no. 10, pp. 3583–3590, 1996.

[16] D. Sarid, *Scanning force microscopy*. Oxford University Press, 1991.

[17] P. J. de Pablo, J. Colchero, J. Gómez-Herrero, and A. M. Baró, "Jumping mode scanning force microscopy," *Applied Physics Letters*, vol. 73, no. 22, pp. 3300–3302, 1998.

[18] D. Martinez-Martin, C. Carrasco, M. Hernando-Perez, P. J. de Pablo, J. Gomez-Herrero, R. Perez, M. G. Mateu, J. L. Carrascosa, D. Kiracofe, J. Melcher, and A. Raman, "Resolving structure and mechanical properties at the nanoscale of viruses with frequency modulation atomic force microscopy," *PLoS ONE*, vol. 7, p. e30204, 01 2012.

[19] Q. Zhong, D. Inniss, K. Kjoller, and V. Elings, "Fractured polymer/silica fiber surface studied by tapping mode atomic force microscopy," *Surface Science Letters*, vol. 290, no. 1–2, pp. L688 – L692, 1993.

[20] A. Rosa-Zeiser, E. Weilandt, S. Hild, and O. Marti, "The simultaneous measurement of elastic, electrostatic and adhesive properties by scanning force microscopy: pulsed-force mode operation," *Measurement Science and Technology*, vol. 8, no. 11, p. 1333, 1997.

[21] Z. Bálint, I. A. Krizbai, I. Wilhelm, A. E. Farkas, A. Párducz, Z. Szegletes, and G. Váró, "Changes induced by hyperosmotic mannitol in cerebral endothelial cells: an atomic force microscopic study," *European Biophysics Journal*, vol. 36, no. 2, pp. 113–120, 2007.

[22] L. Wildling, C. Rankl, T. Haselgrubler, H. J. Gruber, M. Holy, A. H. Newman, M. F. Zou, R. Zhu, M. Freissmuth, H. H. Sitte, and P. Hinterdorfer, "Probing binding pocket of serotonin transporter by single molecular force spectroscopy on living cells," *J. Biol. Chem.*, vol. 287, pp. 105–113, Jan 2012.

[23] D. J. Müller, H. Janovjak, T. Lehto, L. Kuerschner, and K. Anderson, "Observing structure, function and assembly of single proteins by {AFM}," *Progress in Biophysics and Molecular Biology*, vol. 79, no. 1–3, pp. 1 – 43, 2002.

[24] A. Ortega-Esteban, I. Horcas, M. Hernando-Pérez, P. Ares, A. Pérez-Berná, C. S. Martín, J. Carrascosa, P. de Pablo, and J. Gómez-Herrero, "Minimizing tip–sample forces in jumping mode atomic force microscopy in liquid," *Ultramicroscopy*, vol. 114, no. 0, pp. 56 – 61, 2012.

[25] T. Sulchek, R. Hsieh, J. D. Adams, S. C. Minne, C. F. Quate, and D. M. Adderton, "High-speed atomic force microscopy in liquid," *Review of Scientific Instruments*, vol. 71, no. 5, pp. 2097–2099, 2000.

[26] J. Tamayo, A. Humphris, R. Owen, and M. Miles, "High-q dynamic force microscopy in liquid and its application to living cells," *Biophysical Journal*, vol. 81, no. 1, pp. 526 – 537, 2001.

[27] P. K. Hansma, J. P. Cleveland, M. Radmacher, D. A. Walters, P. E. Hillner, M. Bezanilla, M. Fritz, D. Vie, H. G. Hansma, C. B. Prater, J. Massie, L. Fukunaga, J. Gurley, and V. Elings, "Tapping mode atomic force microscopy in liquids," *Applied Physics Letters*, vol. 64, no. 13, pp. 1738–1740, 1994.

[28] T. E. Schäffer, J. P. Cleveland, F. Ohnesorge, D. A. Walters, and P. K. Hansma, "Studies of vibrating atomic force microscope cantilevers in liquid," *Journal of Applied Physics*, vol. 80, no. 7, pp. 3622–3627, 1996.

[29] C. Carrasco, P. Ares, P. J. de Pablo, and J. Gómez-Herrero, "Cutting down the forest of peaks in acoustic dynamic atomic force microscopy in liquid," *Review of Scientific Instruments*, vol. 79, no. 12, pp. –, 2008.

[30] A. Maali, C. Hurth, R. Boisgard, C. Jai, T. Cohen-Bouhacina, and J.-P. Aimé, "Hydrodynamics of oscillating atomic force microscopy cantilevers in viscous fluids," *Journal of Applied Physics*, vol. 97, no. 7, pp. –, 2005.

[31] M. Radmacher, "Measuring the elastic properties of biological samples with the afm," *Engineering in Medicine and Biology Magazine, IEEE*, vol. 16, pp. 47–57, Mar 1997.

[32] A. L. Weisenhorn, P. Maivald, H.-J. Butt, and P. K. Hansma, "Measuring adhesion, attraction, and repulsion between surfaces in liquids with an atomic-force microscope," *Phys. Rev. B*, vol. 45, pp. 11226–11232, May 1992.

[33] J. Zlatanova, S. M. Lindsay, and S. H. Leuba, "Single molecule force spectroscopy in biology using the atomic force microscope," *Progress in Biophysics and Molecular Biology*, vol. 74, no. 1–2, pp. 37 – 61, 2000. Single Molecule Biochemistry and Molecular Biology.

[34] N. A. Burnham, R. J. Colton, and H. M. Pollock, "Interpretation of force curves in force microscopy," *Nanotechnology*, vol. 4, no. 2, p. 64, 1993.

[35] J. Domke and M. Radmacher, "Measuring the elastic properties of thin polymer films with the atomic force microscope," *Langmuir*, vol. 14, no. 12, pp. 3320–3325, 1998.

[36] R. Feynman, *The Feynman Lectures on Physics, Vol. II*, ch. 38, pp. 38–1–38–2. Basic Books, 50th anniverary ed. ed., 2011.

[37] H. Hertz, "Ueber die Berührung fester elastischer Körper.," *Journal für die reine und angewandte Mathematik*, vol. 1882, no. 92, pp. 156–171, 1882.

[38] B. Alberts, D. Bray, J. Lewis, M. Raff, K. Roberts, and J. D. Watson, *Molecular Biology of The Cell*, pp. 599–600. Garland Publishing, 3rd ed., 1994.

[39] S. Mayor and R. E. Pagano, "Pathways of clathrin-independent endocytosis," *Nat. Rev. Mol. Cell Biol.*, vol. 8, pp. 603–612, Aug 2007.

[40] K. Sandvig, S. Pust, T. Skotland, and B. van Deurs, "Clathrin-independent endocytosis: mechanisms and function," *Current Opinion in Cell Biology*, vol. 23, no. 4, pp. 413 – 420, 2011. Membranes and organelles.

[41] J. Gruenberg and K. E. Howell, "Membrane traffic in endocytosis: insights from cell-free assays," *Annu. Rev. Cell Biol.*, vol. 5, pp. 453–481, 1989.

[42] J. M. Larkin, W. C. Donzell, and R. G. Anderson, "Potassium-dependent assembly of coated pits: new coated pits form as planar clathrin lattices," *J. Cell Biol.*, vol. 103, pp. 2619–2627, Dec 1986.

[43] B. M. Pearse, "Clathrin and coated vesicles," *EMBO J.*, vol. 6, pp. 2507–2512, Sep 1987.

[44] B. M. Pearse, "Coated vesicles from pig brain: purification and biochemical characterization," *J. Mol. Biol.*, vol. 97, pp. 93–98, Sep 1975.

[45] B. M. Pearse, "Clathrin: a unique protein associated with intracellular transfer of membrane by coated vesicles," *Proc. Natl. Acad. Sci. U.S.A.*, vol. 73, pp. 1255–1259, Apr 1976.

[46] T. F. ROTH and K. R. PORTER, "Specialized sites on the cell surface for protein uptake," *In Electron Microscopy: Fifth International Congress for Electron Microscopy in Philadelphia*, p. 2:LL4, 1962.

[47] T. F. ROTH and K. R. PORTER, "Membrane differentiation for protein uptake," *Fed. Proc.*, vol. 22, no. 2, 1963.

[48] T. F. ROTH and K. R. PORTER, "YOLK PROTEIN UPTAKE IN THE OOCYTE OF THE MOSQUITO AEDES AEGYPTI. L," *J. Cell Biol.*, vol. 20, pp. 313–332, Feb 1964.

[49] B. Bowers, "Coated vesicles in the pericardial cells of the aphid (myzus persicae sulz)," *Protoplasma*, vol. 59, no. 2, pp. 351–367, 1964.

[50] T. Kanaseki and K. Kadota, "The "vesicle in a basket". A morphological study of the coated vesicle isolated from the nerve endings of the guinea pig brain,

with special reference to the mechanism of membrane movements," *J. Cell Biol.*, vol. 42, pp. 202–220, Jul 1969.

[51] R. Crowther, J. Pinch, and B. Pearse, "On the structure of coated vesicles," *Journal of Molecular Biology*, vol. 103, no. 4, pp. 785 – 798, 1976.

[52] E. Ungewickell and D. Branton, "Assembly units of clathrin coats," *Nature*, vol. 289, pp. 420–422, Jan 1981.

[53] F. M. Brodsky, "Diversity of clathrin function: new tricks for an old protein," *Annu. Rev. Cell Dev. Biol.*, vol. 28, pp. 309–336, 2012.

[54] A. Fotin, Y. Cheng, P. Sliz, N. Grigorieff, S. C. Harrison, T. Kirchhausen, and T. Walz, "Molecular model for a complete clathrin lattice from electron cryomicroscopy," *Nature*, vol. 432, pp. 573–579, Dec 2004.

[55] A. Musacchio, C. J. Smith, A. M. Roseman, S. C. Harrison, T. Kirchhausen, and B. M. Pearse, "Functional organization of clathrin in coats: combining electron cryomicroscopy and X-ray crystallography," *Mol. Cell*, vol. 3, pp. 761–770, Jun 1999.

[56] R. A. Crowther and B. M. Pearse, "Assembly and packing of clathrin into coats," *J. Cell Biol.*, vol. 91, pp. 790–797, Dec 1981.

[57] T. Kirchhausen, S. C. Harrison, and J. Heuser, "Configuration of clathrin trimers: evidence from electron microscopy," *J. Ultrastruct. Mol. Struct. Res.*, vol. 94, pp. 199–208, Mar 1986.

[58] C.-Y. Chen, M. L. Reese, P. K. Hwang, N. Ota, D. Agard, and F. M. Brodsky, "Clathrin light and heavy chain interface: α-helix binding superhelix loops via critical tryptophans," *The EMBO Journal*, vol. 21, no. 22, pp. 6072–6082, 2002.

[59] J. Heuser, "Three-dimensional visualization of coated vesicle formation in fibroblasts," *J. Cell Biol.*, vol. 84, pp. 560–583, Mar 1980.

[60] T. Kirchhausen, "Coated pits and coated vesicles — sorting it all out," *Current Opinion in Structural Biology*, vol. 3, no. 2, pp. 182 – 188, 1993.

[61] R. Nossal, "Energetics of clathrin basket assembly," *Traffic*, vol. 2, no. 2, pp. 138–147, 2001.

[62] T. Kirchhausen, "Clathrin," *Annu. Rev. Biochem.*, vol. 69, pp. 699–727, 2000.

[63] J. Hirst and M. S. Robinson, "Clathrin and adaptors," *Biochimica et Biophysica Acta (BBA) - Molecular Cell Research*, vol. 1404, no. 1–2, pp. 173 – 193, 1998.

[64] M. S. Robinson and B. M. Pearse, "Immunofluorescent localization of 100K coated vesicle proteins," *J. Cell Biol.*, vol. 102, pp. 48–54, Jan 1986.

[65] S. Ahle, A. Mann, U. Eichelsbacher, and E. Ungewickell, "Structural relationships between clathrin assembly proteins from the Golgi and the plasma membrane," *EMBO J.*, vol. 7, pp. 919–929, Apr 1988.

[66] K. M. Huang, K. D'Hondt, H. Riezman, and S. K. Lemmon, "Clathrin functions in the absence of heterotetrameric adaptors and AP180-related proteins in yeast," *EMBO J.*, vol. 18, pp. 3897–3908, Jul 1999.

[67] M. G. Ford, B. M. Pearse, M. K. Higgins, Y. Vallis, D. J. Owen, A. Gibson, C. R. Hopkins, P. R. Evans, and H. T. McMahon, "Simultaneous binding of PtdIns(4,5)P2 and clathrin by AP180 in the nucleation of clathrin lattices on membranes," *Science*, vol. 291, pp. 1051–1055, Feb 2001.

[68] S. A. Morris, S. Schroder, U. Plessmann, K. Weber, and E. Ungewickell, "Clathrin assembly protein AP180: primary structure, domain organization and identification of a clathrin binding site," *EMBO J.*, vol. 12, pp. 667–675, Feb 1993.

[69] B. Zhang, Y. H. Koh, R. B. Beckstead, V. Budnik, B. Ganetzky, and H. J. Bellen, "Synaptic vesicle size and number are regulated by a clathrin adaptor protein required for endocytosis," *Neuron*, vol. 21, pp. 1465–1475, Dec 1998.

[70] A. E. Salcini, H. Chen, G. Iannolo, P. De Camilli, and P. P. Di Fiore, "Epidermal growth factor pathway substrate 15, Eps15," *Int. J. Biochem. Cell Biol.*, vol. 31, pp. 805–809, Aug 1999.

[71] H. Chen, S. Fre, V. I. Slepnev, M. R. Capua, K. Takei, M. H. Butler, P. P. Di Fiore, and P. De Camilli, "Epsin is an EH-domain-binding protein implicated in clathrin-mediated endocytosis," *Nature*, vol. 394, pp. 793–797, Aug 1998.

[72] P. S. McPherson, E. de Heuvel, J. Phillie, W. Wang, A. Sengar, and S. Egan, "EH domain-dependent interactions between Eps15 and clathrin-coated vesicle protein p95," *Biochem. Biophys. Res. Commun.*, vol. 244, pp. 701–705, Mar 1998.

[73] M. T. Drake, M. A. Downs, and L. M. Traub, "Epsin binds to clathrin by associating directly with the clathrin-terminal domain. Evidence for cooperative binding through two discrete sites," *J. Biol. Chem.*, vol. 275, pp. 6479–6489, Mar 2000.

[74] T. Itoh, S. Koshiba, T. Kigawa, A. Kikuchi, S. Yokoyama, and T. Takenawa, "Role of the ENTH domain in phosphatidylinositol-4,5-bisphosphate binding and endocytosis," *Science*, vol. 291, pp. 1047–1051, Feb 2001.

[75] M. G. Ford, I. G. Mills, B. J. Peter, Y. Vallis, G. J. Praefcke, P. R. Evans, and H. T. McMahon, "Curvature of clathrin-coated pits driven by epsin," *Nature*, vol. 419, pp. 361–366, Sep 2002.

[76] P. N. Dannhauser and E. J. Ungewickell, "Reconstitution of clathrin-coated bud and vesicle formation with minimal components," *Nat. Cell Biol.*, vol. 14, pp. 634–639, Jun 2012.

[77] M. S. Chen, R. A. Obar, C. C. Schroeder, T. W. Austin, C. A. Poodry, S. C. Wadsworth, and R. B. Vallee, "Multiple forms of dynamin are encoded by shibire, a Drosophila gene involved in endocytosis," *Nature*, vol. 351, pp. 583–586, Jun 1991.

[78] A. M. van der Bliek, T. E. Redelmeier, H. Damke, E. J. Tisdale, E. M. Meyerowitz, and S. L. Schmid, "Mutations in human dynamin block an intermediate stage in coated vesicle formation," *J. Cell Biol.*, vol. 122, pp. 553–563, Aug 1993.

[79] E. Ungewickell, H. Ungewickell, S. E. Holstein, R. Lindner, K. Prasad, W. Barouch, B. Martin, L. E. Greene, and E. Eisenberg, "Role of auxilin in uncoating clathrin-coated vesicles," *Nature*, vol. 378, pp. 632–635, Dec 1995.

[80] D. M. Schlossman, S. L. Schmid, W. A. Braell, and J. E. Rothman, "An enzyme that removes clathrin coats: purification of an uncoating ATPase," *J. Cell Biol.*, vol. 99, pp. 723–733, Aug 1984.

[81] Y. I. Yim, T. Sun, L. G. Wu, A. Raimondi, P. De Camilli, E. Eisenberg, and L. E. Greene, "Endocytosis and clathrin-uncoating defects at synapses of auxilin knockout mice," *Proc. Natl. Acad. Sci. U.S.A.*, vol. 107, pp. 4412–4417, Mar 2010.

[82] A. Umeda, A. Meyerholz, and E. Ungewickell, "Identification of the universal cofactor (auxilin 2) in clathrin coat dissociation," *Eur. J. Cell Biol.*, vol. 79, pp. 336–342, May 2000.

[83] U. Scheele, C. Kalthoff, and E. Ungewickell, "Multiple interactions of auxilin 1 with clathrin and the AP-2 adaptor complex," *J. Biol. Chem.*, vol. 276, pp. 36131–36138, Sep 2001.

[84] A. Fotin, Y. Cheng, N. Grigorieff, T. Walz, S. C. Harrison, and T. Kirchhausen, "Structure of an auxilin-bound clathrin coat and its implications for the mechanism of uncoating," *Nature*, vol. 432, pp. 649–653, Dec 2004.

[85] I. Rapoport, W. Boll, A. Yu, T. Bocking, and T. Kirchhausen, "A motif in the clathrin heavy chain required for the Hsc70/auxilin uncoating reaction," *Mol. Biol. Cell*, vol. 19, pp. 405–413, Jan 2008.

[86] H. T. McMahon and J. L. Gallop, "Membrane curvature and mechanisms of dynamic cell membrane remodelling," *Nature*, vol. 438, pp. 590–596, Dec 2005.

[87] J. C. Stachowiak, F. M. Brodsky, and E. A. Miller, "A cost-benefit analysis of the physical mechanisms of membrane curvature," *Nature cell biology*, vol. 15, no. 9, pp. 1019–1027, 2013.

[88] B. Antonny, P. Gounon, R. Schekman, and L. Orci, "Self-assembly of minimal COPII cages," *EMBO Rep.*, vol. 4, pp. 419–424, Apr 2003.

[89] M. Kinuta, H. Yamada, T. Abe, M. Watanabe, S. A. Li, A. Kamitani, T. Yasuda, T. Matsukawa, H. Kumon, and K. Takei, "Phosphatidylinositol 4,5-bisphosphate stimulates vesicle formation from liposomes by brain cytosol," *Proc. Natl. Acad. Sci. U.S.A.*, vol. 99, pp. 2842–2847, Mar 2002.

[90] S. Honing, D. Ricotta, M. Krauss, K. Spate, B. Spolaore, A. Motley, M. Robinson, C. Robinson, V. Haucke, and D. J. Owen, "Phosphatidylinositol-(4,5)-bisphosphate regulates sorting signal recognition by the clathrin-associated adaptor complex AP2," *Mol. Cell*, vol. 18, pp. 519–531, May 2005.

[91] P. B. Canham, "The minimum energy of bending as a possible explanation of the biconcave shape of the human red blood cell," *J. Theor. Biol.*, vol. 26, pp. 61–81, Jan 1970.

[92] W. Helfrich, "Elastic properties of lipid bilayers: theory and possible experiments," *Z Naturforsch C*, vol. 28, no. 11, pp. 693–703, 1973.

[93] E. Evans and W. Rawicz, "Entropy-driven tension and bending elasticity in condensed-fluid membranes," *Physical Review Letters*, vol. 64, no. 17, p. 2094, 1990.

[94] W. K. den Otter and W. J. Briels, "The generation of curved clathrin coats from flat plaques," *Traffic*, vol. 12, no. 10, pp. 1407–1416, 2011.

[95] M. Saleem, S. Morlot, A. Hohendahl, J. Manzi, M. Lenz, and A. Roux, "A balance between membrane elasticity and polymerization energy sets the shape of spherical clathrin coats," *Nat Commun*, vol. 6, p. 6249, 2015.

[96] W. C. Chan, "Bionanotechnology progress and advances," *Biology of Blood and Marrow Transplantation*, vol. 12, no. 1, pp. 87–91, 2006.

[97] J.-M. Lehn, "Toward self-organization and complex matter," *Science*, vol. 295, no. 5564, pp. 2400–2403, 2002.

[98] R. Jones, "Why nanotechnology needs better polymer chemistry," *Nature nanotechnology*, vol. 3, no. 12, pp. 699–700, 2008.

[99] S. Iijima, "Helical microtubules of graphitic carbon," *nature*, vol. 354, no. 6348, pp. 56–58, 1991.

[100] N. C. Seeman, "DNA engineering and its application to nanotechnology," *Trends Biotechnol.*, vol. 17, pp. 437–443, Nov 1999.

[101] N. C. Seeman, "Nucleic acid junctions and lattices," *Journal of Theoretical Biology*, vol. 99, no. 2, pp. 237 – 247, 1982.

[102] J. H. Chen and N. C. Seeman, "Synthesis from DNA of a molecule with the connectivity of a cube," *Nature*, vol. 350, pp. 631–633, Apr 1991.

[103] Y. Zhang and N. C. Seeman, "Construction of a dna-truncated octahedron," *Journal of the American Chemical Society*, vol. 116, no. 5, pp. 1661–1669, 1994.

[104] E. Winfree, F. Liu, L. A. Wenzler, and N. C. Seeman, "Design and self-assembly of two-dimensional DNA crystals," *Nature*, vol. 394, pp. 539–544, Aug 1998.

[105] P. W. Rothemund, N. Papadakis, and E. Winfree, "Algorithmic self-assembly of DNA Sierpinski triangles," *PLoS Biol.*, vol. 2, p. e424, Dec 2004.

[106] P. W. Rothemund, "Folding DNA to create nanoscale shapes and patterns," *Nature*, vol. 440, pp. 297–302, Mar 2006.

[107] M. Endo, K. Hidaka, T. Kato, K. Namba, and H. Sugiyama, "Dna prism structures constructed by folding of multiple rectangular arms," *Journal of the American Chemical Society*, vol. 131, no. 43, pp. 15570–15571, 2009.

[108] Y. Ke, J. Sharma, M. Liu, K. Jahn, Y. Liu, and H. Yan, "Scaffolded dna origami of a dna tetrahedron molecular container," *Nano Letters*, vol. 9, no. 6, pp. 2445–2447, 2009.

[109] E. S. Andersen, M. Dong, M. M. Nielsen, K. Jahn, R. Subramani, W. Mamdouh, M. M. Golas, B. Sander, H. Stark, C. L. Oliveira, J. S. Pedersen, V. Birkedal, F. Besenbacher, K. V. Gothelf, and J. Kjems, "Self-assembly of a nanoscale DNA box with a controllable lid," *Nature*, vol. 459, pp. 73–76, May 2009.

[110] C. A. Mirkin, R. L. Letsinger, R. C. Mucic, and J. J. Storhoff, "A DNA-based method for rationally assembling nanoparticles into macroscopic materials," *Nature*, vol. 382, pp. 607–609, Aug 1996.

[111] A. P. Alivisatos, K. P. Johnsson, X. Peng, T. E. Wilson, C. J. Loweth, M. P. Bruchez, and P. G. Schultz, "Organization of 'nanocrystal molecules' using DNA," *Nature*, vol. 382, pp. 609–611, Aug 1996.

[112] J. Zhang, Y. Liu, Y. Ke, and H. Yan, "Periodic square-like gold nanoparticle arrays templated by self-assembled 2D DNA Nanogrids on a surface," *Nano Lett.*, vol. 6, pp. 248–251, Feb 2006.

[113] H. Bui, C. Onodera, C. Kidwell, Y. Tan, E. Graugnard, W. Kuang, J. Lee, W. B. Knowlton, B. Yurke, and W. L. Hughes, "Programmable periodicity of quantum dot arrays with DNA origami nanotubes," *Nano Lett.*, vol. 10, pp. 3367–3372, Sep 2010.

[114] S. H. Park, P. Yin, Y. Liu, J. H. Reif, T. H. LaBean, and H. Yan, "Programmable dna self-assemblies for nanoscale organization of ligands and proteins," *Nano Letters*, vol. 5, no. 4, pp. 729–733, 2005.

[115] S. H. Park, C. Pistol, S. J. Ahn, J. H. Reif, A. R. Lebeck, C. Dwyer, and T. H. LaBean, "Finite-size, fully addressable dna tile lattices formed by hierarchical assembly procedures," *Angewandte Chemie International Edition*, vol. 45, no. 5, pp. 735–739, 2006.

[116] B. Saccà, R. Meyer, M. Erkelenz, K. Kiko, A. Arndt, H. Schroeder, K. S. Rabe, and C. M. Niemeyer, "Orthogonal protein decoration of dna origami," *Angewandte Chemie International Edition*, vol. 49, no. 49, pp. 9378–9383, 2010.

[117] A. V. Pinheiro, D. Han, W. M. Shih, and H. Yan, "Challenges and opportunities for structural DNA nanotechnology," *Nat Nanotechnol*, vol. 6, pp. 763–772, Dec 2011.

[118] R. de la Rica and H. Matsui, "Applications of peptide and protein-based materials in bionanotechnology," *Chem Soc Rev*, vol. 39, pp. 3499–3509, Sep 2010.

[119] M. T. Klem, D. Willits, M. Young, and T. Douglas, "2-d array formation of genetically engineered viral cages on au surfaces and imaging by atomic force microscopy," *Journal of the American Chemical Society*, vol. 125, no. 36, pp. 10806–10807, 2003.

[120] T. Douglas, E. Strable, D. Willits, A. Aitouchen, M. Libera, and M. Young, "Protein engineering of a viral cage for constrained nanomaterials synthesis," *Advanced materials*, vol. 14, no. 6, pp. 415–418, 2002.

[121] T. Douglas and M. Young, "Host–guest encapsulation of materials by assembled virus protein cages," *Nature*, vol. 393, no. 6681, pp. 152–155, 1998.

[122] A. Abbing, U. K. Blaschke, S. Grein, M. Kretschmar, C. M. Stark, M. J. Thies, J. Walter, M. Weigand, D. C. Woith, J. Hess, and C. O. Reiser, "Efficient intracellular delivery of a protein and a low molecular weight substance via recombinant polyomavirus-like particles," *J. Biol. Chem.*, vol. 279, pp. 27410–27421, Jun 2004.

[123] S. IWASHITA and S. KANEGASAKI, "Enzymic and molecular properties of base-plate parts of bacteriophage p22," *European Journal of Biochemistry*, vol. 65, no. 1, pp. 87–94, 1976.

[124] J. King and U. K. Laemmli, "Polypeptides of the tail fibres of bacteriophage T4," *J. Mol. Biol.*, vol. 62, pp. 465–477, Dec 1971.

[125] A. Mitraki and M. J. van Raaij, "Folding of β-structured fibrous proteins and self-assembling peptides," in *Protein Nanotechnology*, pp. 125–140, Springer, 2005.

[126] J. D. Sipe and A. S. Cohen, "Review: history of the amyloid fibril," *J. Struct. Biol.*, vol. 130, pp. 88–98, Jun 2000.

[127] A. T. Petkova, Y. Ishii, J. J. Balbach, O. N. Antzutkin, R. D. Leapman, F. Delaglio, and R. Tycko, "A structural model for alzheimer's β-amyloid fibrils based on experimental constraints from solid state nmr," *Proceedings of the National Academy of Sciences*, vol. 99, no. 26, pp. 16742–16747, 2002.

[128] J. I. Gallea and M. S. Celej, "Structural insights into amyloid oligomers of the Parkinson disease-related protein α-synuclein," *J. Biol. Chem.*, vol. 289, pp. 26733–26742, Sep 2014.

[129] T. Shirahama and A. S. Cohen, "High-resolution electron microscopic analysis of the amyloid fibril," *J. Cell Biol.*, vol. 33, pp. 679–708, Jun 1967.

[130] I. Cherny and E. Gazit, "Amyloids: not only pathological agents but also ordered nanomaterials," *Angew. Chem. Int. Ed. Engl.*, vol. 47, no. 22, pp. 4062–4069, 2008.

[131] A. S. Mostaert, C. Giordani, R. Crockett, U. Karsten, R. Schumann, and S. P. Jarvis, "Characterisation of amyloid nanostructures in the natural adhesive of unicellular subaerial algae," *The Journal of Adhesion*, vol. 85, no. 8, pp. 465–483, 2009.

[132] D. Losic, L. L. Martin, M.-I. Aguilar, and D. H. Small, "β-amyloid fibril formation is promoted by step edges of highly oriented pyrolytic graphite," *Peptide Science*, vol. 84, no. 5, pp. 519–526, 2006.

[133] C. Li, J. Adamcik, and R. Mezzenga, "Biodegradable nanocomposites of amyloid fibrils and graphene with shape-memory and enzyme-sensing properties," *Nature nanotechnology*, vol. 7, no. 7, pp. 421–427, 2012.

[134] A. S. Mostaert and S. P. Jarvis, "Beneficial characteristics of mechanically functional amyloid fibrils evolutionarily preserved in natural adhesives," *Nanotechnology*, vol. 18, no. 4, p. 044010, 2007.

[135] C. Li and R. Mezzenga, "The interplay between carbon nanomaterials and amyloid fibrils in bio-nanotechnology," *Nanoscale*, vol. 5, no. 14, pp. 6207–6218, 2013.

[136] Y. Wang, M. M. Modena, M. Platen, I. A. T. Schaap, and T. P. Burg, "Label-free measurement of amyloid elongation by suspended microchannel resonators," *Analytical chemistry*, vol. 87, no. 3, pp. 1821–1828, 2015.

[137] U. B. Sleytr, P. Messner, D. Pum, and M. Sára, "Crystalline bacterial cell surface layers (s layers): from supramolecular cell structure to biomimetics and nanotechnology," *Angewandte Chemie International Edition*, vol. 38, no. 8, pp. 1034–1054, 1999.

[138] U. B. Sleytr, "Heterologous reattachment of regular arrays of glycoproteins on bacterial surfaces," *Nature*, vol. 257, pp. 400–402, Oct 1975.

[139] U. B. Sleytr, "Regular arrays of macromolecules on bacterial cell walls: structure, chemistry, assembly, and function.," *International review of cytology*, vol. 53, p. 1, 1978.

[140] B. Schuster, E. Györvary, D. Pum, and U. B. Sleytr, "Nanotechnology with s-layer proteins," in *Protein Nanotechnology*, pp. 101–123, Springer, 2005.

[141] D. Pum, M. Sára, and U. Sleytr, "Structure, surface charge, and self-assembly of the s-layer lattice from bacillus coagulans e38-66.," *Journal of bacteriology*, vol. 171, no. 10, pp. 5296–5303, 1989.

[142] S. Weigert and M. Sára, "Surface modification of an ultrafiltration membrane with crystalline structure and studies on interactions with selected protein molecules," *Journal of Membrane Science*, vol. 106, no. 1–2, pp. 147 − 159, 1995.

[143] U. B. Sleytr, E. M. Egelseer, N. Ilk, D. Pum, and B. Schuster, "S-layers as a basic building block in a molecular construction kit," *Febs Journal*, vol. 274, no. 2, pp. 323–334, 2007.

[144] J. C. Sinclair, K. M. Davies, C. Vénien-Bryan, and M. E. Noble, "Generation of protein lattices by fusing proteins with matching rotational symmetry," *Nature nanotechnology*, vol. 6, no. 9, pp. 558–562, 2011.

[145] A. P. Schoen, D. T. Schoen, K. N. Huggins, M. A. Arunagirinathan, and S. C. Heilshorn, "Template engineering through epitope recognition: A modular, biomimetic strategy for inorganic nanomaterial synthesis," *Journal of the American Chemical Society*, vol. 133, no. 45, pp. 18202–18207, 2011.

[146] N. Hom, K. R. Mehta, T. Chou, A. B. Foraker, F. M. Brodsky, K. Kirshenbaum, and J. K. Montclare, "Anisotropic nanocrystal arrays organized on protein lattices formed by recombinant clathrin fragments," *Journal of materials chemistry*, vol. 22, no. 44, pp. 23335–23339, 2012.

[147] L. Hinrichsen, A. Meyerholz, S. Groos, and E. J. Ungewickell, "Bending a membrane: how clathrin affects budding," *Proceedings of the National Academy of Sciences*, vol. 103, no. 23, pp. 8715–8720, 2006.

[148] A. Ortega-Esteban, I. Horcas, M. Hernando-Pérez, P. Ares, A. Pérez-Berná, C. San Martín, J. Carrascosa, P. De Pablo, and J. Gómez-Herrero, "Minimizing tip–sample forces in jumping mode atomic force microscopy in liquid," *Ultramicroscopy*, vol. 114, pp. 56–61, 2012.

[149] N. Burnham, X. Chen, C. Hodges, G. Matei, E. Thoreson, C. Roberts, M. Davies, and S. Tendler, "Comparison of calibration methods for atomic-force microscopy cantilevers," *Nanotechnology*, vol. 14, no. 1, p. 1, 2003.

[150] I. A. Schaap, C. Carrasco, P. J. de Pablo, and C. F. Schmidt, "Kinesin walks the line: single motors observed by atomic force microscopy," *Biophys. J.*, vol. 100, pp. 2450–2456, May 2011.

[151] I. Horcas, R. Fernández, J. M. Gómez-Rodríguez, J. Colchero, J. Gómez-Herrero, and A. M. Baro, "Wsxm: A software for scanning probe microscopy and a tool for nanotechnology," *Review of Scientific Instruments*, vol. 78, no. 1, pp. –, 2007.

[152] T. P. Burg, M. Godin, S. M. Knudsen, W. Shen, G. Carlson, J. S. Foster, K. Babcock, and S. R. Manalis, "Weighing of biomolecules, single cells and single nanoparticles in fluid," *Nature*, vol. 446, no. 7139, pp. 1066–1069, 2007.

[153] T. P. Burg and S. R. Manalis, "Suspended microchannel resonators for biomolecular detection," *Applied Physics Letters*, vol. 83, no. 13, pp. 2698–2700, 2003.

[154] T. P. Burg, A. R. Mirza, N. Milovic, C. H. Tsau, G. Popescu, J. S. Foster, S. R. Manalis, *et al.*, "Vacuum-packaged suspended microchannel resonant mass sensor for biomolecular detection," *Microelectromechanical Systems, Journal of*, vol. 15, no. 6, pp. 1466–1476, 2006.

[155] M. M. Modena, Y. Wang, D. Riedel, and T. P. Burg, "Resolution enhancement of suspended microchannel resonators for weighing of biomolecular complexes in solution," *Lab on a Chip*, vol. 14, no. 2, pp. 342–350, 2014.

[156] K. Gekko and H. Noguchi, "Compressibility of globular proteins in water at 25. degree. c," *Journal of Physical Chemistry*, vol. 83, no. 21, pp. 2706–2714, 1979.

[157] P. G. Squire and M. E. Himmel, "Hydrodynamics and protein hydration," *Archives of biochemistry and biophysics*, vol. 196, no. 1, pp. 165–177, 1979.

[158] I. Kuntz Jr and W. Kauzmann, "Hydration of proteins and polypeptides.," *Advances in protein chemistry*, vol. 28, pp. 239–345, 1974.

[159] C. Kalthoff, J. Alves, C. Urbanke, R. Knorr, and E. J. Ungewickell, "Unusual structural organization of the endocytic proteins AP180 and epsin 1," *J. Biol. Chem.*, vol. 277, pp. 8209–8216, Mar 2002.

[160] J. H. Keen, M. C. Willingham, and I. H. Pastan, "Clathrin-coated vesicles: isolation, dissociation and factor-dependent reassociation of clathrin baskets," *Cell*, vol. 16, pp. 303–312, Feb 1979.

[161] E. Ungewickell and H. Ungewickell, "Bovine brain clathrin light chains impede heavy chain assembly in vitro," *J. Biol. Chem.*, vol. 266, pp. 12710–12714, Jul 1991.

[162] F. K. Winkler and K. K. Stanley, "Clathrin heavy chain, light chain interactions," *EMBO J.*, vol. 2, no. 8, pp. 1393–1400, 1983.

[163] A. Hoffmann, P. N. Dannhauser, S. Groos, L. Hinrichsen, U. Curth, and E. J. Ungewickell, "A comparison of GFP-tagged clathrin light chains with fluorochromated light chains in vivo and in vitro," *Traffic*, vol. 11, pp. 1129–1140, Sep 2010.

[164] S. Holstein, H. Ungewickell, and E. Ungewickell, "Mechanism of clathrin basket dissociation: separate functions of protein domains of the dnaj homologue auxilin.," *The Journal of cell biology*, vol. 135, no. 4, pp. 925–937, 1996.

[165] J. Erhardt and H. Dirr, "Native dimer stabilizes the subunit tertiary structure of porcine class pi glutathione S-transferase," *Eur. J. Biochem.*, vol. 230, pp. 614–620, Jun 1995.

[166] S. H. Liu, M. L. Wong, C. S. Craik, and F. M. Brodsky, "Regulation of clathrin assembly and trimerization defined using recombinant triskelion hubs," *Cell*, vol. 83, pp. 257–267, Oct 1995.

[167] J. D. Wilbur, P. K. Hwang, J. A. Ybe, M. Lane, B. D. Sellers, M. P. Jacobson, R. J. Fletterick, and F. M. Brodsky, "Conformation switching of clathrin light chain regulates clathrin lattice assembly," *Dev. Cell*, vol. 18, pp. 841–848, May 2010.

[168] F. Huang, A. Khvorova, W. Marshall, and A. Sorkin, "Analysis of clathrin-mediated endocytosis of epidermal growth factor receptor by RNA interference," *J. Biol. Chem.*, vol. 279, pp. 16657–16661, Apr 2004.

[169] V. Poupon, M. Girard, V. Legendre-Guillemin, S. Thomas, L. Bourbonniere, J. Philie, N. A. Bright, and P. S. McPherson, "Clathrin light chains function in mannose phosphate receptor trafficking via regulation of actin assembly," *Proc. Natl. Acad. Sci. U.S.A.*, vol. 105, pp. 168–173, Jan 2008.

[170] S. L. Schmid, A. K. Matsumoto, and J. E. Rothman, "A domain of clathrin that forms coats," *Proc. Natl. Acad. Sci. U.S.A.*, vol. 79, pp. 91–95, Jan 1982.

[171] P. Nandi and P. Wahl, "Diffusion properties of clathrin on the surface of isolated mouse liver nuclei by the fluorescence recovery after photobleaching technique," *Biochim. Biophys. Acta*, vol. 943, pp. 367–370, Aug 1988.

[172] M. T. Drake and L. M. Traub, "Interaction of two structurally distinct sequence types with the clathrin terminal domain beta-propeller," *J. Biol. Chem.*, vol. 276, pp. 28700–28709, Aug 2001.

[173] V. I. Slepnev, G. C. Ochoa, M. H. Butler, and P. De Camilli, "Tandem arrangement of the clathrin and AP-2 binding domains in amphiphysin 1 and disruption of clathrin coat function by amphiphysin fragments comprising these sites," *J. Biol. Chem.*, vol. 275, pp. 17583–17589, Jun 2000.

[174] M. Ehrlich, W. Boll, A. Van Oijen, R. Hariharan, K. Chandran, M. L. Nibert, and T. Kirchhausen, "Endocytosis by random initiation and stabilization of clathrin-coated pits," *Cell*, vol. 118, pp. 591–605, Sep 2004.

[175] F. Ferreira, M. Foley, A. Cooke, M. Cunningham, G. Smith, R. Woolley, G. Henderson, E. Kelly, S. Mundell, and E. Smythe, "Endocytosis of G protein-coupled receptors is regulated by clathrin light chain phosphorylation," *Curr. Biol.*, vol. 22, pp. 1361–1370, Aug 2012.

[176] K. M. Huang, L. Gullberg, K. K. Nelson, C. J. Stefan, K. Blumer, and S. K. Lemmon, "Novel functions of clathrin light chains: clathrin heavy chain trimerization is defective in light chain-deficient yeast," *J. Cell. Sci.*, vol. 110 (Pt 7), pp. 899–910, Apr 1997.

[177] J. A. Ybe, S. Perez-Miller, Q. Niu, D. A. Coates, M. W. Drazer, and M. E. Clegg, "Light chain C-terminal region reinforces the stability of clathrin heavy chain trimers," *Traffic*, vol. 8, pp. 1101–1110, Aug 2007.

[178] J. A. Ybe, S. N. Fontaine, T. Stone, J. Nix, X. Lin, and S. Mishra, "Nuclear localization of clathrin involves a labile helix outside the trimerization domain," *FEBS Lett.*, vol. 587, pp. 142–149, Jan 2013.

[179] A. Copic, C. F. Latham, M. A. Horlbeck, J. G. D'Arcangelo, and E. A. Miller, "ER cargo properties specify a requirement for COPII coat rigidity mediated by Sec13p," *Science*, vol. 335, pp. 1359–1362, Mar 2012.

[180] S. Köhler, F. Schmid, and G. Settanni, "The flexibility of fibrinogen and its initial adsorption stages at the graphite and mica surface," in *NIC Symposium 2014-Proceedings: 12–13 February 2014 | Jülich, Germany*, p. 117, Forschungszentrum Jülich, 2014.

[181] P. K. Nandi and H. Edelhoch, "The effects of lyotropic (Hofmeister) salts on the stability of clathrin coat structure in coated vesicles and baskets," *J. Biol. Chem.*, vol. 259, pp. 11290–11296, Sep 1984.

[182] T. Gervais and K. F. Jensen, "Mass transport and surface reactions in microfluidic systems," *Chemical engineering science*, vol. 61, no. 4, pp. 1102–1121, 2006.

[183] M. L. Watson, "Staining of tissue sections for electron microscopy with heavy metals," *The Journal of Biophysical and Biochemical Cytology*, vol. 4, no. 4, pp. 475–478, 1958.

[184] P. J. de Pablo, I. A. Schaap, F. C. MacKintosh, and C. F. Schmidt, "Deformation and collapse of microtubules on the nanometer scale," *Phys. Rev. Lett.*, vol. 91, p. 098101, Aug 2003.

[185] I. A. Schaap, C. Carrasco, P. J. de Pablo, F. C. MacKintosh, and C. F. Schmidt, "Elastic response, buckling, and instability of microtubules under radial indentation," *Biophys. J.*, vol. 91, pp. 1521–1531, Aug 2006.

[186] M. Baclayon, G. Wuite, and W. Roos, "Imaging and manipulation of single viruses by atomic force microscopy," *Soft Matter*, vol. 6, no. 21, pp. 5273–5285, 2010.

[187] A. J. Perez-Berna, A. Ortega-Esteban, R. Menendez-Conejero, D. C. Winkler, M. Menendez, A. C. Steven, S. J. Flint, P. J. de Pablo, and C. San Martin, "The role of capsid maturation on adenovirus priming for sequential uncoating," *J. Biol. Chem.*, vol. 287, pp. 31582–31595, Sep 2012.

[188] S. Garcia-Manyes and F. Sanz, "Nanomechanics of lipid bilayers by force spectroscopy with AFM: a perspective," *Biochim. Biophys. Acta*, vol. 1798, pp. 741–749, Apr 2010.

[189] J. L. Toca-Herrera, S. Moreno-Flores, J. Friedmann, D. Pum, and U. B. Sleytr, "Chemical and thermal denaturation of crystalline bacterial S-layer proteins: an atomic force microscopy study," *Microsc. Res. Tech.*, vol. 65, pp. 226–234, Nov 2004.

LIST OF FIGURES

LIST OF TABLES

APPENDIX

ADDITIONAL PROJECTS

1.1 CLATHRIN CAGES

While studying the mechanics of clathrin cages, with and without clathrin light chains, the idea arose to also examine the effect of different adaptor proteins on the cage stability. Since it was suggested that AP180 stabilizes and auxilin destabilizes the cage, these two adaptor proteins were the first choice.

While scanning the cage in amplitude modulation (Cypher: Asylum Research; OMCL-TR400PSA: Olympus) it was observed that images of cages without adaptor proteins as well as cages with AP180 can be obtained without problems. In contrast, cages with auxilin were breaking during the scan (Fig. 47).

Malte Warias studied the mechanics of this cages in more detail during his bachelor
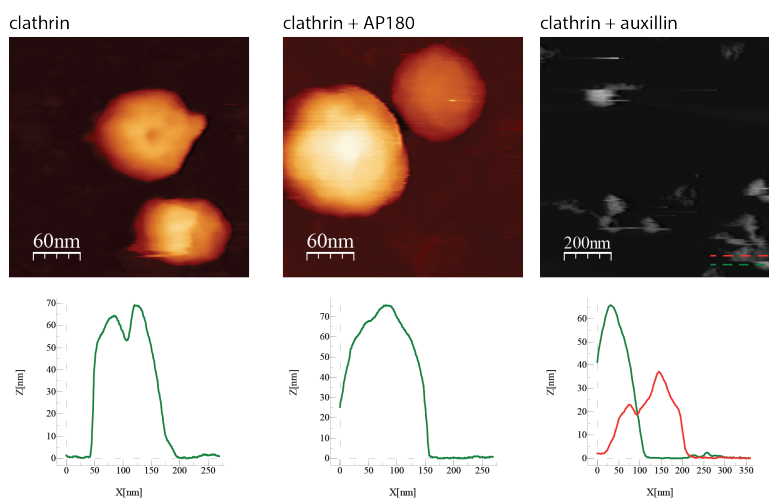

Figure 47: Images of clathrin cages with and without adaptor proteins. Cages with auxilin break half way during scanning (red profile).

thesis, and confirmed that adaptor proteins influence clathrin cage mechanics. Cages with attached AP180 seem to be almost twice as stable as cages without any adaptor proteins. In contrast, cages with auxilin seem slightly less stable (Fig. 48). Force

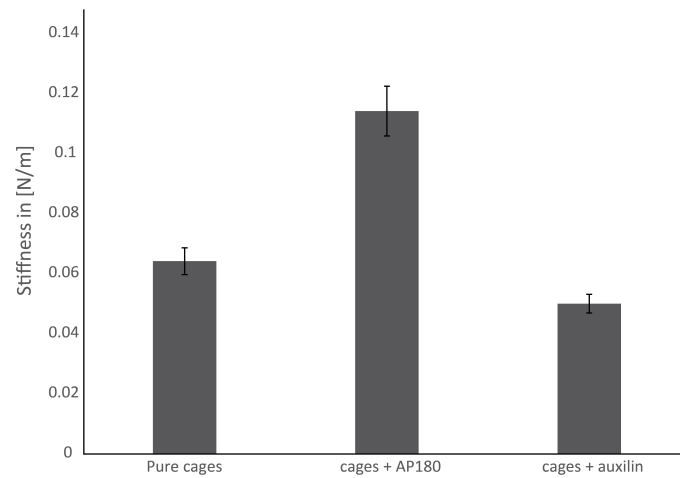curves were recorded with an MFP3D microscope (Asylum Research) and OMCL-TR400PSA cantilever (Olympus).

Figure 48: Mechanical investigations of clathrin cages show that cages with AP180 are more stable, while cages with auxilin are less stable, compared to cages without any adaptor proteins.

1.2 PYRUVATE DEHYDROGENASE COMPLEX

Another fundamental project during the period of this PhD project was the investigation of the pyruvate dehydrogenase multienzyme complex (PDHc) with AFM.

The PDHc links glycolysis to the citric acid cycle by converting the central metabolite pyruvate into acetyl-CoA, a building block for many fundamental metabolic pathways. The core of the human PDHc consists of 60 dihydrolipoamide acetyltransferase enzymes (E2), which assemble into a dodecahedral structure (50 nm in diameter). A key trait vital to PDHc function is the flexibility of the N-terminal "swinging lipoyl domain" of E2, which is capable of reaching the active sites of all proximal enzyme components. Although low resolution structural information about the PDHc core is available, the underlying dynamics of catalysis, in particular substrate channeling, is not understood.

Here, one idea was to examine the effect of Coenzyme A (CoA) binding on the dynamics of the lipoyl domains (swinging arms) of the PDHc core. The hypothesis is that upon binding of CoA, these arms protrude inside the core and remain

there for an extended time period. Therefore, we assumed that the height of the core should decrease in the AFM images. Figure 49 indicates such a shift in height,
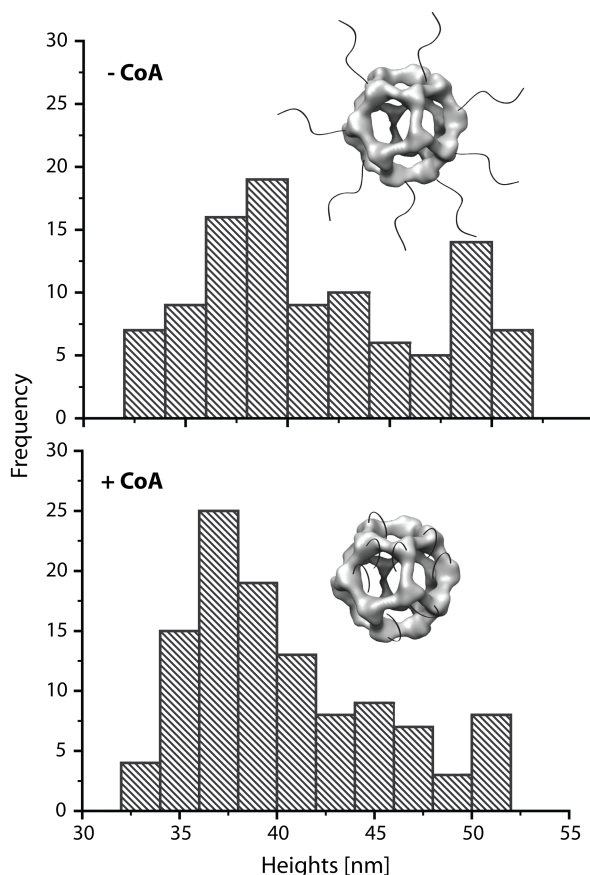

Figure 49: Shift in the height distribution of PDHc cores in presence of CoA.

when CoA was added to the sample. However, after optimization of the PDHc purification, the protein complexes seemed in general smaller compared to these results. The images were acquired with a MFP3D (Asylum Research) using BL-RC-150VB cantilevers (Olympus) in tapping mode. The cores were fixed on N-(3-trimethoxysilylpropyl)diethylenetriamine (DETA)-coated coverslips and heights were analyzed using a MATLAB routine by Maria Kilfoil, which allows to obtain the particle center positions. The core heights were averaged with respect to their radius of gyration.

Later on the height variations of different PDHc assemblies (human PDHc core (hPDHc),mixed hPDHc core (E2/E3 subunits), truncated hPDHc core (without swinging arms) and *E. coli* PDHc core (table 4) were analyzed. As expected, the *E. coli* PDHc core is much smaller (14 nm) compared to the human core (28 nm). The intro-

Table 4: Heights of different PDHc core assemblies

	mean height [nm]	std. error	N
hPDHc core	28.1	0.33	215
mixed hPDHc core	24.8	0.30	206
truncated hPDHc core	22.6	0.17	70
E. coli PDHc core	14.0	0.90	31
full hPDHc	29.6	0.88	37

duction of the E3 subunit to the human E2 core might compact the hPDHc core and removing the lipoyl domains reduces the height further to approximately 23 nm. The full hPDH complex (containing all subunits) shows a height of around 30 nm in the AFM measurements. Hereby, the adhesion to the surface might reduce the height of the PDHc drastically. Additionally, the cores might be deformed via scanning forces due to their extremely soft nature (effective spring constants: hPDHc core 0.03 N/m and mixed hPDHC core 0.04 N/m). The height analyses were performed using a home written MATLAB script (appendix 2.4).

1.3 SNARE CLUSTERS

In this project we were trying to complement results observed in stimulated emission depletion (STED) microscopy. Here, Dragomir Milovanovic was able to show that upon addition of Ca^{2+}, the transmembrane domain of the SNARE protein Syntaxin 1 (Sx1), in presence of phosphatidylinositol 4,5-bisphosphate (Pip2), aggregates to form clusters of around 160 nm in diameter.
We could show a flat membrane with total internal reflection (TIRF) microscopy and AFM, when lipid sheets of only phosphatidylserine (PS) lipids were created. Whereas, protein clusters could be observed when Sx1 and Pip2 were added in presence of Ca^{2+} (Fig. 50). Furthermore, the mean diameter of these clusters appears to be 160 nm (Fig. 51). While this mean diameter correlates very well with the previously obtained STED data, one needs to consider the problem of tip dilation in AFM. Using some simple geometrical calculations and taking into account a tip diameter of approximately 20 nm, an error of around 20 nm to 30 nm was estimated (based on Fig. 52 and MATLAB script 2.5).
Images were obtained using a MFP3D AFM (Asylum Research) with a home-build
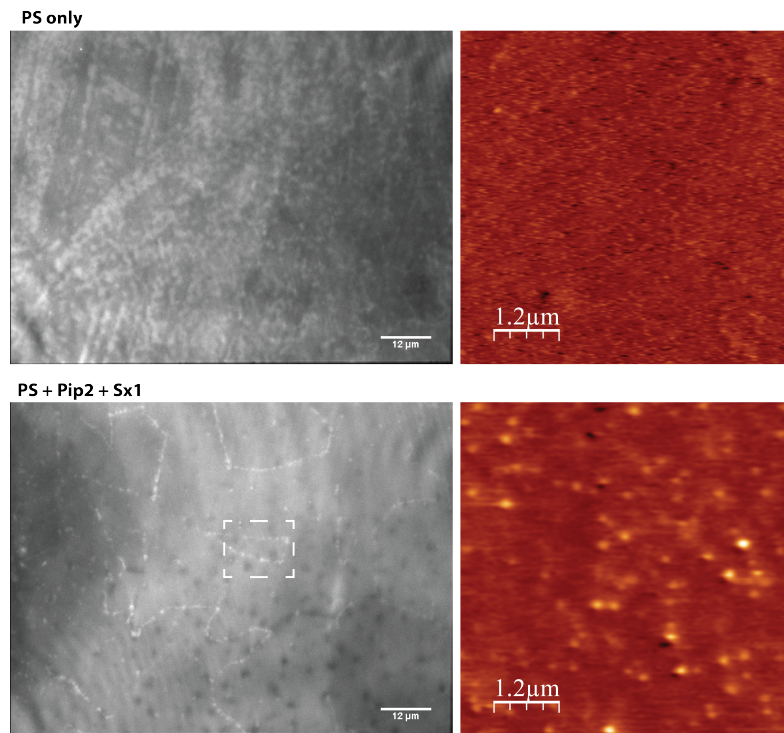
PS only

PS + Pip2 + Sx1

Figure 50: TIRF and AFM images of PS-only sheets and PS sheets containing Sx1 and Pip2 with Ca^{2+}. Protein clusters are visible under latter conditions.
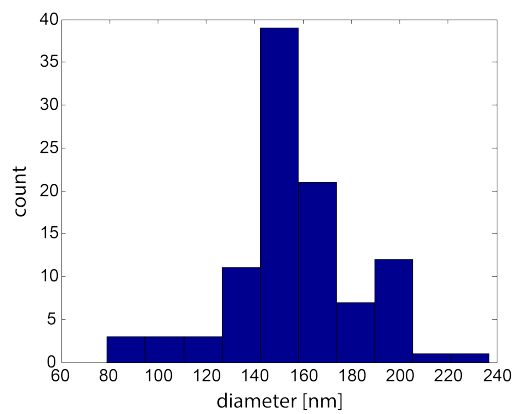

Figure 51: Histogram of the diameters obtained from Sx1 protein clusters in AFM measurements.
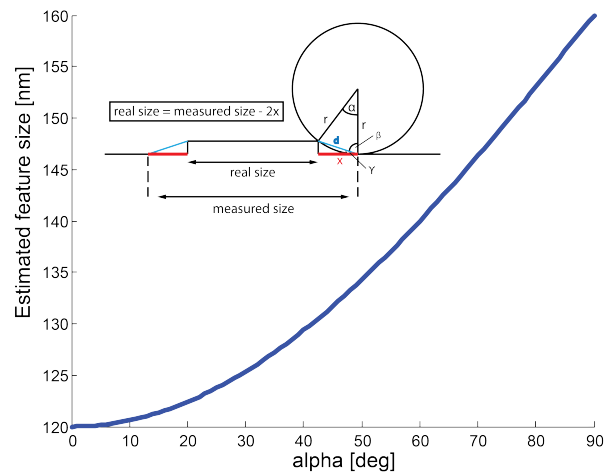
Figure 52: Estimation of the tip dilation when imaging the Sx1 clusters.

TIRF setup and BL-RC-150VB cantilever (Olympus).

In further experiments, we attempted to visualize the binding of the C2AB domain of synaptotagmin to the Sx1 transmembrane domain. The observations during this series of experiments might be explained by the phenomenon known as hydrophobic mismatch. Here, the transmembrane domain is shorter than the thickness of the lipid bilayer. Therefore, the hydrophobic parts in the membrane "squeeze" together to accommodate the length of the transmembrane domain, resulting in dents inside the membrane. In the AFM measurements dents of approximately 1 nm in depth were observed, which disappeared and changed to bulges after C2AB was added to the sample. Therefore, we speculate that the observed dents occur due to the hydrophobic mismatch caused by the short Sx1 domain, and upon binding of C2AB to this domain, the dents were filled (Fig. 53). Unfortunately, this experiment was hardly reproducible and, therefore, remains only a speculation.

Images were obtained using a "Cervantes Full Mode AFM System" (Nanotec) and BL-RC-150VB cantilever (Olympus).
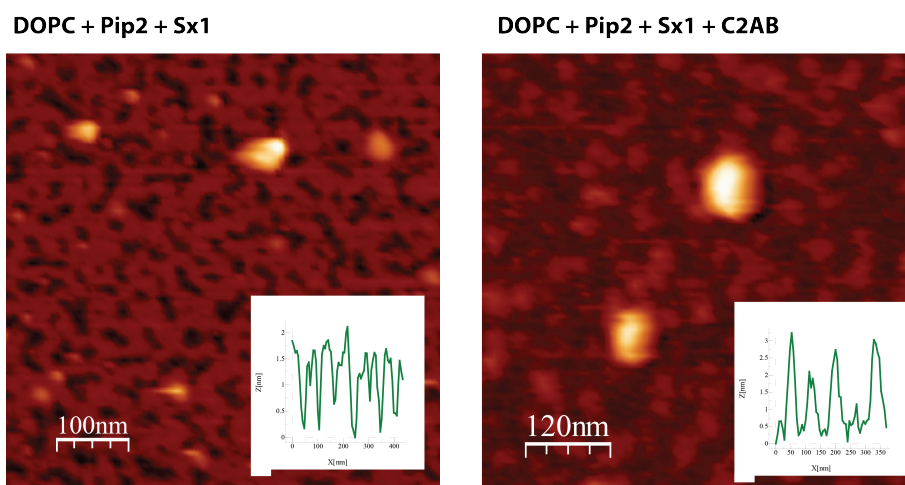
Figure 53: Sx1 is speculated to cause an hydrophobic mismatch and, therefore, introduces dents in the membrane surface. These dents are filled after binding of C2AB to the Sx1 domain.

MATLAB SCRIPTS

2.1 LATTICE HEIGHT CALCULATION

```matlab
% Calculates heights by using 95% of the data (cuts off 2.5% at both sides)
% average height = max - min of resulting histogram values

%read in all txt file names in current directory
files = dir('*.txt');
filenames = extractfield(files, 'name');
results = [];

for i = 1:length(filenames) %loop through all files
    name = filenames{i};

    data = importdata(name); %import data from text file
    data = data.data;

    data = sort(data(:)); %sort data ascended
    cutoff = round(0.025*length(data)); %calculate 2.5% of all data

    for ii = 1:cutoff %remove 2.5% of smallest values
        data(1) = [];
    end

    data = sort(data, 'descend'); %sort data descended

    for ii = 1:cutoff %remove 2.5% of heighest values
        data(1) = [];
    end

    [n,xout] = hist(data,100); %create histogram of remaining data
    figure(i), hist(data(:),100)
```

```
    height = max(xout) - min(xout); %calculate average height


    if height > 90 %no values heigher than 90nm expected
        height = height/10; %if heigher convert scale from A to nm
    end


    results = [results; {name num2str(height)}];
end
results %print results
```

2.2 RADIUS OF CURVATURE

```
y = smooth(a(:,2))
cftool(a(:,1),y)
RofCurv(a(:,1), fitted)
% fitted is output [constants] of polynomial fit


% function to calculate R of curvature
function R = RofCurv(x, f)


y = f.p1.*x.^2 + f.p2.*x + f.p3; % new y for parabola


[m n] = min(y); % get element number of minimum (n)


%calculate radius of curvature around minimum
R = (1 + (2*f.p1*x(n))^2)^(3/2) / abs(2*f.p1);


end
```

2.3 AREA BETWEEN EXTENSION AND RETRACTION CURVES

```
function results = ForceAreas(springConst)


files = dir('*.ibw');
filenames = extractfield(files, 'name');
```

```matlab
results = [];

for i = 1:length(filenames) %loop through all files
    name = filenames{i};

    [data, e, v] = read_wave(name, 'whatever', 'whatever');
    %read_wave function by Jason Bemis
    clear e;
    clear v;

    X = data(:,1);
    Y = data(:,2);
    conv = springConst * 0.001; % pN/nm to N/m
    Y = Y * conv; % converts nm deflection into force
    [N I] = max(Y); %split data to trace and retrace by finding max deflection
    extX = X(1:I);
    retX = X(I:length(X));
    extY = Y(1:I);
    retY = Y(I:length(Y));
    clear X;
    clear Y;
    clear N;

    retX = flipud(retX); %retraction data was upside down
    retY = flipud(retY);

    if extX(1) < retX(1) % get rid of beginning of too long ext curve
        while extX(1) < retX(1)
            extX(1) = [];
            extY(1) = [];
        end
    end

    figure(1), hold on
    plot(extX, extY, 'r')
    plot(retX, retY)
```

```
    [cursorX cursorY] = ginput(2);
    hold off
    close(1);

    [c ExtIndex1] = min(abs(extX-cursorX(1))); %find indices for the
    [c ExtIndex2] = min(abs(extX-cursorX(2))); %selection at the curves
    [c RetIndex1] = min(abs(retX-cursorX(1)));
    [c RetIndex2] = min(abs(retX-cursorX(2)));
    clear c;

    IntExt = trapz(extX(ExtIndex1:ExtIndex2), extY(ExtIndex1:ExtIndex2));
    IntRet = trapz(retX(RetIndex1:RetIndex2), retY(RetIndex1:RetIndex2));
    AreaBetweenExtRet =  IntExt - IntRet;
    AreaBetweenExtRet =  AreaBetweenExtRet * 10^21; %conversion from Nm to pNnnm
    results = [results; AreaBetweenExtRet];

end %for loop

end %function
```

2.4   PARTICLE HEIGHT DETERMINATION

```
%Determines the mean of the 10% highest pixels from picked
%particles from WsXM *.txt files

function heights = particleHeight(fname)

I = [];
heights = [];

data = importdata([fname '.txt']);
data = data.data;

data = rot90(data,2); %rotates image to original orientation

maximum = max(data(:));
```

```
15
   bitstep = maximum/255; % calculating the 8bit pixel value/nm


   imOFdata = [];
   for i = 1:length(data(1,:))
20     for ii = 1:length(data(:,1))
           imOFdata(ii,i) = round(data(ii,i)/bitstep);
       end
   end


25 imwrite(uint8(imOFdata),[fname '.tif'],'tiff'); %save as tif
   I = imread([fname '.tif']); %read in tif


   figure; imshow(I); caxis auto; hold on; %colormap(jet(256)) ;
   another = true;
30 while another == true % another round?
       try
       rect = getrect(); % rect(1) = xmin, rect(2) = ymin, rect(3) = width, rect(4)
            = height
       rectangle('Position',rect,'LineWidth',1.5,'LineStyle','--', 'EdgeColor', 'g'
           );


35


       % check whether rectangular is within image boundaries
       % and translate rect(x) into x/y coordinates
       if rect(1) < 1
40         xmin = 1;
       else
           xmin =  round(rect(1));
       end
       if rect(2) < 1
45         ymin = 1;
       else
           ymin = round(rect(2));
       end
       if xmin + rect(3) > length(I(1,:))
```

```matlab
50          xmax = length(I(1,:));
        else
            xmax = xmin + round(rect(3));
        end
        if ymin + rect(4) > length(I(:,1))
55          ymax = length(I(:,1));
        else
            ymax = ymin + round(rect(4));
        end

60      % get pixel values from rectangle and calculate height
        pxValues = [];
        for i = xmin:xmax
            for ii = ymin:ymax
                pxValues = [pxValues; data(ii,i)];
65          end
        end
        pxValues = sort(pxValues, 'descend');
        % calculate mean height for particle and store it
        elementHeight = mean(pxValues(1:round((10*length(pxValues))/100))); %mean of
            the highest 10%
70      heights = [heights; elementHeight];

        % cancel by e.g. right clicking
        catch
            another = ~another;
75      end

    end
    hold off;

80  end
```

2.5 ESTIMATION OF AFM TIP DILATION

```matlab
% Calculates an estimation of the real feature size of AFM images
```

```matlab
% returns the angle alpha and the calculated "real" size
% input:
% alpha start: start angle
% alpha_end: stop angle
% r: tip radius
% size: measure diameter of feature


function [alpha, realSize] = dilation(alpha_start, alpha_end, r, size)

alpha=[];
realSize=[];

for i = alpha_start:1:alpha_end
    alpha = [alpha i];
    d = sqrt(2*r^2*(1-cosd(i)));
    beta = (180-i)/2;
    gamma = 90- beta;
    x = cosd(gamma) * d;
    realSize = [realSize (size-(2*x))];
end
realSize = fliplr(realSize);
figure
plot(alpha, realSize,'b','LineWidth',3)
title('estimated size reduction vs. contact point')
xlabel('alpha [deg]')
ylabel('Estimated feature size [nm]')

end
```

Curriculum Vitae

Education

October 2012 - October 2015
> Doctor Rerum Naturalium
> Max Planck Research School, Göttingen, Germany
> Physics of Biology and Complex Systems

October 2010 - September 2012
> Master of Science
> BIOTEC, Technical University Dresden, Germany
> Molecular Bioengineering

October 2006 - February 2010
> Bachelor of Science
> University of Applied Science Aachen
> Biotechnology

October 2004 - July 2006
> Bachelor of Science (Canceled)
> University of Paderborn, Germany
> Electronic Engineering

August 2001 - July 2004
> Certified Technical Assistant in IT
> Felix-Fechenbach-Berufskolleg, Detmold, Germany

Conferences

March 2015
> Talk at DPG's Annual and Spring Meeting
> Technical University of Berlin, Germany
> Structural mechanics of protein lattices from clathrin

March 2014
> Proceedings Article (SPIE)
> Single-molecule fluorescence inside solid-state nanochannels
> Siddharth Ghosh, Manoj Kumbhakar, Mitja Platen, Ingo Gregora
> and Jörg Enderlein

March 2014
> Talk at Euro AFM Forum 2014
> Georg-August-University, Göttingen, Germany
> Structural mechanics of 2D & 3D lattices from clathrin proteins

Teaching Experience

March 2015 - August 2015
    Supervision of 2 Bachelor Students
    Georg-August-University, Göttingen, Germany

January 2015
    Training of Postdoctoral Researcher at AFM
    Georg-August-University, Göttingen, Germany

April 2014 - March 2014
    Supervision of Master Student
    Georg-August-University, Göttingen, Germany

April 2014 - July 2014
    Teaching Assistant
    Georg-August-University, Göttingen, Germany
    Lab Course, Atomic Force Microscopy for Physics Students (M. Sc.)

December 2013 - February 2014
    Teaching Assistant
    Georg-August-University, Göttingen, Germany
    Lab Course, Fundamental Physics for Medical Students

Volunteer Experience

June 2013 - September 2014
    Student Representative
    Max Planck Research School, Göttingen, Germany

March 2014
    Organization of a Talk at Max Planck PhD, Postdoc Community
    Max Planck Research School, Göttingen, Germany
    Guest: Prof. Dr. Thoshio Ando,   Kanazawa, Japan

List of Publications

Surface functionalization with durable 2D protein lattices of clathrin
Philip N. Dannhauser*, Mitja Platen*, Heike Böning, and Iwan A.T. Schaap (*equal contribution)
Nature Nanotechnology 2015, DOI: 10.1038/nnano.2015.206

Super-resolution optical fluctuation bio-imaging with dual-color carbon nanodots
Anna M. Chizhik, Weixing Li, Simon Stein, Mariia O. Dekaliuk, Christopher Battle, Anja Huss, Mitja Platen, Iwan A.T. Schaap, Ingo Gregor, Alexander P. Demchenko, Christoph Schmidt, Jörg Enderlein, Alexey . Chizhik
Manuscript in preparation

Calcium induces syntaxin 1/PI(4,5)P2 mesoscale domins
Dragomir Milovanovic, Mitja Platen, Meike Junius, Ulf Diederichsen, Iwan A.T. Schaap, Alf Honigmann, Stefan W. Hell, Geert van den Bogaart and Reinhard Jahn
Manuscript in preparation

Poly(2-oxazoline) based microgel particles for neuronal cell culture
Mitja Platen, Evelien Mathieu, Steffen Lueck, René Schubel, Rainer Jordan and Sophie Pautot
Biomacromolecules 2015, DOI: 10.1021/bm501879h

Effect of clathrin light chains on the stiffness of clathrin lattices and membrane budding
Philip N. Dannhauser, Mitja Platen, Heike Böning, Huberta Ungewickell, Iwan A.T. Schaap and Ernst J. Ungewickell
Traffic 2015, DOI: 10.1111/tra.12263

Label-Free Measurement of Amyloid Elongation by Suspended Microchannel Resonators
Yu Wang , Mario Matteo Modena , Mitja Platen , Iwan A. T. Schaap and Thomas P. Burg
Anal. Chem., 2015, 87 (3), pp 1821–1828

Hypoxia induces EMT in low and highly aggressive pancreatic tumor cells but only cancer stem-like cells acquire high migratory potential
Alexei V. Salnikov*, Li Liu*, Mitja Platen, Jury Gladkich, Olga Salnikova, Eduard Ryschich, Jürgen Mattern, Gerhard Moldenhauer, Jens Werner, Peter Schemmer, Markus W. Büchler and Ingrid Herr (*equal contribution)
PLOS ONE 2012, DOI: 10.1371/journal.pone.0046391

The wine under your bed
Mitja Platen*, José Negrete Jr.*, Franziska Schmidt*
(*equal contribution)
MPIbpc NEWS, Jan. 2014
Written during one week soft skill course, "Science and medical writing for the public"